Dynamics and Thermodynamics of Baryons in Galaxy-Sized Cold Dark Matter Halos

---

Dissertation

zur

Erlangung der naturwissenschaftlichen Doktorwürde

(Dr. sc. nat.)

vorgelegt der

Mathematisch-naturwissenschaftlichen Fakultät

der

Universität Zürich

von

Aleksandra Sokołowska

aus

Polen

Promotionskommission

Prof. Dr. Lucio Mayer (Vorsitz)
Prof. Dr. Romain Teyssier
Prof. Dr. Robert Feldmann
Prof. Dr. Ravit Helled

Zürich, 2018

"Science is a reflection of our very human disquietude, of our longing for order and control, of our awe and fear at the immensity of cosmos". M.Gleiser

Contents

Abstract

This work covers aspects of both the dynamics and thermodynamics of baryons in Galaxy-sized cold dark matter halos. We focus on the Milky Way mass scale because of (1) the wealth of data available in our own habitat, (2) the reasons to believe that it marks a critical mass scale for the effect of feedback mechanisms on the star formation efficiency, (3) for the development of a hot gaseous atmosphere around the disk, and (4) for the transition between the blue and the red sequences of galaxies.

There are three main challenging areas of galaxy formation addressed in this thesis. First, we study if galaxies and their halos grow in a quasi-homologous way in models with varied subgrid physics or initial conditions. Second, we determine whether the state-of-the-art models of galaxy formation produce not only realistic galaxies but also realistic present-day gaseous galactic halos. Finally, we investigate if the Galactic X-ray luminous corona is a consequence of hot spherical accretion, or if it results from heating induced by shocks in mergers and by supernovae feedback. In order to advance the understanding of these problems, we use high-resolution cosmological zoom-in simulations of galaxy formation as our main tool. The numerical experiments are performed with the Smoothed Particle Hydrodynamics (SPH) code Gasoline, and include both published (Eris, ErisBH) and novel realizations (Eris2k, ErisNFB, Venus). Our major findings are presented in the three main chapters of this work.

In the first part of this thesis, we investigate the angular momentum evolution of four disk galaxies residing in the Milky Way-sized halos, and we study them in the context of the physically motivated alternative to the Hubble sequence called the j_*–M_* diagram. We find that galaxies born in high- and low-density environments evolve differently on this diagram. Moreover, the angular momentum of the total stellar mass of the galaxy (the sum of a bulge and a disk) is similar, and for the stellar disk alone really identical, to that of the dark matter.

Our results indicate that, after averaging over numerous but brief fluctuations, galaxies and their halos grow approximately homologously with each other.

In the second part of this thesis, we investigate the properties of present-day gaseous halos in simulated Milky Way analogs with varying sub-grid physics. We adopt various benchmarks, such as the X-ray luminosity, electron number density profiles of the Milky Way, circumgalactic medium (CGM) studies of the extragalactic L_* objects, dispersion measures and ram pressure stripping arguments, to test the properties of the gaseous halos arising in the simulations. We find a model both satisfying those measurements, and producing a realistic Milky Way-analog. Moreover, we show that concealing of the ubiquitous warm–hot baryons, along with the ejection of just $20-30\%$ of the diffuse gas out of the potential wells by supernova–driven outflows, can solve the "missing baryon problem".

In the final part, we investigate which physical processes are responsible for the formation of an X-ray luminous corona. We show new evidence that before the gravitational heating can sustain extended hot atmospheres of gas, merger-induced shock heating and supernova feedback are capable of generating extended reservoirs of diffuse low-density gas around galaxies. We discuss how the transition from cold mode to hot mode accretion is driven by the presence of such a corona. This leads to a new scenario for the thermodynamical evolution of diffuse gas in galaxies, which complements the standard model for the origin of stable hot gas atmospheres. The implications for mechanisms leading to galaxy quenching are discussed.

Zusammenfassung

Diese Arbeit behandelt Aspekte der Dynamik und der Thermodynamik von Baryonen in Galaxien-grossen kalter dunkler Materie. Wir konzentrieren uns auf die Massenskala der Milchstraße (1) wegen der Fülle an Daten, die in unserem eigenen Umgebung verfügbar sind, (2) weil es Gründe gibt, zu glauben, dass sie eine kritische Massenskala für den Effekt von Feedbackmechanismen auf die Effizienz der Sternentstehung und (3) für die Entwicklung einer heißen Gasatmosphre um die Scheibe herum hat und (4) weil sie den die blauen und die roten Galaxiensequenz trennt.

In dieser Arbeit werden drei herausfordernde Bereiche der Galaxienbildung behandelt. Zunchst untersuchen wir, ob Galaxien und ihre Halos in Modellen mit unterschiedlicher Subgridphysik oder Anfangsbedingungen quasi-homolog wachsen. Zweitens bestimmen wir, ob die modernsten Modelle der Galaxienbildung nicht nur realistische Galaxien, sondern auch realistische gasförmige galaktische Galaxien erzeugen. Schließlich untersuchen wir, ob die galaktische Röntgen-Leuchtkorona eine Folge von heißer sphrischer Akkretion ist oder ob sie durch Erwrmung verursacht wird, die durch Schockwellen bei Kollisionen und durch Supernova-Feedback induziert wird. Um das Verstndnis dieser Probleme zu fördern, verwenden wir hochauflösende kosmologische Zoom-In-Simulationen der Galaxienbildung als Hauptwerkzeug. Die numerischen Experimente werden mit dem Smoothed Particle Hydrodynamics (SPH) Code Gasoline durchgeführt und umfassen sowohl veröffentlichte (Eris, ErisBH) als auch neue Erkenntnisse (Eris2k, ErisNFB, Venus). Unsere wichtigsten Ergebnisse werden in den drei Hauptkapiteln dieser Arbeit vorgestellt.

Im ersten Teil dieser Arbeit untersuchen wir die Entwicklung des Drehimpulses von vier Disk-Galaxien, die in den Milchstraßen-Halos enthalten sind, und untersuchen sie im Kontext der physikalisch motivierten Alternative zur Hubble-Sequenz namens j_* - M_* Diagram. Wir stellen fest, dass Galaxien, die in Umgebungen mit hoher und niedriger Dichte entstehen, sich

auf diesem Diagramm unterschiedlich entwickeln. Darüber hinaus ist der Drehimpuls der gesamten Sternmasse der Galaxie (Ausbuchtung und Scheibe) hnlich, und die Sternscheibe allein ist wirklich identisch mit der der dunklen Materie. Unsere Ergebnisse zeigen, dass Galaxien und ihre Halos nach Mittelung über zahlreiche, aber kurze Fluktuationen annhernd homolog zueinander werden.

Im zweiten Teil dieser Arbeit untersuchen wir die Eigenschaften heutiger gasförmiger Halos in simulierten Milchstraßenanaloga mit variierender Subgitterphysik. Wir verwenden verschiedene Maßstbe, wie Röntgenhelligkeit, Elektronenzahldichteprofile der Milchstraße, Circumgalactic Medium (CGM)-Studien der extragalaktischen L_* Objekte, Dispersionsmessungen und Stauchdruck-Stripping-Argumente, um die Eigenschaften von die in den Simulationen entstehenden gasförmigen Halos. Wir finden ein Modell, das sowohl diese Messungen als auch ein realistisches Milchstraßeanalog erfüllt. Darüber hinaus zeigen wir, dass die Verschleierung der allgegenwrtigen warm-heißen Baryonen zusammen mit dem Ausstoß von nur 20 - 30% des diffusen Gases aus den Potentialtöpfen durch supernova-gesteuerte Abflüsse das "fehlende Baryon-Problem" lösen kann.

Im letzten Teil untersuchen wir, welche physikalischen Prozesse für die Bildung einer Röntgen-Leuchtkorona verantwortlich sind. Wir zeigen neue Belege dafür, dass vor der Gravitationserwrmung ausgedehnte heiße Gasatmosphren aufrechterhalten werden können. Die fusionsinduzierte Schockheizung und die Supernova-Rückkopplung sind in der Lage, ausgedehnte Reservoirs von diffusem Gas niedriger Dichte um Galaxien herum zu erzeugen. Wir diskutieren, wie der übergang vom Kaltmodus zum Heißmodus durch das Vorhandensein einer solchen Korona gesteuert wird. Dies führt zu einem neuen Szenario für die thermodynamische Entwicklung von diffusem Gas in Galaxien, das das Standardmodell für den Ursprung einer stabilen heißen Gasphase um Galaxien ergnzt. Die Implikationen für Mechanismen, die zum Abschrecken von Galaxien führen, werden diskutiert.

Preface

This thesis consists of a general introduction into the research field, three published papers on the thermodynamics and dynamics of baryons in the Milky Way-sized halos, and the summary of an additional relevant research project I carried out during my PhD. In particular, chapter 1 covers the hierarchical framework of structure formation, and the state-of-the art of research on the assembly of gaseous galactic halos. Chapter 2 reviews the scientific methodology behind high-resolution zoom-in cosmological smoothed hydrodynamics simulations. These chapters are followed by the three main scientific publications. Chapter 6 summarizes the key findings of this thesis and is followed by the discussion of the limitations of this thesis, and the statement on how this work could be expanded in the future, in chapter 7. Finally, the Appendix contains the results of an unpublished research project, which is not the main part of this thesis but validates the results of chapter 4 in large volume hydrodynamical simulations (Eagle).

Chapter 1

Theoretical background

1.1 Hierarchical framework of structure formation

The theoretical framework for the formation of structure is based upon the gravitational instability. The early universe is assumed to have been almost perfectly smooth, with small local deviations in the density and velocity fields from the cosmic background density and the general Hubble expansion, respectively. The density perturbations induce local differences in gravity, resulting in the growth of overdensities. When overdense regions become massive enough, their expansion may cease, and a region can decouple from the Hubble expansion. A decoupled object turns around and collapses if pressure forces are not sufficient to counteract the infall. Those early stages of structure formation can be described with the linear perturbation theory up to a point when the nonlinear features emerge. The small-scale perturbations become non-linear first because they have a higher amplitude than those on a larger scale. This means that the process of structure formation occurs hierarchically.

This section serves as an overview of how structures emerge in the universe in this framework. We discuss the growth of perturbations, the collapse of regions into the objects observed today, and their acquisition of angular momentum.

1.1.1 The cosmological framework

The equations describing the evolution of the universe are derived from Einstein's theory of general relativity. A flat, homogeneous and isotropic universe is described by the Friedmann-

Table 1.1: How space expanded in different epochs of the Universe.

EPOCH	SCALE FACTOR
radiation-dominated	$a(t) \propto t^{1/2}$
matter-dominated	$a(t) \propto t^{2/3}$
Λ-dominated	$a(t) \propto \exp(Ht)$

Robertson-Walker (FRW) metric

$$ds^2 = dt^2 - a^2(t)\delta_{ij}dx^i dx^j, \tag{1.1}$$

with ds^2 the space-time separation, δ_{ij} the Kronecker delta, x^i the local coordinate running from $i = 1$ to $i = 3$. The scale factor $a(t)$ satisfies the Friedmann equations

$$H^2 = \left(\frac{\dot{a}}{a}\right)^2 = \frac{8\pi G}{3}\rho + \frac{kc^2}{a^2} \tag{1.2}$$

$$\frac{\ddot{a}}{a} = -\frac{4\pi G}{3}(\rho + 3P), \tag{1.3}$$

where k stands for the type of geometry (for flat, $k = 0$), and ρ and P should be understood as the sum of all contributions to the to the energy density (i.e. radiation, matter, vaccum energy) and pressure in the universe. $\dot{a} > 0$ implies expanding universe. Additionally, $\ddot{a} > 0$ corresponds to an accelerating expansion. Observations favor an accelerating flat universe composed of abour 5% of baryons, 27% of dark matter, and 68% of dark energy (Λ).

1.1.2 Linear perturbation theory

The deviation from smoothness in the density at a given point and time is defined as

$$\delta(\vec{\mathbf{x}}, t) = \frac{\rho(\vec{\mathbf{x}}, t) - \rho_0(t)}{\rho_0(t)}, \tag{1.4}$$

where $\rho(\vec{\mathbf{x}}, t)$ is the physical density and ρ_0 is the cosmic background density. The perturbation theory makes use of the continuity equation, the Euler equation and the Poisson equation, in order to derive the equation describing the time evolution of the linear ($\delta \ll 1$)

density perturbations. This equation has a form of

$$\ddot{\delta_k} + 2H\dot{\delta_k} = \left(4\pi G\rho_0(t) - \frac{k^2c_s^2}{a^2}\right)\delta_k, \tag{1.5}$$

where k is the Fourier mode, c_s the sound speed, a the scale factor, G the gravitational constant, and H the Hubble constant. If the wave number k is smaller than the Jeans wave number

$$k_J = a(t)\frac{\sqrt{4\pi G\rho_0}}{c_s}, \tag{1.6}$$

perturbations grow exponentially with time. Otherwise, perturbations oscillate as sound waves. Note that the equation 1.6 implies that the expansion slows down the growth of the perturbations (Elgaroy, 2017).

Perturbations evolve differently during the radiation and matter dominated epochs of the universe. The differences are summarized below.

The radiation-dominated era. Matter density is heavily dominated by the cold dark matter which is pressureless, hence the pressure term can be neglected in eq. 1.5. With this assumption, one can find that δ_k can grow between the beginning of the universe and the epoch of equivalence of matter and radiation maximally by a factor of 5/2. This growth is thus insignificant.

The matter-dominated era. In that epoch, the evolution of density perturbations in baryons is induced by a pressureless (cold) dark matter component. The perturbations of dark matter can be derived in the EdS[1] cosmology with only dark matter contributing to the matter density. The general solution to the eq. 1.5 has then a growing mode of $\delta_{dm} \propto a(t)$.

The density perturbations in baryons, δ_b , obey the following equation:

$$\frac{d^2\delta_b}{dt^2} + 2\frac{\dot{a}}{a}\frac{d\delta_b}{dt} + \frac{k^2c_s^2a}{a^3}\delta_b = 4\pi G\frac{\rho_0 a_0^3}{a^3}\rho_{dm}, \tag{1.7}$$

with a_0 and ρ_0 being the scale factor and the matter density at the present time. In the case

[1]Einstein de Sitter matter-dominated universe with $\Omega_m = 1$

of a polytropic fluid and the EdS universe, a special solution exists in the form of

$$\delta_b(\vec{\mathbf{k}}, t) = \frac{\delta_{dm}(\vec{\mathbf{k}}, t)}{1 + k^2/k_J^2} \tag{1.8}$$

with $k_J = \frac{3a^2H^2}{2c_s^2}$. This implies that baryons follow dark matter perturbations with the amplitude dependent on the scale. If $k \ll k_J$ (large scales), baryons behave as a pressureless fluid similar to dark matter. Conversely, on small scales ($k \gg k_J$), the baryonic pressure initially suppresses the growth of perturbations and causes acoustic oscillations, which at the later times are damped by the expansion of the universe. As before recombination baryons are coupled to photons, the only perturbations is the baryon fluid were sound waves of amplitudes of order the cosmic microwave background (CMB) anisotropies. Only after the recombination would baryons follow dark matter perturbations. Without dark matter, baryonic perturbations would have been in the linear regime today, and bound structures such as galaxies that we observe today would not have formed.

1.1.3 A spherical collapse of dark matter

A highly idealized case of a top-hat spherical collapse allows us to gain insights into the non-linear ($\delta \gg 1$) evolution of density perturbations, under the assumption that the universe is homogeneous except for a single top-hat spherical perturbation (Mo et al., 2010). Considering a single collisionless mass shell of a radius r at some initial time t, the mass enclosed by a shell is $M(< r) = \frac{4}{3}\pi r^3(t)\bar{\rho}(t)[1 + \delta(t)]$, where δ and $\bar{\rho}$ denote the top-hat overdensity and the background density. The integrated equation of motion has the form of

$$\frac{1}{2}\left(\frac{dr}{dt}\right)^2 - \frac{GM}{r} = E, \tag{1.9}$$

with $E < 0$ being the specific energy of a bound overdensity. The solution of a mass shell growing at the same rate as the EdS universe ($r \propto a$) can be written in the parametric form:

$$r = A(1 - \cos\theta) \quad t = B(\theta - \sin\theta) \quad \theta \in [0, 2\pi] \tag{1.10}$$

$$A = \frac{GM}{2|E|} \quad B = \frac{GM}{(2E)^{3/2}} \quad A^3 = GMB^2. \tag{1.11}$$

The shell expands from $r = 0$ (at $\theta = 0$ and $t = 0$) until it reaches a maximum r_{ta} (also known as a turn-around radius, $\theta = \pi$ and $t_{ta} = \pi B$) and collapses back to $r = 0$ (at $\theta = 2\pi$ and $t = t_{coll} = 2t_{ta}$). The overdensity of the spherical top-hat region evolves as

$$1 + \delta = \frac{9}{2}\frac{(\theta - \sin\theta)^2}{(1 - \cos\theta)^3}. \tag{1.12}$$

The expression for δ can be used to normalise the predictions of the linar theory, namely $\delta_{lin} \propto a \propto t^{2/3}$. Taylor expanding $\sin\theta$ and $\cos\theta$ around $\theta \ll 1$ yields

$$\delta_{lin} = \frac{3}{20}(6\pi)^{2/3}\left(\frac{t}{t_{ta}}\right)^{2/3}, \tag{1.13}$$

which can be evaluated at the times of the turnaround and collapse. Hence, in the linear regime $\delta_{lin}(t_{ta}) \sim 1.0624$ and $\delta_{lin}(t_{coll}) \sim 1.6865$, meaning that regions in the linearly extrapolated density field of $\delta_{lin} \geq 1.686$ should have collapsed.

The above description is valid up to the point of shell crossing, that is when a shell begins to cross itself and oscillates (note $M(r)$ is no longer conserved). When the shell crossing occurs, the oscillating shells begin to exchange energy (virialize). Virialization is a process in which the system relaxes to the virial equilibrium that can be written as

$$2K + W = 0, \tag{1.14}$$

where K and W are the kinetic and potential energy, respectively. Combining the virial equilibrium with the conservation of energy at the collapse yields a useful relationship that $r_{vir} = r_{ta}/2$. A bound structure in virial equilibrium is referred to as the dark matter halo. The final density of the dark matter halo in the EdS universe is

$$1 + \Delta_{vir} \equiv 1 + \delta_{coll} = \frac{\rho_{coll}}{\bar{\rho}_{coll}} = \frac{8\rho_{ta}}{\bar{\rho}_{ta}/4} = 18\pi^2 = 178. \tag{1.15}$$

In the last equation, we used the fact that the cosmic background density and the overdensity at the time of the collapse are 4 and 8 times higher than at the turnaround, respectively.

1.1.4 A collapse in the Zel'dovich approximation

The linear perturbation theory is generally valid until $\delta \ll 1$. However, one can follow the evolution of a perturbation down to $\delta \sim 1$ using the Zel'dovich approximation (Zel'dovich, 1970). The use case of Zel'dovich approximation is not only to gain insights into the nature of a collapse of matter but also to set the initial conditions of numerical simulations, i.e. the initial velocities and positions of particles in the astrophysical fluid. The ZA has two major advantages over the spherical collapse model: 1) it does not oversimplify the geometry of the collapse; 2) it is accurate in the quasi-linear regime.

The deformation of matter perturbations can be studied in this framework. In the Lagrangian frame, $\vec{\mathbf{q}}$ is a comoving coordinate of a particle at the center of the perturbation, and $\vec{\mathbf{x}}$ the proper coordinate of another nearby particle. The trajectory of the nearby particle can be written as

$$\vec{\mathbf{x}}(t) = a(t)\vec{\mathbf{q}} + b(t)\vec{\mathbf{f}}(\vec{\mathbf{q}}), \tag{1.16}$$

where the first term represents the Hubble expansion of $\vec{\mathbf{x}}$ relative to $\vec{\mathbf{q}}$, and the second term describes the comoving deviation from the Hubble flow parametrized by a function $\vec{\mathbf{f}}(\vec{\mathbf{q}})$. This function can be represented by three constants, α, β, γ, related to the principal axes of an ellipsoid, if the initial configuration of the particles is assumed to be an ellipsoid.

Two parameters in the eq. 1.16, $a(t)$ and $b(t)$, are assumed to be the same for all particles. The diagonal *deformation tensor*

$$D = |dx_i/dq_i| = a(t)\delta_{ij} + b(t)\partial x_i/\partial q_j \tag{1.17}$$

describes the motion of these particles. Using the conservation of mass in the deforming ellipsoid, the density evolution can be written as

$$\rho(a - b\alpha)(a - b\beta)(a - b\gamma) = \bar{\rho}a^3. \tag{1.18}$$

For the EdS universe[2], one obtains $a(t) = (t/t_0)^{2/3}$ and $b(t) = 0.4(t/t_0)^{4/3}$, with $t_0 = 2/3H_0$ being the final time of a collapse. The collapse happens first along the axis associated with the largest of the constants α, β, or γ, leading to flattened structures called Zel'dovich pancakes (see Figure 1.1). Zel'dovich approximation breaks once shell crossing occurs (i.e.

[2]Einstein de Sitter matter-dominated universe with $\Omega_m = 1$

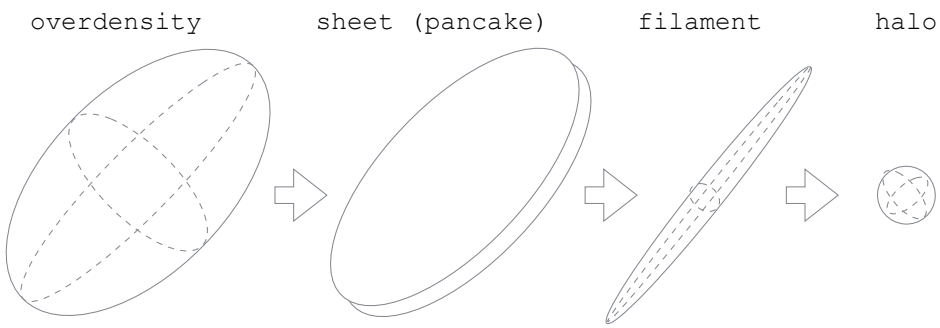

Figure 1.1: Qualitatively, perturbations are triaxial, and hence the collapse along all axes is not synchronous. A perturbation will first form a sheet (pancake), then a filament, and finally a quasi-spherical halo (van den Bosch, 2010).

$a(t) - b(t)\alpha = 0$).

The Zel'dovich approximation is used to set the initial conditions of the numerical simulations of structure formation. Particles' positions are displaced with respect to the initialized uniform grid from about $z \sim 1000$ until the time of the first shell crossing in the volume. The velocities of particles are computed as

$$\dot{\vec{\mathbf{x}}} = \dot{b}(t)\vec{\mathbf{f}}(\vec{\mathbf{q}}). \tag{1.19}$$

Once the initial conditions are generated, the evolution of the structures in the universe is then followed numerically.

1.1.5 Angular momentum of dark matter halos

As perturbations on small scales have a higher amplitude than those on a larger scale, less massive dark matter halos form first. More massive halos form at a later time via merging of smaller halos. As discussed above, baryons follow the perturbations and the collapse of much more abundant dark matter, hence galaxies we observe today are expected to reside within the dark matter halos.

The angular momentum of dark matter halos is usually characterized by the dimensionless spin parameter

$$\lambda_P \equiv \frac{J|E|^{1/2}}{GM^{5/2}}, \tag{1.20}$$

where J, E and M are the total angular momentum, energy and mass of the halo, respectively (Peebles, 1969, 1971). The spin parameters takes on two characteristic values for simple objects:

$$\lambda = \begin{cases} 0.5 & \text{for rotating, self-gravitating disk} \\ 0 & \text{for a non-rotating spheroid.} \end{cases} \tag{1.21}$$

An alternative definition which avoids the need to calculate the halo energy explicitly has the form of

$$\lambda' = \frac{j}{\sqrt{2} v_{\rm vir} R_{\rm vir}}, \tag{1.22}$$

where j is the specific angular momentum, $\mathrm{v_{vir}}$ is the virial velocity and $\mathrm{R_{vir}}$ is the virial radius of the halo (Mo et al., 1998). No trends with halo mass, redshift or environment have been found in the spin parameters (Stewart, 2017). The distribution of the spin parameter has been studied extensively in many simulations and it has been found that it has a shape of a log-normal distribution

$$P(\lambda) = \frac{1}{\lambda\sigma\sqrt{2\pi}} \exp\left(-\frac{\ln(\lambda/\lambda_0)^2}{2\sigma^2}\right), \tag{1.23}$$

with the peak at $\lambda_0 = 0.035$ and a Gaussian width of $\sigma \simeq 0.5$ (see Figure 1.2).

Tidal Torque Theory (TTT). Dark matter halos acquire angular momentum due to the torques exerted by the tidal gravitational fields of their neighbours. According to the linear TTT, the angular momentum of a virialized halo should be

$$\mathrm{J_{vir}} = \int_0^{\mathrm{t_{ta}}} \mathrm{J(t)dt} = \epsilon_{\mathrm{ijk}} \mathrm{T_{ij}} \mathrm{I_{lk}} \int_0^{\mathrm{t_{ta}}} \mathrm{a^2(t)\dot{D}(t)dt}, \tag{1.24}$$

where $\dot{D}(t)$ is the time-derivative of the linear growth rate, ϵ_{ijk} the Levi-Civita tensor, T_{ij} the tidal tensor, and I_{lk} the inertial tensor. In the linear theory, the angular momentum grows until a halo reaches the maximum expansion (turnaround, t_{ta}), after which it collapses and virializes, conserving the angular momentum in the process. $J(t)$ represents the contribution

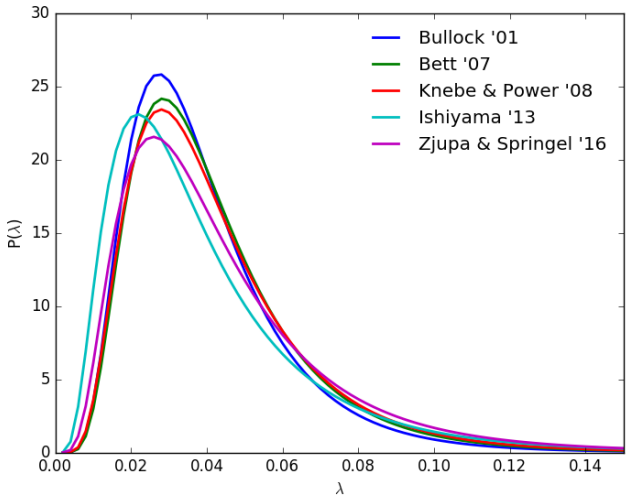

Figure 1.2: The distributions of dark matter halo spin parameters adopted from (Stewart, 2017).

of individual Lagrangian volumes, which end up as a part of the virialized halo. The linear TTT implies that for an EdS cosmology $J \propto t$.

Mergers. Numerical simulations show that the overall behavior of the angular momentum growth of proto-halos is consistent with the linear TTT. However, the linear TTT overpredicts the total angular momentum of a virialized halo by a factor of 3 (Sugerman et al., 2000). There are also two major differences between the assumptions adopted by TTT and the numerical simulations, which are illustrated in Figure 1.3. First, there is a substantial growth of angular momentum between the turnaround and the collapse. Second, the impact of mergers and tidal interactions with other objects on the evolution of angular momentum after the turnaround is substantial.

1.1.6 Galaxy formation

Standard picture. In the framework of structure formation (White & Rees, 1978), galaxies form in the dark matter halo from the gas, which dissipates its energy via radiative cooling and contracts up to the point when the angular momentum supports the halo against collapse in the directions perpendicular but not parallel to the overall angular momentum

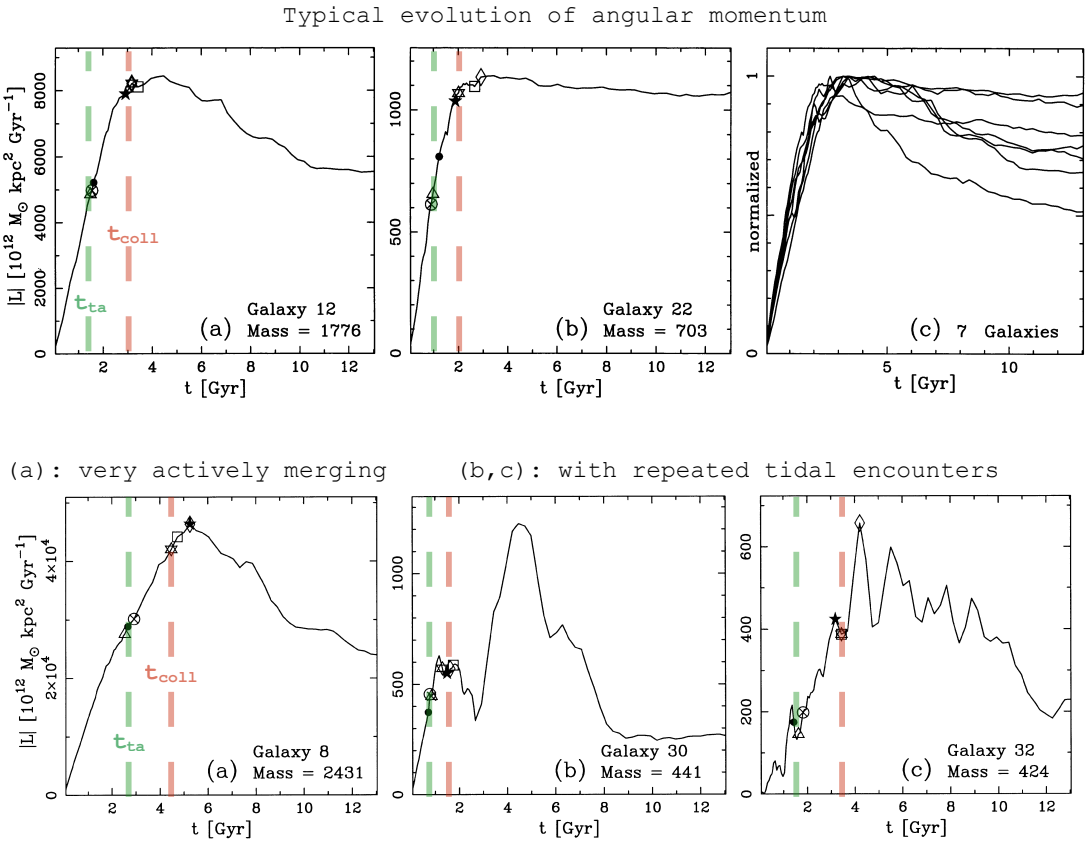

Figure 1.3: Results from the numerical simulations. Top shows that typically, the angular momentum L grows linearly beyond turnaround, turns over during shell crossing, and remains constant as the galaxy relaxes and virializes. Bottom illustrates how that evolution can be disturbed by either numerous mergers or repeated tidal encounters. Adopted from (Sugerman et al., 2000).

vector, forming a flattened disk (Gott & Thuan, 1976). The standard picture of disk formation states that the collapsing gas arranges itself into an exponential disk with a scale length R_d (Fall & Efstathiou, 1980). It then holds that

$$J_d = 2\pi \int_0^\infty \Sigma(R) v_c(R) R^2 dR = 2\mathrm{M_d R_d v_c}, \tag{1.25}$$

where J_d is the angular momentum of the disk, v_c the circular velocity, Σ the surface density of the infititesimally thin disk, and M_d the mass of the disk. When one ignores terms of order λ^2 in the energy E, the angular momentum of the dark matter halo can be determined from eq. 1.20 and yield

$$J_H = \sqrt{2}\lambda \mathrm{M_{vir} v_c R_{vir}}. \tag{1.26}$$

Assuming that baryons and dark matter acquire identical specific angular momentum distributions through torques, and that baryons conserve their specific angular momentum while cooling, one can derive a relationship between the sizes of dark matter halos and the galactic disks, namely

$$\frac{R_d}{R_{vir}} = \frac{\lambda}{\sqrt{2}} \simeq 0.025, \tag{1.27}$$

for $\lambda = 0.035$. The proportionality between the galaxy and halo sizes inferred with these assumptions is confirmed with recent observations, as shown in Figure 1.4. We note that this standard picture has been extended with self-gravity of the disk and a correction of the circular velocity of the NFW dark matter halo for the adiabatic contraction due to disk formation (Mo et al., 1998).

Specific angular momentum. Angular momentum of dark matter scales as $J \propto M^{5/3}$ (specific angular momentum as $j_{DM} \propto M^{2/3}$), which can be obtained from tidal torque theory ($J \propto I \propto MR^2 \propto M^{5/3}$) or the argument of mechanicam equilibrium ($J \propto MRV \sim M^{5/3}$). ΛCDM N-body simulations are consistent with that scaling (e.g. $J \propto M^{1.5\pm1.75}$ (Sugerman et al., 2000)). The specific angular momenta of observed galaxies were also found to scale as $j_{gal} \propto M^{2/3}$, with an offset between the track of pure disks and pure ellipticals of order 5-6 (Fall, 1983; Romanowsky & Fall, 2012). The ratio between the j_{gal} and j_{DM}, the so-called

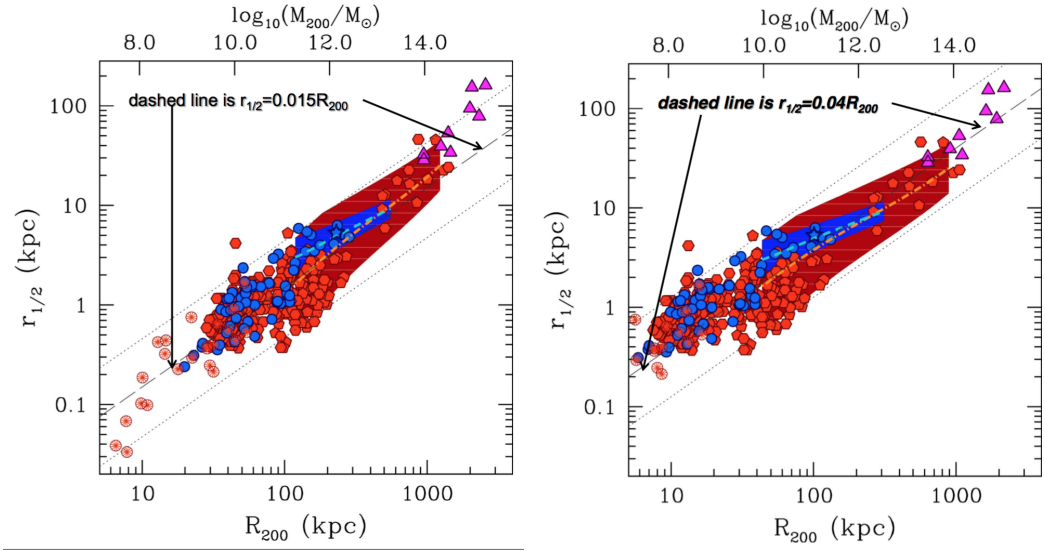

Figure 1.4: Size-virial radius relation of galaxies. Blue points – a sample of late-type galaxies, red points – spheroidal galaxies, magenta triangles – BCGs. See (Kravtsov et al., 2014; Kravtsov, 2014). Dashed black lines show linear relations with different proportionality constants. Black dotted lines are linear relations offset by 0.5 dex. Left. The proportionality constant is 0.015. Right. The sample of objects from the left are corrected for the pseudo-evolution of R_{200}, occuring when the change in R_{200} is due to the change in critical density of the Universe and not the evolution of the halo. The proportionality constant of the relation is then 0.04.

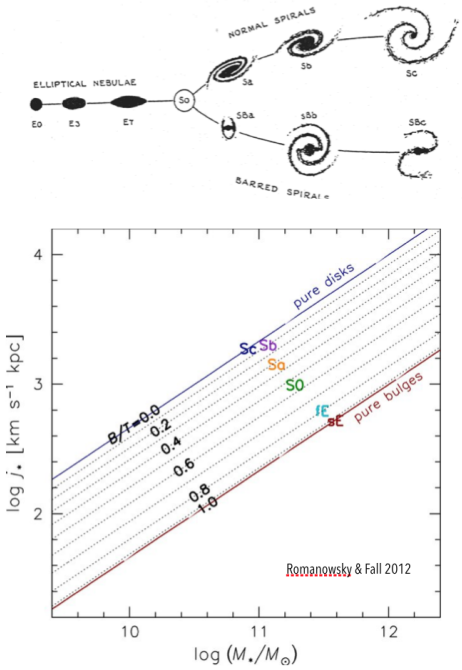

Figure 1.5: A physically-motivated alternative to the Hubble diagram: $j_* - M_*$ diagram classifying different morphological types by specific angular momentum (Romanowsky & Fall, 2012).

retention factor η_j, was found to be different for pure disks and ellipticals, namely

$$\eta_j = \begin{cases} 0.8 & \text{for Sc galaxies} \\ 0.1 - 0.2 & \text{for E galaxies.} \end{cases} \tag{1.28}$$

This lead to a conjecture that there is a connection between the j_{gal} vs M_{gal}, or j_* vs. M_*, the bulge-to-disk ratio (B/T), and the Hubble type, which was confirmed with a sample of well-resolved galaxies (Romanowsky & Fall, 2012; Fall & Romanowsky, 2013). The $j_* - M_*$ diagram is a physics-based alternative to the morphology-based Hubble sequence, as illustrated in Figure 1.5. This classification method has the advantages of being quantitative, robust and having theoretical foundations.

In general, many properties of galaxies, such as flat rotation curves and the Tully-Fisher relation (Tully & Fisher, 1977), could be obtained in the Cold Dark Matter framework, if the specific angular momenta of disks ($j \equiv J/M$) are similar to those of their halos, and approximately conserved during the collapse of gas within hierarchically-forming dark matter

halos (Fall & Efstathiou, 1980; Mo et al., 1998). The conservation implied is "weak", i.e. it does not assume conservation of the internal distribution of J with radius, which in fact could be readily altered by secular processes within disks while still preserving the total J (see the discussion in Fall, 2002; Kormendy & Kennicutt, 2004). In principle, weak conservation of the total specific angular momentum of each component during and after the collapse could explain why the total specific angular momenta of dark matter (assuming constant λ) and galaxies (baryons) scale as $j \propto M^{2/3}$, with their ratios $j_{\rm gal}/j_{\rm dm}$ being dependent on the morphological type (Fall, 1983; Romanowsky & Fall, 2012; Fall & Romanowsky, 2013; Obreschkow & Glazebrook, 2014).

However, two major issues greatly complicate this picture: 1) galaxies may not sample the initial angular momentum distribution of all baryons, and 2) the angular momentum may be altered during the lifetime of a galaxy. This could be done through stellar feedback and outflows (Binney et al., 2001), galaxy collisions (Jesseit et al., 2009), and non-spherically symmetric accretion (Brooks et al., 2009; Kassin et al., 2012). Angular momentum can be both lost, e.g. due to torques associated with violent disk instabilities (Danovich et al., 2015), or significantly increased in galactic fountains if material is ejected for long times and to large radii (Übler et al., 2014).

Angular momentum catastrophe. Numerical experiments are the only way to study systems with such a degree of complexity, but galaxy-formation simulations have struggled for over 20 years to produce large enough disks (Navarro et al., 1995). The angular momentum catastrophe was going hand in hand with the overcooling problem - the combination of dynamical friction and gravitational torques within the halos transferred most of the orbital angular momentum of the baryons to the dark matter, causing clumps of baryons to sink inwards. Both problems were resolved with increased resolution and improved prescriptions for feedback (Governato et al., 2007; Kaufmann et al., 2007; Zavala et al., 2008; Governato et al., 2010; Guedes et al., 2011; Danovich et al., 2015).

1.2 The assembly of gaseous galactic halos

Present-day galaxies are embedded in massive reservoirs of gas. Gaseous galactic halos are defined as baryons stretching between the verge of the galactic disks and the boundary of

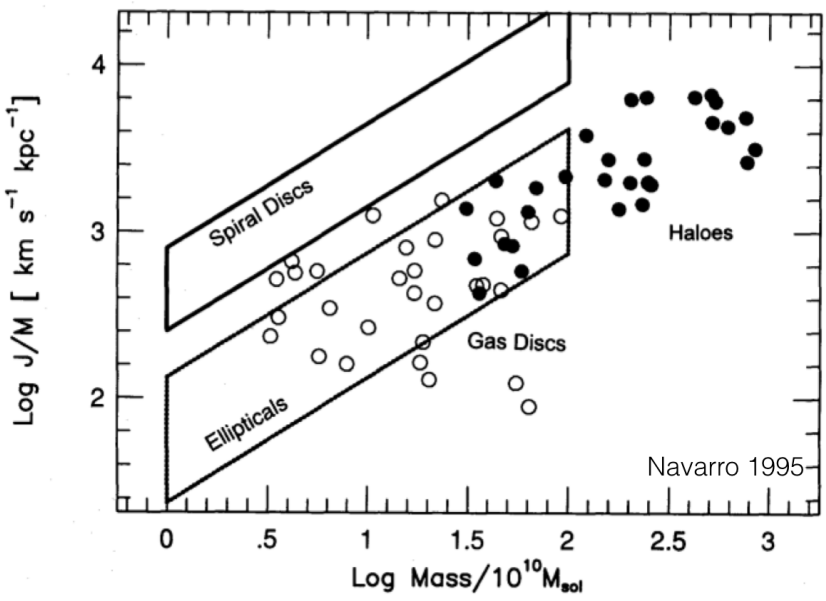

Figure 1.6: The angular momentum catastrophe (Navarro et al., 1995). Simulated gas disks used to have much lower specific angular momentum than observed galaxies.

the halo (the virial radius). The standard picture of galaxy formation assumes that gas shock heats to approximately the virial temperature of the halo as it falls into a dark matter potential well (White & Rees, 1978; Fall & Efstathiou, 1980). The virial temperature can be derived from the virial theorem applied to e.g. a truncated singular isothermal sphere, yielding

$$T_{vir} = \frac{\mu m_p}{2k_B} v_c^2 \simeq 10^6 \left(\frac{v_c}{167 \text{ km s}^{-1}}\right)^2 \text{K}, \tag{1.29}$$

with μ the mean molecular weight, m_p the proton mass, k_B the Boltzmann constant, and v_c the circular velocity of the halo. However, simulations find that more than half of the gas accreted by galaxies is never shock heated to close to the virial temperature of the halo (Kereš et al., 2005).

This section serves as an overview of the state-of-the-art research on the thermodynamics and assembly history of gaseous galactic halos. The geometry of accretion flows, the balance between the cooling and heating, as well as the observational status of the circumgalactic medium (CGM) are reviewed.

1.2.1 Thermodynamics of diffuse gas

A gas cloud of mass M_{gas} falling into a halo with a velocity v_{in} will experience an accretion shock at the shock radius (typically near the virial radius, Birnboim & Dekel (2003)). If we ignore the internal energy of the infalling gas and assume that shock thermalizes all the kinetic energy of the gas cloud, for the monoatomic gas it holds that

$$\frac{3}{2}Nk_BT_{sh} = \frac{1}{2}M_{gas}v_{in}^2, \tag{1.30}$$

where $N = M_{gas}/(\mu m_p)$ is the number of gas particles. The final temperature of shocked gas is thus approximately

$$T_{sh} = \frac{\mu m_p}{3k_B}v_{in}^2. \tag{1.31}$$

Gas falling in from large distances will have the velocity proportional to the escape velocity at the shock radius (virial radius), which then can be connected to the virial velocity by a parameter χ that depends on the density profile of the halo. Finally,

$$T_{sh} \simeq \frac{\chi}{3}\frac{\mu m_p}{k_B}v_{vir}^2 \sim T_{vir}. \tag{1.32}$$

After gas enters the halo and shock-heats, gas may cool and further collapse. The main cooling mechanisms include the inverse Compton scattering of microwave background photons (very efficient at $z > 10$), and radiative cooling by bound-bound and bound-free transitions. The cooling of hot gas near T_{vir} ($T > 2$ keV) is dominated by thermal bremsstrahlung. The formation of hot atmospheres of gas thus depends on the cooling rate of gas. The cooling time is defined as the ratio of the specific energy content to the cooling rate. For each radial shell of the halo with the isothermal distribution and in hydrostatic equilibrium, the cooling time is

$$t_{cool}(r) = \frac{3}{2}\frac{\rho_g(r)}{\mu m_p}k_BT\left(n_e^2(r)\Lambda(T)\right)^{-1}, \tag{1.33}$$

with ρ_g being the density profile of the gas, n_e the electron density profile, and $\Lambda(T)$ the cooling function. In this approximation, the formation of hot atmospheres of gas depends on the size of the cooling radius relative to the virial radius. A cooling radius r_{cool} is defined as the point where the cooling time is equal to the age of the universe. If $r_{cool} \ll r_{vir}$, the accretion shock radiates only weakly (White & Frenk, 1991). The maximal halo mass for

efficient cooling, and hence the first constraint on the critical mass of the halo for suppporting shock-heated reservoirs of gas, has been estimated in this way to be $10^{12-13}\mathrm{M}_{\odot}$.

1.2.2 Cold vs. hot accretion

More accurate estimates of $\mathrm{M}_{\mathrm{crit}}$. In order to retain the atmospheres of diffuse gas, the radiative cooling rate must be slower than the compresson rate, i.e. $t_{cool}^{-1} < t_{comp}^{-1}$, which stabilizes the shock against the gravitational pull (Dekel & Birnboim, 2006). The following derivation assumes that the virial shock is spherical and propagates outwards, and that the system obeys a strong shock limit. The jump conditions between pre-shock and post-shock (subscript 0 and 1, respectively) are

$$\begin{cases} \rho_0 = \frac{\gamma-1}{\gamma+1}\rho_1, \\ (u_0 - u_s) = \frac{\gamma+1}{\gamma-1}(u_1 - u_s), \\ P_1 = \frac{2\rho_0 u_0^2}{\gamma+1}, \\ T_1 = \frac{\mu}{k_B N_a}\frac{P_1}{\rho_1} = \frac{\mu}{k_B N_a}\frac{2\gamma-1}{(\gamma+1)^2}u_0^2, \end{cases} \tag{1.34}$$

where u is the radial velocity, N_a the Avogadro's number, and u_s the shock velocity (Zeldovich & Raizer, 1966). Note that the post-shock gas is assumed to be isothermal. The equation of state is

$$P = (\gamma - 1)\rho e, \tag{1.35}$$

where γ is the adiabatic index, P the pressure, ρ the density and e the specific internal energy. The standard Jeans stability criterion for the adiabatic case is $\gamma > \frac{4}{3}$ and can be qualitatively understood as $\frac{a_p}{a_g} \propto \rho^{\gamma-4/3}$, where $a_p/a_g = 1$ implies a hydrostatic equilibrium (accelerations due to pressure and gravity cancel out). However, this is not valid in the radiative case. If the energy is lost at a rate q per unit mass, one defines an effective index

$$\gamma_{eff} \equiv \frac{d\ln P}{d\ln \rho} = \gamma - \frac{\rho}{\dot{\rho}}\frac{q}{e}, \tag{1.36}$$

with the second equality reflecting the energy conservation in the presence of radiative losses. The compression rate in the post-shock gas is defined as the inverse of the compression time

scale

$$t_{comp} \equiv \Gamma \frac{\rho}{\dot{\rho}}, \qquad \Gamma \equiv \frac{3\gamma + 2}{\gamma(3\gamma - 4)} = \frac{21}{5}, \tag{1.37}$$

where the last equality is valid for the monoatomic gas. The cooling rate is the inverse of the radiative cooling time expressed as

$$t_{cool} \equiv \frac{e}{q}. \tag{1.38}$$

Altogether, the final γ_{eff} is thus

$$\gamma_{eff} = \gamma - \Gamma^{-1} \frac{t_{comp}}{t_{cool}}. \tag{1.39}$$

It then holds that

$$\gamma_{eff} > \gamma_{crit} \equiv \frac{2\gamma}{\gamma + 2/3} = \frac{10}{7}, \tag{1.40}$$

where γ_{crit} follows from the perturbation analysis[3](Birnboim & Dekel, 2003). Putting together eqs.1.39 and 1.40, we get

$$t_{cool} > t_{comp}. \tag{1.41}$$

The critical stability criterion can be translated into the corresponding critical halo virial mass as a function of radius. The analytical expression has the form of

$$M(10^{11} M_{\odot}) = 25.9 A^{3/8} (Z_{0.03}^{0.7} F)^{3/4} f_u^{-3} (1 + \widetilde{u_s})^{-3}, \tag{1.42}$$

[3]The radius of a shell is perturbed as $r \to \delta r$. Then the sign of the force $\ddot{\delta r}$ is controlled by an expression, which is a function of γ. A positive acceleration, i.e. $\gamma_{eff} > \gamma_{crit}$ ensures the expansion of the shock front.

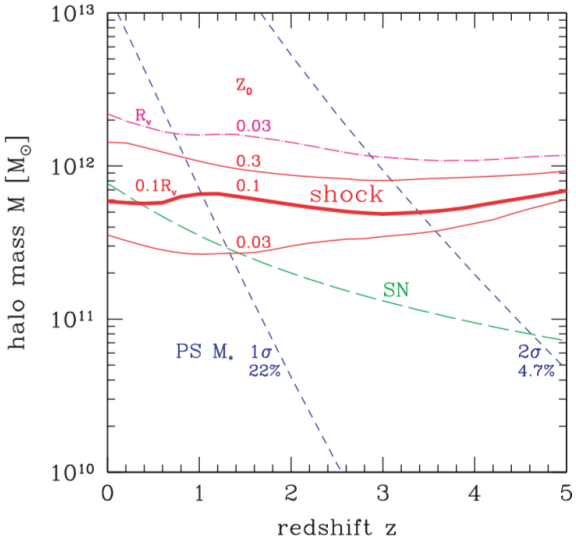

Figure 1.7: Critical mass estimate for the development of a stable shock at the virial radius (solid red lines) or 10% of the virial radius (dash-dot), and for different metallicities. As shown, the critical mass is not very sensitive to the redshift. This figure has been discussed in more detail and presented in (Dekel & Birnboim, 2006).

where

$$\begin{cases} A \equiv \frac{(\Delta_{200}\Omega_{m,0.3}h_{0.7}^2)^{1/3}}{1+z} & \text{– a parameter dependent on cosmology,} \\ f_{b,0.05} = \frac{f_b}{0.05} & \text{– the effective baryon fraction,} \\ f_{\bar{\rho},0.17} = \left(\frac{\rho}{\bar{\rho}}\right)/0.17 & \text{– the ratio derived for the universal NFW profile,} \\ Z_{0.03} = \frac{Z}{0.03} & \text{– the metallicity,} \\ \widetilde{u_s} \equiv \frac{u_s}{|u_0|} & \text{– the ratio of the radial shock velocity to the radial velocity of pre-shock gas,} \\ f_u \equiv \frac{|u|}{v_{vir}} & \text{– the ratio of infalling velocity to the virial velocity,} \\ f_r \equiv \frac{r}{R_{vir}} & \text{– the ratio of the radius of the shock and the virial radius,} \\ f_\rho \equiv \frac{\rho_0(r)}{\rho_0(R_{vir})} & \text{– the density contrast at these radii.} \end{cases}$$

Figure 1.7 shows the dependency of the critical mass threshold on redshift for various metallicities described by equation 1.42. The critical mass for the stable shock is not a strong function of redshift. Hence, the critical masses for the development of the shock at the virial

radius and at the 10% of the virial radius are estimated to be

$$M_{\rm crit}(10^{11}M_{\odot}) = \begin{cases} 26, & \text{for } R_{vir}, z=0, Z=0.03, \widetilde{u_s}=1/7, f_r=f_\rho=f_u=1; \\ 8.8, & \text{for } 0.1R_{vir}, z=0, Z=0.1, \widetilde{u_s}=0, f_r=0.1, f_\rho=100, f_u=2.5. \end{cases} \tag{1.43}$$

The results of this analytical derivation of the condition for stability is consistent with the outcomes of numerical simulations (Birnboim & Dekel, 2003; Dekel & Birnboim, 2006).

The accretion pattern in the cosmic web. Large volume smoothed particle hydrodynamics (SPH) cosmological simulations, which add to the theoretical picture above the important information about the accretion pattern, led to a significant progress in the field. Firstly, they pointed out that cooling of shock-heated gas is not the dominant source of cold star-forming gas in galactic disks. In fact, most of the gas building galaxies enters a halo cold, and thus the temperature distribution of accreted gas is bimodal. Secondly, they have shown that there are geometric differences between these two modes of accretion (referred to as cold and hot mode accretion), namely that the shock-heated gas is quasi-spherical, whereas the cold gas flows along a preferential direction in the form of dense filaments (Figure 1.8). Finally, they also provided an additional independent constraint on the critical mass for the transition between these two modes of accretion (Figure 1.9), which turned out to be nearly constant from $z = 3 - 0$ at a value of $\mathrm{M_{crit}} = 2 - 3 \times 10^{11}\mathrm{M_{\odot}}$.

Cold flows may exist even above the critical mass scale at $z \gtrsim 2$ (Dekel & Birnboim, 2006). The cross section of large halos is wider than the filaments which penetrate it[4]; the streams are thus narrow and dense, and cool very efficiently compared with the surrounding gaseous halo. At the same time, the compression rates of these components are comparable. Thus, the critical halo mass for shock heating of the filaments is expected to be higher than M_{crit} derived analytically, allowing them to prevail above M_{crit}.

The critical mass scale (an equivalent in the stellar mass of $M_* \sim 3 \times 10^{11} M_{\odot}$) is also the transition mass between two different galaxy populations, red and blue sequences, as well as the so-called quenching mass scale, on which the galaxy mass function drops exponentially. The cold mode-hot mode transition and these relations are likely to be causally connected,

[4]Massive halos exceeding the Press-Schechter mass (Press & Schechter, 1974) were found to from at the intersection of a number of filaments, whereas smaller halos form inside the single filaments. The cross section of smaller halos is of order the cross section of the filament (Kereš et al., 2005).

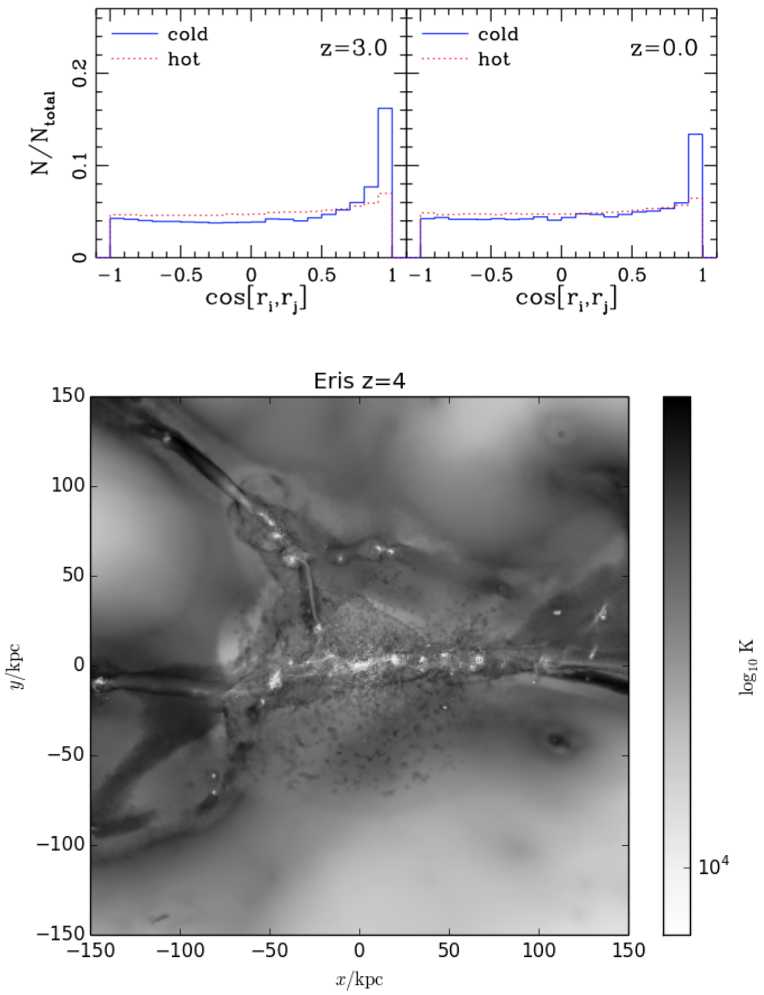

Figure 1.8: Top. The distribution of the scalar products of the radius vectors connecting the centre of simulated galaxies to the positions of all particles that will be accreted. Hot shock-heated gas is entering rather uniformly from all directions, while cold-accreted gas particle histogram has a clear peak near $\cos[r_i, r_j] \sim 1$, indicating a preferential direction (Kereš et al., 2005). Bottom. The visualization of the structure of these "cold flows" in a zoom-in hydrodynamical simulation studied in this thesis. The details of the setup of this simulation can be found in (Guedes et al., 2011) or in the next chapters.

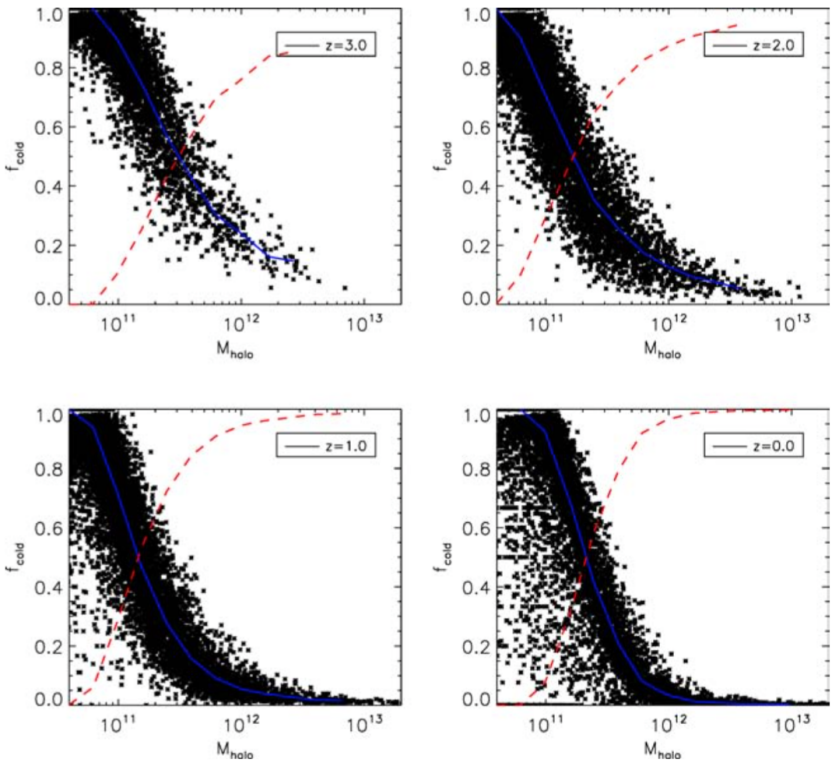

Figure 1.9: Median hot and cold accretion fractions (red and blue lines) as a function of halo mass for a population of galaxies simulated in a large volume box (Kereš et al., 2009). Each point corresponds to individual galaxies and shows that the growth of high-redshift galaxies ($z \geq 2$) is dominated by cold accretion.

since they are driven by the thermal properties of the inflowing gas (Dekel & Birnboim, 2006; Dekel et al., 2009).

1.2.3 Angular momentum of accreting gas

Each mode of accretion has different implications for the evolution and the final distribution of angular momentum in a galaxy (Figure 1.10). When gas is shock-heated to approximately the virial temperature, it spends sufficient time in the halo to mix before eventually cooling onto the galaxy. Feeding a galaxy with cooled gas of the same angular momentum distribution as the dark matter is the foundation of the standard picture of galaxy formation presented in section 1.1.6. The main mode of galaxy formation, however, is the cold mode, which does not necessarily mix with the existing gasous halo, and thus its specific angular momentum does not match well that of the dark matter. In fact, recent observations of the angular momentum of both gas in the disk (Oosterloo et al., 2007; Obreschkow & Glazebrook, 2014) and in the circumgalactic medium (e.g. Bouché et al., 2013) report that the angular momentum of gas is much higher than of the galaxy (or dark matter). It is thus unclear why the predictions of the standard model based on the premise $j_{gas} = j_{DM} = j_*$ such as $R_d = \lambda R_{vir}$ would hold.

Over time, baryons and dark matter are expected to lose its angular momentum through the vector cancellation with other accretion events. It is hence possible that the high angular momentum of cold gas compared with that of dark matter is related to the fact that the dark matter halo represents a cumulative effect of accretion events, while a cold flow is only recent (Stewart et al., 2011, 2013). Further posibilities are related to the physical processes such as cooling and outflows, which have been shown to modify the distribution of angular momentum, for example by redistributing the angular momentum of the streams (Pichon et al., 2011; Kimm et al., 2011).

1.2.4 Evidence of hot gas around galaxies

Hot gas around galaxies is not only a key prediction of galaxy formation in the cold dark matter paradigm, but it also has been invoked as the reason for the confinement of ubiquitous HI clouds (Spitzer, 1956). Moreover, ram pressure stripping off such coronae would explain the gas depletion in Milky Way dwarfs (Gatto et al., 2013). To date, the strong evidence for

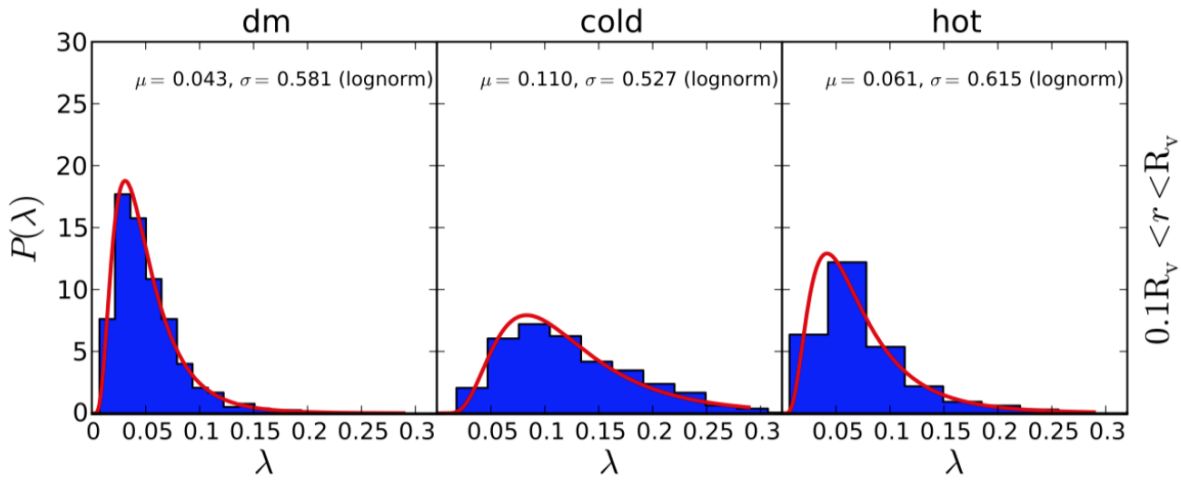

Figure 1.10: The distributions of halo spin parameters excluding the material in the inner 10% of the virial radius among 29 zoom-in simulations across redshifts $z = 4 - 1.5$. On average, the spin parameters of cold gas are significantly higher than of dark matter or hot gas (Danovich et al., 2015; Stewart, 2017).

extended coronae comes from observations of massive spirals (Bogdan et al., 2013; Bogdán et al., 2013), or around low-mass starburst galaxies (Strickland et al., 2004). Studies of extragalactic low-mass spirals fail to detect any significant extraplanar X-ray emission with the current state-of-the-art instruments (Rasmussen et al., 2009). The best evidence of the existence of hot gas comes from our own Galaxy, namely the high-resolution spectra of soft X-ray background (Snowden et al., 1997), and the studies of the OVII and OVIII absorption lines (Miller & Bregman, 2013; Miller & Bregman, 2014).

Chapter 2

Scientific methodology: numerical experiments

The aim of astrophysical numerical experiments is to test underlying models by comparing their outcomes with the observations. The key utility of computer simulations comes from their ability to solve complex systems of equations that are intractable with analytic techniques. Simulations model the system under consideration – be it cosmic scale volumes, or individual halos – as discretised mass elements, which typically amount to more than several million particles. The number of such particles is limited by the speed of calculations, which depends on both the optimization of numerical methods in the astrophysical code and the computing power of national supercomputers. Numerical simulations in the cosmological context cost millions of core-hours (for instance, the Eris [1] zoomed-in simulation of tens of millions particles used in this thesis was evolved for 1.5 million CPU hours), require tens to hundreds of gigabytes of memory, and use up terabytes to petabytes of disk storage. Models discussed in this work are based on the parallel hydrodynamical code GASOLINE (Wadsley et al., 2004) with self-gravity. This section covers the core principles of the numerical simulations of galaxy formation, including the N-body solvers, smoothed particle hydrodynamics and subgrid physics.

[1] Eris simulation was introduced in (Guedes et al., 2011).

2.1 N-body dynamics, tree codes and adaptive leapfrog

According to the ΛCDM paradigm, the matter density of the Universe is composed of baryonic and non-baryonic elementary particles. Hence, a full description of matter in a cosmological volume or individual halos would require following the trajectories of individual elementary particles, resulting in a gigantic computationally unattainable model. However, physical particles can be treated as a continuum fluid, and such fluid can then be viewed as fiducial macro particles that sample phase-space in a Monte-Carlo fashion. Thus, under certain assuptions discussed below, we can describe chunks of Universe as discrete systems composed of far fewer and far more massive elements than in reality (Gnedin et al., 2015).

Macro particles come in different flavors, depending on what forces govern their equations of motion. For example, a galactic halo and its galaxy can be viewed as a system consisting of dark matter, stellar, and gaseous particles. The first two are dissipationless (collisionless), and can be evolved in time with N-body solvers. Mathematically, a system is collisionless if its relaxation time $\mathrm{t_{relax}}$, defined as

$$\mathrm{t_{relax}} \equiv \frac{\mathrm{v}^2}{(\Delta \mathrm{v})^2/\mathrm{t_{cross}}}, \tag{2.1}$$

is much greater than the age of the Universe ($\mathrm{t_{cross}}$ is a ratio of the scale length of the system to its typical velocity). What it means physically is that the individual perturbations on a particle from neighboring particles (Δv) reach a level of the typical squared velocity v of that particle[2] on a time scale (t_{relax}) that is so long that one can neglect interactions between the particles. The relaxation time can be expressed in terms of the number of physical elements in the system N, as $\mathrm{t_{relax}} = \frac{\mathrm{N}}{8 \ln \mathrm{N}} \mathrm{t_{cross}}$. Thus, the following holds for the two components of a galactic system:

- STARS IN A GALAXY: with $\mathrm{N_{stars}} \sim 10^{11}$, $\mathrm{t_{cross}} \sim \frac{10\mathrm{kpc}}{100\mathrm{km/s}} = 0.1\mathrm{Gyr}$, $\mathrm{t_{relax}} \sim 10^{10}\mathrm{Gyr} >> \mathrm{t_{Hubble}} \sim 10\mathrm{Gyr}$.

- DARK MATTER IN A HALO: with $\mathrm{N_{WIMPs}} \sim 10^{77}$ (assuming the dark matter is composed of a ~ 100GeV WIMPs), crossing time $\mathrm{t_{cross}} \sim 0.1 \frac{1}{\mathrm{H_0}}$, $\mathrm{t_{relax}}$ is more than 70 orders of magnitude higher than the age of the Universe.

[2] the velocity perturbations have random orientations, so they add up in quadrature

Collisionless systems can be instantaneously described as a distribution function f($\vec{\mathbf{x}}$,$\vec{\mathbf{v}}$) over the phase space. A phase space density $\rho(\vec{\mathbf{x}}, t)$ reproduces the density and potential Φ of a galaxy at one particular instant. The time evolution of the phase space density is governed by a 6-dimensional equation of continuity, which combined with the equation of motion yields the Collisionless Boltzmann Equation (CBE):

$$\frac{\partial f}{\partial t} + \vec{\mathbf{v}} \cdot \vec{\nabla} f - \vec{\nabla}\Phi \cdot \frac{\partial f}{\partial \vec{\mathbf{v}}} = 0 \tag{2.2}$$

that can be coupled with the Poisson equation

$$\nabla^2 \Phi(\vec{\mathbf{x}}, t) = 4\pi G \rho(\vec{\mathbf{x}}, t) = 4\pi G m \int f(\vec{\mathbf{x}}, \vec{\mathbf{v}}, t) d^3\vec{\mathbf{v}}. \tag{2.3}$$

This set of equations turns the elementary particle description into the continuum fluid. Reintroducing particles on a macro scale (tens to thousands solar masses) has the downside of boosting Newtonian forces upon close approaches. To alleviate this problem, the common practice is to insert the softening length ϵ that eliminates force divergence on close interactions, as below:

$$\Phi(\vec{\mathbf{r}}) = -G \sum_{j=1}^{N} \frac{m_j}{[(\vec{\mathbf{r}} - \vec{\mathbf{r}}_j)^2 + \epsilon^2]^{1/2}}. \tag{2.4}$$

In general, the softening length should be large enough to prevent formation of bound particles and spurious fragmentation, and as small as the computational resources allow (the smaller the softening, the shorter the time steps). Moreover, the softening will determine the force resolution of a simulation, as it equals to the smallest resolved length-scale. Its choice must thus be a compromise between all of the above.

To evolve particles in time, numerical codes integrate the equations of motion of a form

$$\ddot{\vec{\mathrm{x}}} = -\nabla_{\mathrm{i}} \Phi(\mathrm{r_i}), \tag{2.5}$$

using integration schemes for ordinary differential equations (in case of PKDGRAV, an adaptive leapfrog integration scheme, which will be covered below). The straightforward way of solving the right-hand side of the equation 2.5 is direct summation, i.e. computing N forces for N particles ($O(N^2)$). For large numbers of particles, however, the direct summation is

highly ineffcient (e.g. solving them for 10^{10} particles would take 10 million years, Gnedin et al. (2015)). PKDGRAV and GASOLINE use spatial binary trees as fast approximate force calculation schemes (Wadsley et al., 2004).

The basic idea behind tree codes (e.g. Barnes-Hut algorithm) is to use the hierarchical grouping of particles to evaluate the gravitational field (Ventimiglia & Wayne, 2017). The starting point is to build a tree of spatial regions of the simulation with regions occupied by single particles as its end points (the procedure is explained in Figure 2.1, alongside the graphical representation of a tree). A tree consists of multiple levels of nodes, which can be divided into "external nodes" containing a single body, and "internal nodes" representing a group of bodies beneath it. In order to evaluate the gravitational forces acting on any body of the tree, the following procedure is executed. Starting from the root node, which is the highest-level internal node, if the distance between the body and the center of mass of the internal node is sufficiently large, the particles in that internal node can be treated as one single body, whose position is at the center of mass of that node. Otherwise, the condition is evaluated for the nodes in the next levels of the tree recursively, until the condition is met, or the node is external. Mathematically, the condition is controlled by the quotient s/d, with s the width of the node and d the distance body-center of mass of the node, and the threshold value θ which is user-specified. In general, the choice of the threshold value is a trade-off between accuracy and speed of the calculation. When the walk on a tree branch (over the consecutive nodes) is finished, the algorithm calculates the force exerted by the node on the body, adds this amount to body's net force and proceeds with the next branch. This procedure is then repeated for all particles in the simulation. Overall, this algorithm is much faster than the direct summation, and has the speed of order $O(N \log N)$.

Equation 2.5 is a second-order vector equation that can be split into two first-order equations, and thus the orbit integration is fast and accurate (Hutchinson, 2015). This is because the leapfrog scheme conserves energy and momentum, hence long-term energy errors are reasonably small. The integrator consists of two principle operations, called the "drift" and the "kick". The drift moves particles at a position n to $n+1$ with a velocity that is the average velocity between the two positions; the kick accelerates particles at a position $n+\frac{3}{2}$ using an acceleration evaluated at a new step $n+1$. The sequence "drift-kick-drift-kick" is repeated over the span of the simulation. The leapfrog integrator can be written as:

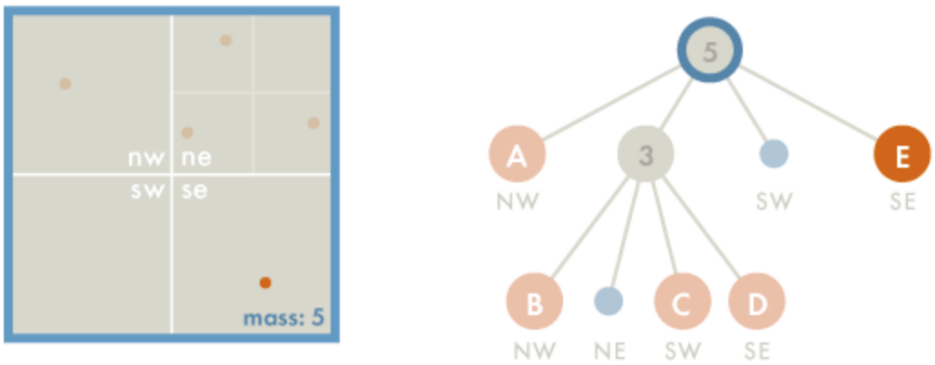

Figure 2.1: The illustration of the Barnes-Hut algorithm. In the first step, all five objects are identified in the root node (blue frame). The node is then divided into subregions (nw, ne, sw, se). Regions which contain one object are saved as "external nodes" of the tree (e.g. A, E), empty regions are discarded (SW), and regions with multiple objects are treated further as "internal nodes". The procedure is repeated recursively on the internal nodes (3) until they become external (B, C, D) (Ventimiglia & Wayne, 2017).

$$\vec{\mathbf{x}}_{n+1} = \vec{\mathbf{x}}_n + \frac{1}{2}\vec{\mathbf{v}}_{n+1/2}\Delta t \tag{2.6}$$

$$\vec{\mathbf{v}}_{n+3/2} = \vec{\mathbf{v}}_{n+1/2} + \vec{\mathbf{a}}_{n+1}\Delta t \tag{2.7}$$

where $\vec{\mathbf{x}}$ is the position vector of a particle, $\vec{\mathbf{v}}$ is the velocity, $\vec{\mathbf{a}}$ is the acceleration, and Δt is the timestep. Before the integrator is initialized, the following equation

$$\vec{\mathbf{v}}_{1/2} = \vec{\mathbf{v}}_0 + \vec{\mathbf{a}}_0\frac{t_1 - t_0}{2} \tag{2.8}$$

constructs a half-step in velocity, which is a necessary operation, given that velocities in this method are time-shifted with respect to the positions and accelerations.

As mentioned above, PKDGRAV uses an adaptive leapfrog integrator (Quinn et al., 1997), which accounts for density contrasts between particles when assigning a timestep to a particle, and thus saves computational time (shorter Δt for low densities). This method adjusts timesteps of the individual particles according to their dynamical time, i.e. $\Delta t < \frac{\eta}{\sqrt{G\rho}}$, with η being a numerical coefficient ($\eta = 0.3$ ensures the stability of integration), ρ the estimate of the local density, and G the gravitational constant. As particles can be on different timesteps, to ensure synchronization, all timesteps are the power-of-two subdivision of the

largest timestep Δt_s, i.e. $\Delta t_i = \frac{\Delta t_s}{2^{n_i}}$, with n_i being the integer number of the rung for the timestepping. The adaptive leapfrog integrator is not symplectic but has proven to achieve an order-of-magnitude gains in performance with respect to the traditional symplectic leapfrog scheme.

2.2 Collisional astrophysical fluid and SPH

The previous section focused on describing the methodology behind modelling the collisionless systems, which comprise cold dark matter and stellar particles. Gas, however, is the main fluid component in the Universe, i.e. a collisional medium with well-defined macroscopic properties (such as density and pressure). Gas can dissipate energy, shock-heat, and is a subject to various fluid instabilities (e.g. buoyancy-driven Rayleigh-Taylor, vortex-generating Kelvin-Helmholtz). Its evolution is governed by the fluid equations, which are based on the concept of a fluid element. A fluid element is a region of the fluid, size of which is assumed to be large compared to the mean free path[3] of the particles making the fluid (i.e. the state of the element reflects the local conditions of physical particles colliding with each other), but small compared to the length scale over which the fluid properties vary (i.e. we can ignore systematic variations across it) (Clarke & Carswell, 2007; Draine, 2010). The fluid equations in the Lagrangian form (i.e. in the reference frame of the fluid element) comprise the continuity, momentum and energy equations listed below:

$$\frac{d\rho}{dt} + \rho\vec{\nabla}\cdot\vec{\mathbf{v}} = 0 \tag{2.9}$$

$$\rho\frac{dv}{dt} + \vec{\nabla}p - \rho\vec{\mathbf{g}} = 0 \tag{2.10}$$

$$\frac{d\varepsilon}{dt} + \frac{p}{\rho}\vec{\nabla}\cdot\vec{\mathbf{v}} = 0, \tag{2.11}$$

where ρ, $\vec{\mathbf{v}}$, p, $\vec{\mathbf{g}}$, and ε are the density, velocity, pressure, gravitational acceleration, and the total energy per unit mass (thermal u and kinetic $v^2/2$), respectively. Those equations convey three fundamental principles:

1. *continuity equation (2.9):* in the absence of sources or sinks for matter, the mass of fluid in the comoving volume of the fluid element is constant;

[3]The mean free path is the average distance traveled by a moving particle between successive collisions.

2. *momentum equation (2.10):* the momentum of a fluid changes as a result of pressure gradients and gravitational forces;

3. *energy equation (2.11):* the rate of change of energy inside the fluid element equals to the net flux of heat into the element.

Particles in a fluid interact with each other and attain a well-defined distribution of particles speeds, that can be described by means of the equation of state. For an ideal gas, the pressure law is

$$P = (\gamma - 1)\rho u, \tag{2.12}$$

with γ being the ratio of specific heats, equal to 5/3 for a monoatomic gas.

These equations describe the *ideal fluid*, hence neglect the internal friction of a fluid. In regimes, where viscosity is important, eq. 2.10) and 2.11) are modified to include the terms transfering momentum and dissipating relative motions of the fluid into heat (Navier-Stokes equations, see reference Gnedin et al., 2015).

The astrophysical code GASOLINE uses a smoothed particle hydrodynamics (SPH) technique to approximate the continuum dynamics of fluids (Gingold & Monaghan, 1977; Lucy, 1977; Monaghan, 1992). SPH equations of motion are the same as in eqs. 2.9, 2.10, 2.11. SPH follows the evolution of smoothly varying fluid quantities that are represented by the discrete gas particles (particles carry physical properties such as position, velocity, and mass). The smooth fluid is recovered from this macro discretization through local summation of the particles with a smoothing kernel, W (Stadel et al., 2002; Wadsley et al., 2004). For some quantity f of a particle i and its neighbours j, this means

$$f_{i,smooth} = \sum_{j=1}^{n} f_j W_{ij}(\vec{\mathbf{r}}_i - \vec{\mathbf{r}}_j, h_i, h_j), \tag{2.13}$$

where W_{ij} is a kernel function, h_j a smoothing length (a scale length beyond which the kernel becomes negligible), and $\vec{\mathbf{r}}_j$ the positions of particles. The smoothing length h_i is set equal to the half of the distance to the 32-nd nearest neighbour from the particle i (the minimum smoothing length allowed is equal to the gravitational softening). The kernel function W is symmetric ($W_{ij} = W_{ji}$) and has the form of

$$W_{ij} = \frac{1}{2} w(|\vec{\mathbf{r}}_i - \vec{\mathbf{r}}_j|/h_i) + \frac{1}{2} w(|\vec{\mathbf{r}}_i - \vec{\mathbf{r}}_j|/h_j), \tag{2.14}$$

where $w(x)$ is a normalised spherical kernel with compact support (Monaghan, 1992) described as

$$w(x) = \frac{1}{\pi h^3} \begin{cases} 1 - (3/2)x^2 + (3/4)x^3, & 0 \leq x \leq 1 \\ (2-x)^3/4, & 1 < x \leq 2 \\ 0, & x > 2 \end{cases} \tag{2.15}$$

The equations of SPH in the form presented above keep the entropy strictly constant[4]. However, at the shock front, the entropy of the gas always increases, which means that gas dynamics is no longer inviscid. The dissipation of kinetic energy into heat and the production of entropy is introduced in SPH by means of the *artificial viscosity*, and parametrized in terms of a friction force that damps the relative motions of particles. The artificial viscosity term Π_{ij} is usually given by

$$\Pi_{ij} = \begin{cases} \frac{-\alpha c_{ij}\mu_{ij} + \beta\mu_{ij}^2}{\rho_{ij}}, & \vec{\mathbf{v}}_{ij} \cdot \vec{\mathbf{r}}_{ij} < 0 \\ 0 & \text{otherwise} \end{cases} \tag{2.16}$$

with

$$\mu_{ij} = \frac{h_{ij}\vec{\mathbf{v}}_{ij} \cdot \vec{\mathbf{r}}_{ij}}{|\vec{\mathbf{r}}_{ij}|^2 + \epsilon h_{ij}^2}. \tag{2.17}$$

The terms h_{ij}, ρ_{ij}, c_{ij} denote arithmetic means of the smoothing lengths, densities and sound speeds of particles i and j, respectively. Vectors $\vec{\mathbf{r}}_{ij} = \vec{\mathbf{r}}_i - \vec{\mathbf{r}}_j$ and $\vec{\mathbf{v}}_{ij} = \vec{\mathbf{v}}_i - \vec{\mathbf{v}}_j$. The strength of the viscosity is controlled by the parameters $\alpha = 1$ and $\beta = 2$ for the terms representing shear and von Neuman-Richtmyer viscosities, correspondingly. The viscosity term enters the momentum and energy equations:

$$\frac{d\vec{\mathbf{v}}_i}{dt} = -\sum_{j=1}^{n} m_j \left(\frac{P_i}{\rho_i^2} + \frac{P_j}{\rho_j^2} + \Pi_{ij} \right) \nabla_i W_{ij} \tag{2.18}$$

$$\frac{du_i}{dt} = \sum_{j=1}^{n} m_j \left(\frac{P_i}{\rho_i^2} + \frac{1}{2}\Pi_{ij} \right) \vec{\mathbf{v}}_{ij} \cdot \nabla_i W_{ij} \tag{2.19}$$

The viscosity should be activated only when the shock is present, however, even in this form the numerical method cannot distinguish purely adiabatic compression from that in shock, leading to a relatively high numerical viscosity of SPH.

The timestepping in GASOLINE, similarly to PKDGRAV, takes into account differences

[4]GASOLINE does not enforce entropy conservation, and it uses internal energy as a variable. For more details on the latest formulation, GASOLINE2, see Wadsley et al. (2017).

in densities of particles in order to speed up the calculations. However, there are a few fundamental differences between the timestepping in N-body and SPH simulations, e.g.: 1) the dynamical timescale for gravity scales as $\rho^{-1/2}$ and for gas as $\rho^{-1/3}T^{-1/2}$; 2) for SPH, not only the positions but also thermal energies and velocities influence the choice of a timestep (Wadsley et al., 2004). GASOLINE incorporates the Kick-Drift-Kick scheme described above for PKDGRAV with additional timestep criteria:

$$\begin{aligned} dt_{Accel} &\leq 0.3\sqrt{\frac{a}{\epsilon}} \\ dt_{Courant} &\leq 0.4\frac{h}{(1+\alpha)c + \beta\mu_{max}} \\ dt_{Expand} &\leq 0.25\frac{u}{du/dt} \qquad \text{if} \quad du/dt < 0, \end{aligned} \tag{2.20}$$

where ϵ and a are particle's softening length and acceleration; μ_{max} is the maximum value of μ_{ij} (eq. 2.17). Three constraints on the timestep follow from the particle's acceleration, the Courant condition[5] and the expansion cooling rate.

2.3 Subgrid physics

Sub-resolution physics is a direct consequence of the macro-particle methodology, since simulations are not able to resolve ISM or individual stars. The heuristic models for star formation, stellar feedback, cooling of gas and other physical processes in GASOLINE are briefly described below. More details can be found in (Stinson et al., 2006; Shen et al., 2010).

Star formation. Stars are generated probabilistically in order to match the observational Schmidt law:

$$\Sigma_{SFR} \propto (\Sigma_{gas})^n, \tag{2.21}$$

where $n = 1.4$ (Stinson et al., 2006). A part of the parent gas particle will turn into a star particle, provided that the gas particle i is: 1) denser than the star formation number density threshold n_{SF}; 2) a part of an overdense region ($\rho_i/\rho_{min} \geq 55$); 3) a part of a convergent

[5] $|v|\Delta t/\Delta r \leq 1$; breaking this condition implies that information is propagating faster than a particle changes its position Δr in a time step of a simulation Δt.

flow

$$\nabla \cdot \vec{\mathbf{v}} = \frac{1}{\rho_i} \sum_{j=1}^{n} m_j (\vec{\mathbf{v}}_j - \vec{\mathbf{v}}_i) \cdot \nabla_i W_{ij} < 0; \tag{2.22}$$

4) Jeans unstable, meaning the pressure inside the smoothing sphere cannot provide support against the gravitational collapse, i.e.

$$\frac{h_i}{c_i} > \frac{1}{\sqrt{4\pi G \rho_i}} \tag{2.23}$$

with G being the gravitational constant. This condition can also be expressed as the temperature threshold T_{max}, beyond which a gas particle cannot form stars. The probability that a star will form is expressed as

$$p = \frac{m_i}{m_*} \left(1 - e^{-c^* \Delta t / t_{form}}\right), \tag{2.24}$$

where m_i, m_* are masses of the parent particle and a new star, respectively, t_{form} is the dynamical time, and c^* is a constant star formation efficiency factor that follows from the definition of the star formation rate (SFR)

$$\frac{d\rho_*}{dt} = c^* \frac{\rho_i}{t_{form}}, \tag{2.25}$$

and can be adjusted in order to match the observed values of SFR. Each newly born particle represents a population of stars with a distribution governed by the initial mass function (IMF). For the purpose of this work, two different IMFs are utilized (Kroupa et al., 1993; Kroupa, 2001). The difference between them is presented in Figure 2.2.

Stellar feedback. GASOLINE includes stellar feedback from SNIa and SNII. The number of supernovae that explode in a stellar particle depends on the choice of the initial mass function. Generally, stars with masses between 8 and 40 $M_\odot$ are exploding as SN II. The total feedback energy released by a stellar particle equals to the number of supernovae multiplied by the energy released by a single explosion (a fraction of the canonical 10^{51} erg controlled by the SN feedback efficiency parameter, E_{SN}). This energy is then distributed within the kernel of a particle among its neighbours, and is weighted by the mass of the gas

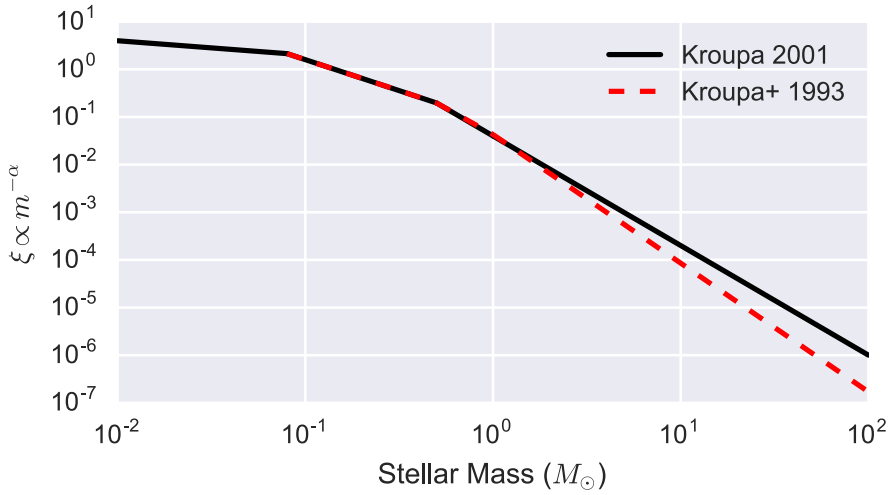

Figure 2.2: A diagram showing the initial mass functions used in this thesis. The distribution of stellar masses ξ is proportional to $m^{-\alpha}$, with m being the stellar mass, α the parameter controling a slope of the distribution. Note the more recent IMF (2001) implies more stars at the high-mass end.

particle that receives it. The energy received by a gas particle i is thus

$$\Delta E_{SN,i} = \frac{m_i W(|\vec{\mathbf{r}}_i - \vec{\mathbf{r}}_s|, h_s)\Delta E_{SN}}{\sum_{j=1}^{n} m_j W(|\vec{\mathbf{r}}_j - \vec{\mathbf{r}}_s|, h_s)} \tag{2.26}$$

where h_s is the distance from the stellar particle to its 32nd nearest gas particle, and ΔE_{SN} is the total feedback energy. SNII also return metals and mass to the gas particles in a similar way to the equation 2.26. Another source of metals comes from SNIa, which are assumed to eject fixed mass of iron and oxygen to the surrounding medium. As in case of SNII, the energy and mass of SNIa are distributed among neighbouring gas particles within a smoothing kernel (more details in Stinson et al. (2006)).

Gas in high-density regions can typically radiate away the energy of supernovae on the time scales shorter than one time step, which can be mitigated by disabling the radiative cooling for a short period of time. This inhibits star formation (as it mimics turbulence in molecular clouds), and allows the energy to flow outwards (models high pressure of a blastwave). In every time step, each gas particle has its cooling shutoff time calculated from the total SN energy received according to the following recipe (Stinson et al., 2006).

The cooling shut-off time follows from the explicit blastwave solution, which determines the maximum radius of the blastwave[6],

$$R_E = 10^{1.74} E_{51}^{0.32} n_0^{-0.16} P_{04}^{-0.2} \text{ pc}, \tag{2.27}$$

and the time that the blastwave will keep the gas hot[7], i.e.

$$t_{max} = 10^{6.85} E_{51}^{0.32} n_0^{0.34} P_{04}^{-0.7} \text{ yr}, \tag{2.28}$$

where $E_{51} = E_{SN}/10^{51}$ erg, n_0 is the ambient hydrogen density, $P_{04} = 10^{-4} P_0 k^{-1}$ with P_0 the ambient pressure and k the Boltzmann constant.

Cooling is switched off temporarily for particles within R_E (but in no more than 32 particles), and for the time t_{max}. The cooling shut-off time physically corresponds to the sum of the period of inefficient cooling (Sedov phase), and the momentum-conserving blastwave expansion time, over which the low-density hot shell can still survive (the snowplow phase).

Gas cooling. The standard version of GASOLINE incorportates Compton cooling, atomic cooling and metallicity-dependent radiative cooling at low temperatures. Cooling and heating rates of primordial gas are derived from the ioniation equations of the Minimal Model[8] in the presence of a uniform UV background. Cooling at temperatures below 10^4 K is assumed to come from the fine structure and metastable lines of C, N, O, F e, S, Si (Mashchenko et al., 2007). The latest version of GASOLINE includes metal line cooling down to 100 K with cooling rates computed with CLOUDY (Ferland et al., 1998). Those rates are determined for 30 first elements in the periodic table and under the assumption of ionization equilibrium. The built-in UV background includes extragalactic radiation from both quasars and galaxies (Shen et al., 2010).

[6]Result from simulations of Chevalier (1974).

[7]Based on McKee & Ostriker (1977).

[8]this model describes 12 processes sufficient to model abundances of $H, He, H^+, H^-, He^+, He^{++}, H_2$ for the lowdensity ($n < 10^4$ cm^{-3}) primordial gas (Abel et al., 1997)

2.4 ICs and the cosmological context

Generating initial conditions boils down to choosing a background cosmological model (here, ΛCDM) and imposing perturbations on this background, assuming a finate periodic volume (the Universe is homogeneous and isotropic on large enough scales). The perturbations of dark matter and baryons are specified by a power spectrum $P(k)$ with an index n controlling its shape. Inflation predicts that those fluctuations can be characterized as a Gaussian random field. The cosmological density field is described by

$$\delta(x) = \int d^3k e^{i\vec{\mathbf{k}}\vec{\mathbf{x}}} T(k)\xi(\vec{\mathbf{k}}) \tag{2.29}$$

with $\delta(x)$ the deviations from the average background density, $\xi(x)$ Gaussian white noise, and $T(k)$ transfer function related to the power spectrum by $T(k) = [P(k)]^{1/2}$. The density perturbations are imposed on a uniform grid in the form of density and velocity fields, obeying the Zeldovich approximation (Mo et al., 2010).

Zoom-in technique. This technique allows to simulate a region of a cosmological box with higher resolution, and adds smaller scale perturbations. After the selection of a target region, the new initial conditions with an improved mass resolution are generated on a nested grid in a Lagrangian sub-region. It is important to ensure that the white noise in each higher refinement level has the same long-wave properties as the coarser grid.

Generating cosmological initial conditions for the hierarchical set of nested regions can be done with the code MUSIC (MUlti-Scale Initial Conditions, Hahn & Abel (2011)), in the following steps.

1. Setting up initial conditions with MUSIC for the dark matter only and on the uniform grid.

2. Running the simulation to desired redshift.

3. Identifying the region of interest at that redshift, and tracing its particles to the initial conditions (positions and velocities in the Lagrangian patch).

4. Adding baryons and resampling that Lagrangian patch with the desired resolution.

Expanding background. In the cosmological simulations, the background space is uniformly expanding with time. This implies a necessity to include a modification to the equations of motion involving the scale factor a

$$\ddot{\vec{\mathrm{x}}} = -2\frac{\dot{a}}{a}\dot{\vec{\mathrm{x}}} - \frac{\nabla_x \Delta\Phi}{a^2}. \tag{2.30}$$

The above equations of motion are locally Newtonian within an expanding FLRW background.

Chapter 3

The Galaxy-Halo Connection

Sokolowska, A., Capelo, P. R., Fall, S. M., et al. 2017, ApJ, 835, 289.

3.1 Abstract

We investigate the angular momentum evolution of four disk galaxies residing in the Milky Way-sized halos formed in cosmological zoom-in simulations with varying sub-grid physics and merging histories. We decompose these galaxies kinematically and photometrically, into their disk and bulge components. The simulated galaxies and their components lie on the observed sequences in the j_*–M_* diagram relating the specific angular momentum and mass of the stellar component. We find that galaxies in the low-density environments evolve on straight lines in the $\log j_*$–$\log M_*$ diagrams past major mergers, in the case of strong feedback following the relation $j_* \propto M_*^{\alpha}$ with $\alpha \sim 0.6$, when bulge-to-disk ratios are relatively constant, and in the two other cases with $\alpha \sim 1.4$, when secular processes operate on shorter timescales. The ratio of the specific angular momentum of stars and dark matter, i.e. the retention factor, highlights that the angular momentum of disk-dominated galaxies is nearly conserved. We compute the retention factors for both the disk and bulge components as a function of time and show that, unless a system undergoes multiple major mergers, the retention factors of disks are always close to unity. Our results indicate that, after averaging over numerous but brief fluctuations, galaxies and their halos grow approximately homologously with each other.

3.2 Introduction

The mass M and angular momentum J are two of the most basic properties of galaxies. For many purposes, it is more convenient and physically meaningful to describe galaxies in terms of their mass M and specific angular momentum $j \equiv J/M$ (for the stellar parts of galaxies, we denote these quantities by j_* and M_*). Galaxies of the same disk-to-spheroid ratio or morphological type at redshift $z = 0$ obey scaling relations of the form $j_* \propto M_*^{\alpha}$, with $\alpha \sim 2/3$ (Fall, 1983; Romanowsky & Fall, 2012; Fall & Romanowsky, 2013). In a plot of $\log j_*$ against $\log M_*$, disk-dominated (Sc, Sd) galaxies and spheroid-dominated (E) galaxies lie along roughly parallel sequences of slope $\sim$2/3 separated by a factor of $\sim$5 in j_* at each M_*. Galaxies of intermediate types (Sb, Sa, and S0) populate the region between these sequences.

The observed sequence of disk-dominated galaxies at $z = 0$ in the j_*–M_* diagram is close to the predictions of a simple analytical model in which baryons and dark matter are endowed with approximately the same specific angular momentum by tidal torques in the early stages of galaxy formation and this is assumed to hold later for disks and halos, at least in total if not for each element of material[1] (Fall & Efstathiou, 1980; Fall, 1983; Mo et al., 1998). Disk-dominated galaxies at high redshift ($0.2 < z < 3$) also appear to obey this simple model (Burkert et al., 2016; Contini et al., 2016). Moreover, the sizes of galactic disks, another reflection of their angular momenta, are consistent with this model, both at $z = 0$ (Kravtsov, 2013) and at $0 < z < 3$ (Huang et al., 2016).

Over the past two decades, there have been many attempts to reproduce the observed j_*–M_* sequences in hydrodynamical simulations of galaxy formation. Until recently, most of these simulations produced galaxies that lay closer to the spheroid-dominated sequence than to the disk-dominated sequence (e.g Navarro & Steinmetz, 1997; Weil et al., 1998; Abadi et al., 2003; Stinson et al., 2010). The failure of the early simulations to reproduce the observed disk-dominated sequence has been called the 'angular momentum problem'. It is another manifestation or close relative of the 'over-cooling problem'.

The situation has changed dramatically in the past few years as a result of greater computing power, better numerical techniques, and the inclusion of more realistic physical pro-

[1]This is based on the "weak" form of conservation of specific angular momentum in total, rather than the more restrictive "strong" form, which requires conservation of the specific angular momentum of each element of material. See Fall (2002) for further discussion.

cesses in the simulations. Some of the simulations are now capable of producing respectable galactic disks (e.g. Guedes et al., 2011; Agertz et al., 2011; Marinacci et al., 2014a; Roškar et al., 2014). Feedback – the injection of momentum and/or energy into the interstellar and/or circumgalactic media (ISM and CGM) – appears to be crucial (Governato et al., 2007; Zavala et al., 2008). Some physical processes cause losses in specific angular momentum (e.g. galaxy mergers; Jesseit et al., 2009; Capelo & Dotti, 2016), while others cause gains (e.g. galactic fountains; Übler et al., 2014). At the same time, increased mass and spatial resolution have reduced numerical artefacts responsible for spurious angular momentum losses in galactic disks (Okamoto et al., 2003; Kaufmann et al., 2007). The most recent generation of large-volume hydrodynamical simulations of galaxy formation have succeeded, at least approximately, in reproducing the observed sequences of disk-dominated, spheroid-dominated, and intermediate-type galaxies (Genel et al., 2015; Pedrosa & Tissera, 2015; Teklu et al., 2015; Zavala et al., 2016). Evidently, for disk-dominated galaxies, the gains and losses mostly cancel out, leading to an apparent, if not strict, conservation of specific angular momentum.

The large-volume hydrodynamical simulations, with typical dimensions ∼100 Mpc, produce many thousands of galaxies, more than enough to define the j_*–M_* relations over wide ranges of mass and disk-to-spheroid ratio. The price paid for these large volumes and galaxy populations, however, is relatively low mass and spatial resolution, typically $\sim 10^7$ $M_\odot$ and ∼kpc. Many of the most important physical processes, particularly those involving transport of radiation, mass, and momentum or energy, are affected strongly by the structure of the ISM and CGM on much smaller scales. To take only one example among many, the formation of star clusters and their resulting feedback occurs in some of the densest parts of the ISM, the so-called clumps, with typical masses $\sim 10^2$–10^6 $M_\odot$ and dimensions ∼pc.

These complicated, and only partially understood, small-scale processes are dealt with in the hydrodynamical simulations of galaxy formation by approximate sub-grid prescriptions rather than by direct solution of the relevant dynamical equations. Given the large mismatch of scales, the use of sub-grid modules is likely to be necessary in this field for the foreseeable future. Thus, it is important to analyze simulations with different resolution, numerical techniques, and sub-grid prescriptions, especially for star formation and feedback by both young stars and active galactic nuclei (AGN), to determine which results depend sensitively on these features and which are robust. In this respect, high-resolution zoom-in

simulations of the formation and evolution of individual galaxies are a valuable complement to the large-volume simulations of galaxy populations. In particular, they allow for a more detailed and reliable study of the processes causing gains and losses of specific angular momentum. Recently, zoom-in simulations have been able to capture even subtle internal dynamical processes occurring in disks, from non-axisymmetric instabilities such as bars to radial migration of stars, and their interplay with other galaxy properties such as the age of stellar populations (Brook et al. 2011; Bird et al. 2013; Guedes et al. 2011; Guedes et al. 2013; Gabor & Bournaud 2013; Stinson et al. 2013; Bonoli et al. 2016; Spinoso et al. 2016). This brings confidence in re-addressing the theme of angular momentum of galaxies using the latest generation of zoom-in simulations.

In this and a companion paper (hereafter papers I and II), we report on a study of the angular momentum in four high-resolution zoom-in simulations of galaxy formation and evolution. The focus of paper I is on the evolution of the stellar components – the disks and spheroids – of these galaxies in the j_*–M_* diagram from the beginning of the simulations at redshift $z \sim 100$ all the way to the end at $z = 0$. The focus of paper II is on the evolution of the inflowing, outflowing, and circulating gas, in different ranges of density and temperature, how it gains and loses specific angular momentum, and how this accounts for the evolution of the stellar components. Running the simulations all the way to $z = 0$ is crucial, because their behavior changes in important ways at $z \sim 1$. Our study is similar in spirit to the recent analyses of high-resolution zoom-in simulations by Fiacconi et al. (2014), Danovich et al. (2015), and Agertz & Kravtsov (2016).

The plan for the remainder of this paper is the following. In Section 3.3, we describe our simulations. In Section 3.4, we decompose the galaxies into disks and spheroids. In Section 3.5, we plot galaxies and their components in the j–M diagram at $z = 0$ and at higher redshifts. In Section 3.6, we study the relation between the specific angular momentum of galaxies and their dark halos. Finally, in Section 3.7, we discuss and summarize our conclusions. The adopted cosmological parameters in all four simulations are $\Omega_{\rm M} = 0.24$, $\Omega_\Lambda = 1 - \Omega_{\rm M}$, $\Omega_{\rm b} = 0.042$, $H_0 = 73$ km s^{-1} Mpc^{-1}, $n_{\rm s} = 0.96$, and $\sigma_8 = 0.76$, based on the first three years of data from the Wilkinson Microwave Anisotropy Probe (Spergel et al., 2007).

3.3 Simulations

We use four unique high-resolution simulations of spiral galaxies performed with the tree-smoothed particle hydrodynamics (SPH) code GASOLINE (Wadsley et al., 2004) with mass resolution $m_{\rm dm} \simeq 9.8 \times 10^4$ M$_\odot$ and $m_{\rm SPH} \simeq 2 \times 10^4$ M$_\odot$, and spatial resolution $\simeq 120$ pc. These runs are all cosmological zoom-in simulations of Milky Way-sized galaxies. The zoom-in technique (Katz & White, 1993) is well established numerically after more than two decades from its introduction, but care has to be taken in building the initial conditions to avoid numerical artifacts which could affect the dynamics. For the simulations presented here, the original periodic low-resolution box from which the initial conditions were subsequently refined is much larger than the Lagrangian subvolume that was selected for the refinement. The large-scale box has indeed a size of 90 Mpc as opposed to about 1 Mpc for the Lagrangian high-resolution subvolume at $z = 0$ (different for Venus, being 60 Mpc and 0.2 Mpc, respectively). The total number of particles in the box of Eris is 53 million (including 13 million of gas), whereas the box of Venus has 170 million particles (16 million of gas).

While the base box is larger than in other published zoom-in simulations, as explained in Katz & White (1993), Mayer et al. (2008), and Governato et al. (2004), choosing a large enough box for the coarsely resolved region is important because lack of large-scale power may bias the angular momentum of collapsing halos. In building the initial conditions we also checked that the spin parameter of the selected halo remains essentially unchanged as we introduce successive refinements.

Run	UVB	IMF	$n_{\rm SF}$	$\epsilon_{\rm SN}$	MC	AGN	IC
Eris	HM96	K93	5	0.8	low-T	no	Q
Venus	HM96	K93	5	0.8	low-T	no	A
EBH	HM96	K93	5	0.8	low-T	yes	Q
E2k	HM12	K01	100	1.0	all-T	no	Q

Table 3.1: Input parameters of the runs. Notation: UVB – UV background (HM96: Haardt & Madau 1996, HM12: Haardt & Madau 2012), IMF – initial mass function (K93: Kroupa et al. 1993, K01: Kroupa 2001), $n_{\rm SF}$ – star formation density threshold, $\epsilon_{\rm SN}$ – SN efficiency parameter, MC – metal cooling, AGN – AGN feedback, and IC – initial conditions (Q: quiet merger history, A: active merger history).

One of the runs, Eris, has been shown to be extremely successful in recovering various

properties of late-type spirals such as the Milky Way (Guedes et al., 2011). The other runs comprise two which stem from the same initial conditions but have different sub-grid models, and a fourth one with different initial conditions. They are, in order: Eris2k (hereafter E2k, described in more detail in Sokołowska et al. 2016) for which sub-grid parameters were tuned to yield a stronger effect of supernova (SN) feedback to lower star formation rates at high redshift; ErisBH (hereafter EBH) being a replica of Eris that includes AGN feedback and yields final correlations between galaxy properties and the mass of the central supermassive black hole that are in good agreement with those of late-type spirals (Bonoli et al., 2016); and Venus, with the same sub-grid physics as the original Eris but different initial conditions, chosen to have an active merging history down to low redshift in contrast with the quiet merging history of the other three runs but also a nearly identical final virial halo mass ($\sim 8 \times 10^{11}$ $M_\odot$) and halo spin parameter ($\lambda \sim 0.03$). Some important simulation parameters of all runs, including the choice of the UV background and aspects of the sub-grid physics, are listed in Table 5.1 and discussed below.

All runs include radiative and Compton cooling. However, in Eris, EBH, and Venus gas cooling is computed for a simple mixture of H and He via non-equilibrium cooling rates in the presence of the ionizing cosmic ultraviolet (UV; Haardt & Madau 1996) background (Wadsley et al., 2004). Additionally, gas of $T < 10^4$ K cools through fine structure and metastable lines of C, N, O, Fe, S, and Si (Bromm et al., 2001; Mashchenko et al., 2007). In E2k we instead account for metal-line cooling at all temperatures, employing tabulated rates computed with the code CLOUDY (Ferland et al., 1998), which assumes that metals are in ionization equilibrium (Shen et al., 2010) in the presence of an updated cosmic ionizing background (Haardt & Madau, 2012).

The recipes for star formation and SN feedback are the same in all the runs and are described in Stinson et al. (2006). Gas particles must be dense – namely have a density above the threshold $n_{\rm SF}$ (set to 100 atom cm^{-3} in E2k and 5 atom cm^{-3} in the other runs) – and cool (cooler than $T_{\rm max} = 1$–3×10^4 K) in order to form stars. Particles which fulfill these requirements are stochastically selected to form stars according to $dM_*/dt = c^* M_{\rm gas}/t_{\rm dyn}$, where M_* is the mass of stars created, c^* is a constant star formation efficiency factor (set to 0.1 in all runs), $M_{\rm gas}$ is the mass of gas creating the star, and $t_{\rm dyn}$ is the gas dynamical time. Each star particle then represents a population of stars, covering the entire initial mass function (IMF; listed in Table 5.1).

Stars larger than 8 $M_\odot$ explode as SNII. According to the "blastwave feedback" model of Stinson et al. (2006), feedback is purely thermal, as the blastwave shocks convert the kinetic energy of ejecta into thermal energy on scales smaller than those resolved by our simulations. Once energy is ejected (the fraction of SN energy that couples to the interstellar medium is $\epsilon_{\rm SN} = 1.0$ in E2k and 0.8 in the remainder), particles receiving the energy are prevented from cooling for typically 10–50 Myr, with the cooling shut-off timescale being computed as the sum of the Sedov–Taylor (Taylor, 1950; Sedov, 1959) and snow-plough phases in the ejecta (McKee & Ostriker, 1977). By delaying the cooling we model in a phenomenological way the unresolved effect of momentum and heating by turbulent dissipation in the ejecta before they reach the radiative phase. The strength of feedback depends on the number of SNe produced, which is in turn governed by the IMF and, locally, by the star formation density threshold.

The IMF in Eris, EBH, and Venus was based on Kroupa et al. (1993), whereas in E2k an updated IMF was used (Kroupa, 2001) which yields about a factor of 2.8 more SNe at equivalent star formation rate. Furthermore, as explained in detail in Guedes et al. (2011) and Mayer (2012), the local star formation rate, and thus the local effect of SNe, can be boosted significantly by raising the star formation density threshold as the interstellar medium is allowed to become more inhomogeneous, an effect that saturates only at very high resolution and density thresholds, well above those resolved with cosmological simulations (Hopkins et al., 2012). This implies that in E2k heating by SN feedback is boosted both globally and locally. We recall that E2k is a run that follows an extensive study of sub-grid parameters by running many different simulations with the same Eris-type initial conditions in order to determine the combination of parameters that yields realistic stellar masses in accordance with abundance matching at both high and low redshift, these being shown in Table 5.1. Indeed in the original Eris suite the conversion of gas into stars was too efficient at high redshift, although final stellar masses at $z = 0$ are in agreement with abundance matching (see also Agertz & Kravtsov, 2015; Sokołowska et al., 2016). E2k also has a richer inventory of physical processes, not only metal-line cooling but also a sub-grid turbulent diffusion prescription for both metals and thermal energy which allows mixing to be captured in SPH (Shen et al., 2010).

The EBH run improves the physical model in the simulations in a different direction as it includes prescriptions for the formation, growth and feedback of supermassive black

holes, and assumes "quasar mode" thermal feedback with Bondi-Hoyle-Lyttleton accretion (Bondi 1952; Bondi & Hoyle 1944; Hoyle & Lyttleton 1939; for more details, see Bellovary et al. 2010; Bonoli et al. 2016), while all the rest of the sub-grid modeling and the cooling is identical to that of Eris.

The Venus simulation employs different initial conditions. The "zoom-in" was initialized using the MUSIC code (Hahn & Abel, 2011), rather than with GRAFIC2 (Bertschinger, 2001) as in the other cases, which allows a computationally more efficient topological identification of the Lagrangian subvolume for the refinement. In contrast to other runs with a quiet merger history, we selected the halo of Venus to have a very active merging history. Its last major merger, which is nearly equal-mass, occurs at $z = 0.9$, as opposed to $z = 3.1$ in the other runs.

3.4 Disk–bulge decompositions

We begin with characterizing the structure of our simulated galaxies by extracting a bulge and a disk component with complementary methods. We perform the decompositions of the simulated spiral galaxies at the final redshift $z_{\rm end}$ of each simulation ($z_{\rm end} = 0$ for Eris, EBH, and Venus; $z_{\rm end} = 0.3$ for E2k). The first decomposition is based on the kinematics of the stellar population in the spherical region characterized by a radius of 15 comoving kpc around the center, which is located at the minimum of the potential well of the galactic halo. We chose this radius as the limit, upon a visual inspection of the extent of the galaxies at $z = z_{\rm end}$ in the stellar-mass density maps.

In Figure 3.1, we show four distributions of the circularity parameter $\epsilon \equiv j_{\rm z}/j_{\rm c}$, where $j_{\rm z}$ is the z-component of the angular momentum vector of a stellar particle when the galactic disk lies in the x–y plane, and $j_{\rm c}$ is the angular momentum of that same stellar particle if it were on a circular orbit in the potential well of the host halo. One expects the distribution of the circularity parameter, $f(\epsilon) \equiv dN/d\epsilon$ (where N is the number of particles in a given circularity bin), to show two peaks in a typical spiral galaxy – one at $\epsilon \simeq 1$ corresponding to the particles in the disk, and one at $\epsilon \simeq 0$ denoting the constituents of a spheroidal component. A typical galaxy would have a disk and a spheroid comprising the bulge, as well as a more extended stellar halo component.

Using the information about the direction of the total angular momentum of all particles

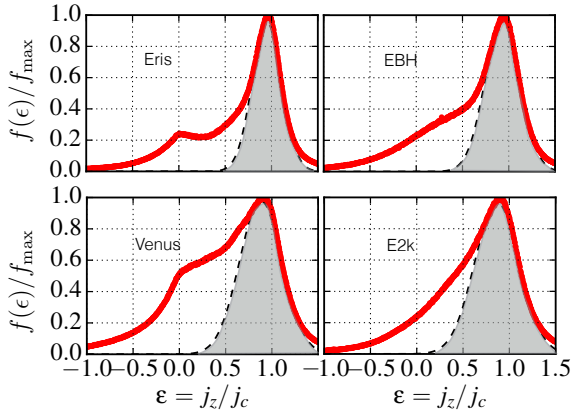

Figure 3.1: The distribution of the circularity parameter ϵ for stellar particles in a galaxy at the most recent redshift (Eris, EBH, and Venus: $z_{\rm end} = 0$; E2k: $z_{\rm end} = 0.3$) is shown with the red line. The black dashed line denotes the Gaussian function obtained as a fit to the distribution right of and about the highest peak in the distribution ($\epsilon \simeq 1$). All particles in the grey-shaded area are assigned to the disk.

in our sample, we rotate the galaxies to appear face-on in the x–y plane. Then we compute the circularity parameters ϵ of all particles and plot their mass-weighted histogram, which is then normalized to the maximum value of the distribution, $f_{\rm max}$, as shown in Figure 3.1 (note that $f_{\rm max}$ represents the most probable value of the circularity).

The total distribution (red line) is the sum of the particles residing in the disk, bulge, and a stellar halo. In what follows, we do not discriminate between the latter two and choose to classify them together as a *spheroid*. Moreover, we defer the complex discussion of bulge classification, in particular whether or not it is a pseudobulge or a classical bulge, to Appendix 3.8, but note here that, in conclusion, our sample comprises composite, classical, pseudobulges, and peanut bulges (in Eris, Venus, E2k, EBH, respectively). Some of the galaxies in our sample exhibit non-axisymmetries such as a clear bar (see the discussions in Bonoli et al., 2016; Guedes et al., 2013), therefore a standard picture of a Sérsic (1963, 1968) bulge and a thin disk (or, equivalently, a sum of two Gaussian distributions of particles peaking at $\epsilon_{\rm s} = 0$ and $\epsilon_{\rm d} = 1$) is not applicable. However, as seen in Figure 3.1, all spiral galaxies in our sample have a distinct, close-to-Gaussian distribution for $\epsilon \gtrsim 0.7$. We thus fit a Gaussian function to each of these distributions for all particles with $\epsilon > 0.8$ at $z_{\rm end}$ to determine the mass and the angular momentum of the disk component, treating the rest as the spheroid. The fits are shown with black dashed lines in Figure 3.1.

To determine the spheroid-to-disk (S/D) and spheroid-to-total (S/T) ratios, we first denote the Gaussian fit to the disk as $g(\epsilon)$ and define the weighting function $w \equiv [f(\epsilon) - g(\epsilon)]/f(\epsilon)$, which describes the fraction of stellar particles in each bin of a histogram that belong to the spheroid. The S/D ratios can be determined from

$$D = \int_{\epsilon_{min}}^{\epsilon_{max}} [1 - w(\epsilon)] M(\epsilon) d\epsilon, \tag{3.1}$$

$$S = \int_{\epsilon_{min}}^{\epsilon_{max}} w(\epsilon) M(\epsilon) d\epsilon, \tag{3.2}$$

where $\epsilon_{min} = -1.5$ and $\epsilon_{max} = 1.5$. The final values of ratios (S/D and S/T, where $S + D = T$) for the $z = z_{\rm end}$ galaxies determined with this method are $S/D = (0.75, 0.51, 0.96, 0.69)$ and $S/T = (0.43, 0.34, 0.49, 0.41)$ for Eris, E2k, Venus, and EBH, respectively.

Although our primary method of decomposition in this paper is kinematic, we also decompose galaxies into spheroids and disks photometrically for the galaxies observed face-on (i.e., parallel to the galactic angular momentum vector). Comparing the results of these two methods may prove useful for determining the uncertainties on the properties derived from the 2D quantities (surface brightness/surface density) vs. those based on the 3D kinematic information.

The mock data, i.e. the surface density profiles for the stars, are calculated for a sphere of $r = 15$ comoving kpc around the centers of galaxies. The fitting function is a combination of the surface density of an exponential disk, $\Sigma_{\rm d}$, and a Sérsic spheroid, $\Sigma_{\rm b}$:

$$\begin{aligned} \Sigma_*(r) = \Sigma_{\rm d}(r) + \Sigma_{\rm b}(r) = \Sigma_{\rm d,0} \exp\left(-\frac{r}{R_{\rm d}}\right) + \\ \Sigma_{\rm b,0} \exp\left[-b_{\rm n}\left(\frac{r}{R_{\rm b}}\right)^{1/n} - 1\right], \end{aligned} \tag{3.3}$$

where n is the Sérsic index, $R_{\rm d}$ and $R_{\rm b}$ are the scale radii of the two profiles, $\Sigma_{\rm d,0}$ and $\Sigma_{\rm b,0}$ are the surface densities at $r = 0$, and $b_{\rm n} = 1.9992\,n - 0.3271$ (Capaccioli, 1989). Initially, we determine parameters with a least-squares method, whose best-fit parameters serve as initial guesses to the more sophisticated Metropolis-Hastings Markov chain Monte Carlo method (Metropolis et al., 1953; Hastings, 1970) with 10^6 realizations. We note that we included a modification to this algorithm, namely we accept only those sets of parameters that result

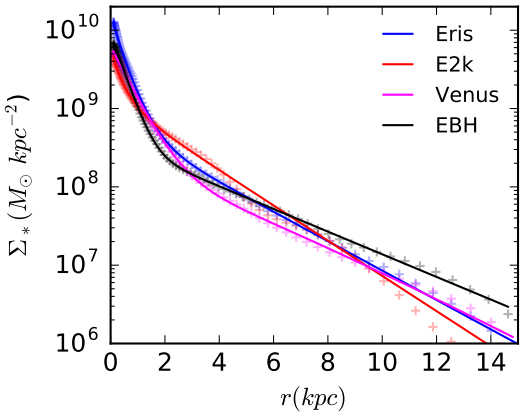

Figure 3.2: Best-fit functions to the surface-density profiles of our sample of simulated galaxies. The actual surface-density profiles are denoted with crosses, whereas the solid lines show the result of the fitting functions (see Equation 3.3). The calculations are performed at $z = z_{\rm end}$.

in the best fit to our data.

The results are shown in Figure 3.2, with the best-fit parameters and estimates of bulge-to-disk ratios set in Table 4.1. We computed the bulge-to-disk (B/D) and bulge-to-total (B/T, with $B + D = T$) ratios according to $B = \int_0^\infty \Sigma_{\rm b}(r) 2\pi r dr$ and $D = \int_0^\infty \Sigma_{\rm d}(r) 2\pi r dr$. When compared to the kinematic estimates, shown again in Table 4.1, these ratios are in near-perfect agreement for Eris and Venus, compatible for EBH, and off in E2k. Nevertheless, the relative values of B/T and S/T ratios are consistent between these two methods, i.e. the sequence of runs with increasingly prominent bulge (spheroid) is in both cases: E2k, EBH, Eris, and Venus. Quantitatively, the differences between the two methods are in the 10–30% range for all galaxies except E2k, for which the difference is about a factor of 3. The differences arising in the bulge-to-disk ratios between the photometric and kinematic decomposition methods are strongest for the galaxies with the most prominent bars, which illustrates how the accuracy of the photometric method is dependent on the type of spheroid. The kinematic method enables to distinguish between the material of high and low velocity dispersion, while the Sérsic index measures only the curvature of the surface density profile, and does not necessarily describe an object that is truly round or flat in 3D. We note that galaxies which harbor bars might turn out to be morphologically closer to pure disk objects (E2k), *Sc*/*Sd* galaxies (EBH), or *Sb*/*Sc* galaxies (Eris), as we do not separate bars in this paper.

The more pronounced difference in the case of E2k, in which the photometrically estimated bulge is much less prominent than that estimated using kinematics, highlights a peculiarity of the galaxy with stronger feedback. By low redshift, this galaxy has acquired a stellar component with no clear separation between disk and spheroid (see Figure 3.1). However, when the surface brightness profile is inspected, it is almost a single exponential up to less than 1 kpc from the very center, which is typical of very late-type disks, such as Sd galaxies. The central steepening of the profile inside 1 kpc is highly correlated with the growth of a bar around $z = 1$ and below, as we checked that the inner profile is flatter earlier on. We argue that E2k is essentially a nearly bulge-less, barred disk galaxy, or equivalently that the bar makes up for a large fraction of what we identify as the bulge with the photometric method (see Appendix 3.8). The tendency of stronger SN feedback to suppress bulge formation (e.g. Hopkins et al., 2014; Keller et al., 2014) is expected since ejective feedback removes low-angular momentum baryons by means of outflows (see Governato et al., 2010; Brooks et al., 2013). The tendency of this galaxy to have a kinematically hotter stellar component is also likely an effect of feedback on the galactic structure, which will be studied in Paper II, but may also reflect the presence of a rather prominent bar which is expected to induce non-circular motions in the stellar component.

We note that, in observations, the quoted B/T ratios are normally obtained by applying the fits and decomposition to the surface brightness profile in a given magnitude band, rather than to the surface density. Depending on the band, the difference in the relative weight of the bulge and the disk can be small or quite large, with variations of up to a factor of 3 between the B and the I band, depending on the age of the stars of the various components (Graham & Worley, 2008). In general, the bulge, which is composed of an older stellar population than that of the disk, will be fainter in optical bands relative to the disk, irrespective of the underlying mass ratio of the components. Hence our estimates of the relative contribution of the two components, which are based on actual mass density, should be considered as an upper limit. Indeed in the case of Eris, the B/D ratio we quote here is higher by a factor of 2 with respect to the I-band B/D found with GALFIT (Peng et al., 2002, 2010) after post-processing with the SUNRISE radiative-transfer code (Jonsson, 2006; Jonsson et al., 2010), including dust reddening (Guedes et al., 2011). This supports the notion that, photometrically, E2k is an almost bulge-less galaxy as its B/D would be < 0.1 in optical bands.

	Eris	E2k	Venus	EBH
$\Sigma_{\rm d,0}$	6.43×10^8	1.29×10^9	6.12×10^9	3.85×10^8
$R_{\rm d}$	2.31	1.93	0.62	2.44
$\Sigma_{\rm b,0}$	2.43×10^9	5.67×10^8	4.97×10^7	1.80×10^9
$R_{\rm b}$	0.70	0.70	4.84	0.67
n	1.14	1.35	0.85	0.88
B/T	0.41	0.11	0.47	0.29
S/T	0.43	0.34	0.49	0.41
B/D	0.70	0.13	0.89	0.41
S/D	0.75	0.51	0.96	0.69
$j_{\rm d}$	784.6	762.6	618.4	952.0
$j_{\rm b}$	143.0	133.0	101.2	139.3
$j_{\rm star}$	511.0	547.4	363.3	613.2
$j_{\rm gas}$	1620.2	916.4	1541.4	1829.6

Table 3.2: Best-fit values of the parameters of the photometric decomposition (see Equation 3.3). For a comparison, we also show the results of the kinematic decomposition (B/T vs. S/T and B/D vs. S/D). We add the values of the specific angular momenta calculated at $z_{\rm end}$ for: $j_{\rm d}$ – stars in the disk; $j_{\rm b}$ – stars in the bulge; $j_{\rm star}$ – stars in the disk and bulge; $j_{\rm gas}$ – cold ($T < 10^4$ K) gas in the galaxy. The units of Σ, R, and j are $\rm M_\odot$ $\rm kpc^{-2}$, kpc, and $\rm km\ s^{-1}$ kpc, respectively.

3.5 j_*–M_* diagrams

In this section, we use the outcome of the preceding analysis to determine the specific angular momentum of the disk and bulge, as well as that of the overall stellar and gas components. In this way, we can compare the scaling relation between stellar mass and specific angular momentum with those of observed galaxies, as well as study the evolution of such relations from high to low redshifts. This is particularly relevant for the interpretation of the j_*–M_* diagram which has been proposed as an alternative to the Hubble sequence (Romanowsky & Fall, 2012).

We calculate the specific angular momentum of our sample of galaxies at $z = z_{\rm end}$ for the entire galaxies and for their separate components. The specific angular momentum vector of particle species k is defined as

$$\mathbf{j}_k = \frac{\sum_i m_{k,i} \mathbf{r}_{k,i} \times \mathbf{v}_{k,i}}{\sum_i m_{k,i}}, \tag{3.4}$$

where the sums are over each particle i. The particles within each histogram bin (Figure 3.1)

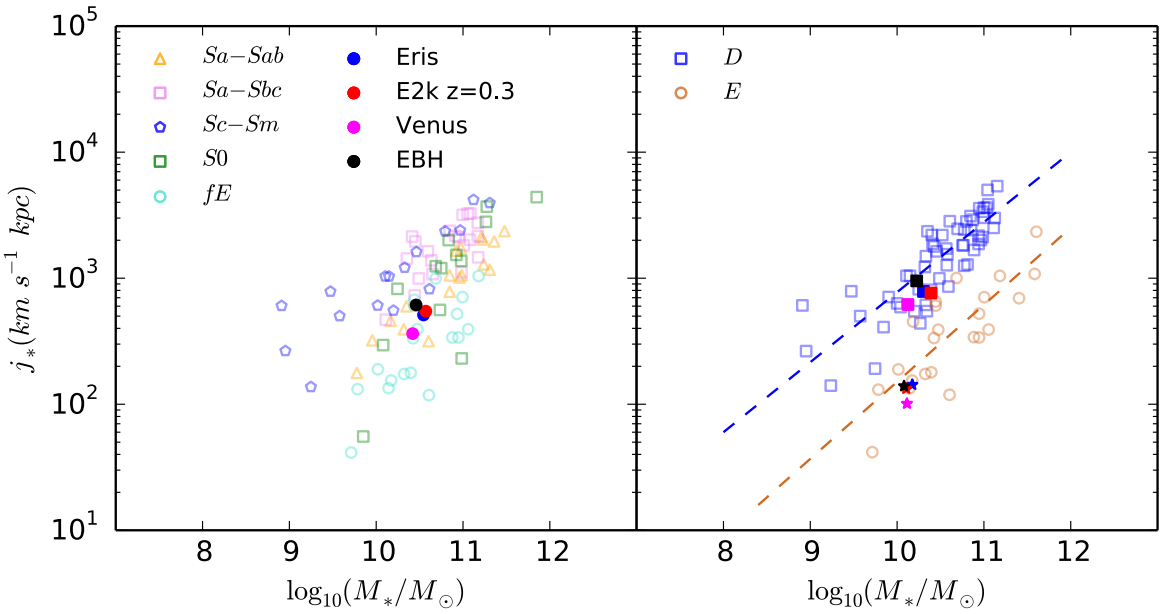

Figure 3.3: Specific angular momentum–mass (j_*–M_*) diagrams for stars of the simulated galaxies vs. the sample of Fall & Romanowsky (2013). Left. The comparison of the total specific angular momentum of the simulated galaxies with the observed galaxies of various morphological types. Right. Simulated galaxies are kinematically decomposed into disks (squares) and spheroid (stars) and then compared with the subsample of observed pure disk galaxies (D) and ellipticals (E).

are assigned to a spheroid or a disk randomly but in numbers determined by the weight function w defined in Section 3.4.

Our results are set against two samples of observed galaxies. In the left panel of Figure 3.3, we compare the total specific angular momentum of the stars in our galaxies with a sample of galaxies classified by Fall & Romanowsky (2013) according to their morphologies. The location of our simulated galaxies on that diagram is well-aligned with the population of observed disk-dominated galaxies. Furthermore, in the right panel, we compare the individual components, i.e. spheroids (marked as stars) and disks (marked as squares), with the sample of pure disk galaxies and ellipticals of Fall & Romanowsky (2013). Upon the decomposition, it is evident that all simulated galaxies consist of a disk component with high specific angular momentum and a spheroidal component with low specific angular momentum. Moreover, in that respect, the disks of the simulated galaxies are in perfect agreement with what is expected of bulgeless galaxies, and their spheroids also agree well with what is found for ellipticals. The ratio of specific angular momentum between the corresponding

components ranges from 5.5 to 6.8 (see also Table 4.1).

As pointed out by Kormendy & Kennicutt (2004), morphologically bulges are regarded as ellipticals "living in the middle of a disk". In practice, this interpretation might change if a bulge was formed by secular processes (so-called pseudobulge, discussed more in Appendix 3.8). Nevertheless, both the total j_*–M_* diagrams, as well as the dichotomy in the distribution of the specific angular momentum of the components, confirm that the simulated galaxies do not suffer from the overcooling problem or the angular momentum catastrophe (see Section 3.2), and can be regarded as good laboratories for in-depth studies of the angular momentum evolution.

In what follows, we investigate the evolutionary tracks of the galaxies and their components on the j_*–M_* diagram, and also address their dependence on the S/T ratio. To do so, first we need to decompose our sample of galaxies at various redshifts. In particular, at high redshift, this is a non-trivial task, given the complexity of the structure of those galaxies, tidal interactions, and frequent mergers. We thus study kinematic diagrams along with the morphology of both gas and stars in order to properly interpret the data. Our results are presented in Figure 3.4.

In general, upon combining the circularity diagrams with the morphological data-set, in most of the cases the S/T decomposition is straightforward. The same procedure as in the case of the $z = z_{\rm end}$ galaxies is applied, i.e. based on finding the thin disk in a sphere of 15 comoving kpc encompassing the galaxy. Whenever the fitting of a Gaussian fails (e.g. for both Venus and E2k at $z = 3$), we identify the peak of the circularity distribution that should correspond to the disk, i.e. near $\epsilon = 1$, and then characterize the disk as the ensemble of stars distributed symmetrically around the circularity peak (see for example view *a* for E2k at $z = 3$ in Figure 3.4).

All galaxies exhibit a similar morphology at $z = 5$, i.e. they appear to be ellipsoids rather than flat extended disks, although in the inner 1–2 kpc a flat disk-like component is already discernible. This and the fact that their distribution of the circularity parameter peaks close to 0, lead to the classification of these galaxies at that stage as spheroid-dominated. The disky component is approximated by mirroring the distribution around $\epsilon_{\rm d} = 1$ as explained above, but with the peculiarity that at this stage there is no peak at high circularity yet.

We caution that the galaxy structure at this redshift might suffer from resolution limitations, as the disk scale length would correspond to only a few gravitational softenings

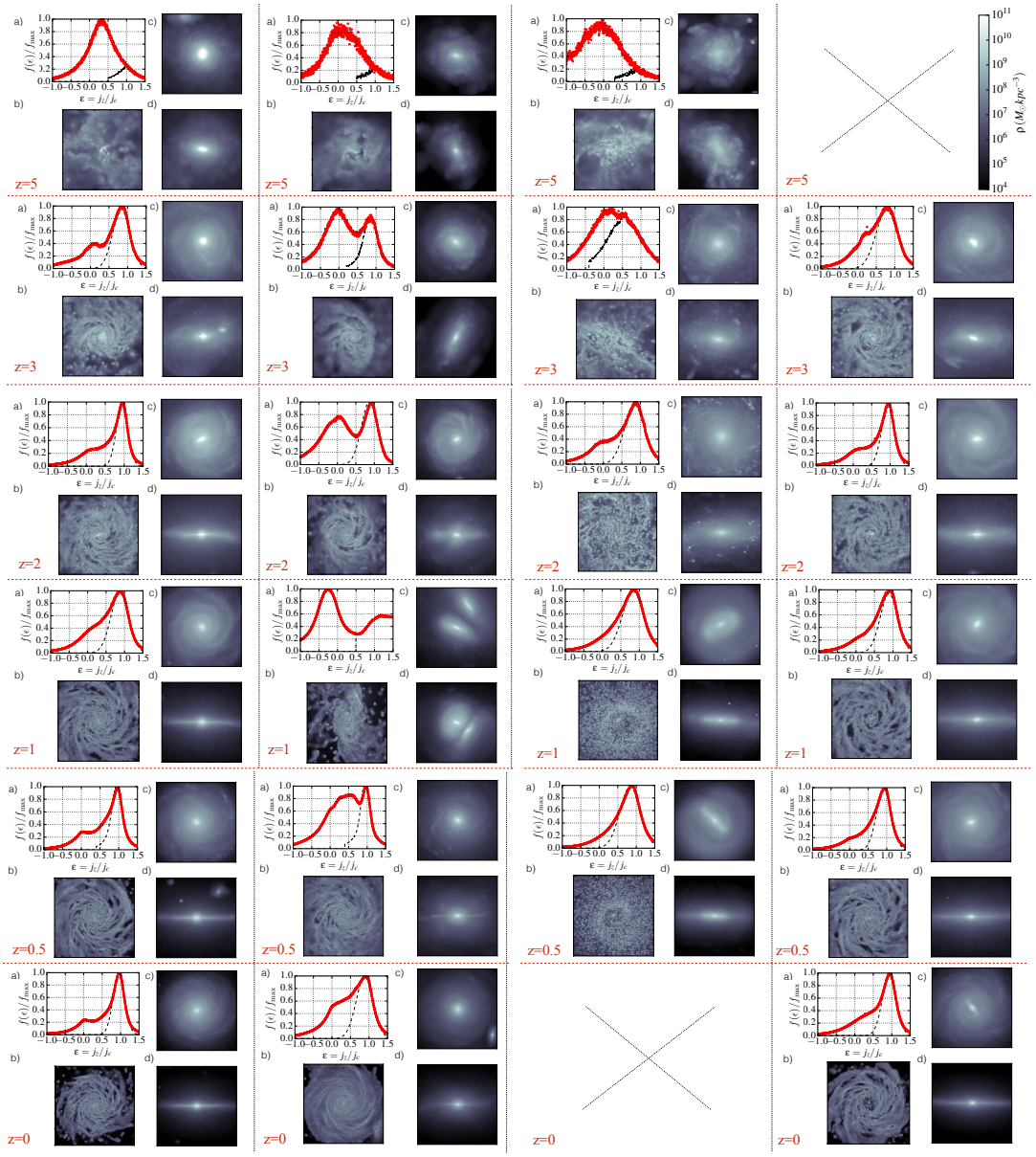

Figure 3.4: A diagram linking the morphology of a galaxy at various stages of its lifetime with its kinematics. Each column corresponds to a different run – going from left to right: Eris, Venus, E2k, and EBH. Every row shares the same redshift. Crosses are placed whenever an output of a run is missing. Each piece of a matrix contains the following information: a) distribution of the circularity parameter in a galaxy; b) gas density map of a galaxy oriented face-on; c) stellar density map of a galaxy oriented face-on; d) stellar density map of a galaxy oriented edge-on. Total circularity distributions are colored in red, whereas their sub-distributions assigned to the disks are marked in black. Every image has a width of 30 comoving kpc.

at this epoch (disk sizes are expected to be about an order of magnitude smaller simply from the scaling of the halo virial radius with redshift in a Λ–CDM cosmology, see e.g. Mo et al. 1998). Indeed, recent simulations with much higher resolution (tens of pc) that stop at $z > 5$ do find a prominent rotating disk in halos of masses only a few times larger than ours already at $z = 8$ (Fiacconi et al., 2016; Pallottini et al., 2016). However, these simulations also find that the disk is thick and turbulent, resulting in $v/\sigma < 2$ for the most part (where v stands for the magnitude of the velocity vector and σ is the total velocity dispersion), which supports the notion that the galaxy would be classified as spheroid-dominated based on our criteria. An early phase in which a turbulent gas disk results in a thick primitive stellar disk was already pointed out in Bird et al. (2013).

In Figure 3.4, the circularity diagrams of Eris and EBH have a dominant rotating disk around $\epsilon \simeq 0.8$, and a secondary peak near $\epsilon = 0$–0.1 at $z = 3$. A gaseous disk is evident and the edge-on view of stars appears flattened, although we witness signs of tidal disturbances from frequent interactions. This suggests that the galactic structure is continuously evolving at this epoch and hard to characterize in a simple way. Most of the mass of Venus and E2k has a low circularity parameter peaking at about $\epsilon_s = 0$, whereas the secondary peak is lower. The gaseous disk of Venus is rotating coherently, whereas the cold gaseous component in E2k appears to not have an ordered rotation pattern, probably reflecting the stronger effect of feedback on gas dynamics.

By $z = 2$, all galaxies are already dominated by a thick disk. The face-on stellar density maps reveal spiral structures present in all of them. By this time, Eris, E2k, and EBH have already entered a quiescent phase past the last major merger. Venus, on the other hand, experiences another major merger at $z \sim 1$. In this case, as there are two interacting galaxies at very small separation, the decomposition of the system is somewhat arbitrary. The circularity diagrams show two clear peaks, one at about $\epsilon_d = 1$ and the other at $\epsilon_s \simeq -0.2$, thus we choose to cut the distribution at the minimum between the two peaks, i.e. at around $\epsilon = 0.5$. Despite the ongoing stellar merger (views *c*–*d*), the gaseous disk appears flat (*b*). The spiral structure of E2k vanished giving way to a prominent bar. The circularity distribution, although strongly asymmetrical, shows only one peak near $\epsilon_d = 0.8$.

From $z = 0.5$ to 0, the galaxies generally appear similar. The triple-component distribution of Venus settles into a double-component one by $z = 0$ with an extended thin disk (in both the gaseous and stellar matter) and a massive stellar bulge. EBH develops a bar which

appears more prominent than the one in E2k in terms of size relative to the disk itself.

With a clear picture of morphological fluctuations in our sample of galaxies, we can proceed to quantify the magnitude of the specific angular momentum vector at various time steps. Figure 3.5 shows evolutionary tracks for the cold gas mass ($T < 10^4$ K, dash-dot line), total stellar mass (solid line), stellar mass in the spheroid (dotted line), stellar mass in the disk (dashed black line), and joint total stellar and total cold gas mass (squares) at nine redshifts – $z = (5, 4, 3, 2, 1.5, 1, 0.7, 0.5, 0)$ – for our four runs (for EBH and E2k, respectively, the $z = 5$ and $z = 0$ data-points are missing). The data-points are color-coded with the S/T ratios. The two diagonal dashed lines represent the relationship from Fall & Romanowsky (2013) of $j_* \propto M_*^{\alpha}$ with $\alpha \sim 2/3$ for disk galaxies (in blue) and ellipticals (in red).

The specific angular momentum of cold gas is substantially higher than that of the stellar component (it reaches values of order 10^3 km s^{-1} kpc), which is consistent with observations (Obreschkow & Glazebrook, 2014). At all times, disks have a higher specific angular momentum than spheroids. At high redshift, all stars have a very low specific angular momentum that evolves below the line of ellipticals. After $z = 3$, they move over that line and gradually get closer to the line of disks. Eris and EBH evolve on a slope which is steeper than $\alpha = 2/3$, namely $\alpha = 1.4$. E2k, however, evolves on a track parallel to the one found by Fall & Romanowsky (2013). Venus is a more complex case: it initially evolves approximately on the track of the ellipticals and, after several fluctuations, its track steepens in the final stages, after the last major merger ($z < 0.7$).

In general, Eris, EBH, and E2k become disk-dominated galaxies past $z = 4$. Venus experiences a series of oscillations in the S/T ratio through frequent mergers.

3.6 The galaxy–halo connection

As discussed in Section 3.2, theory and observations suggest that the specific angular momenta of galaxies are similar to those of their dark halos, which is often referred to as the "weak conservation" of angular momentum. Strictly speaking, specific angular momentum of galaxies is not conserved, as its vector is not time-independent. Galaxies and their halos grow in mass through accretion and mergers, and experience feedback-related phenomena which modify their specific angular momentum. We show signatures of such mechanisms in Figure 3.6, where we combine the information about the changes in the magnitude of the

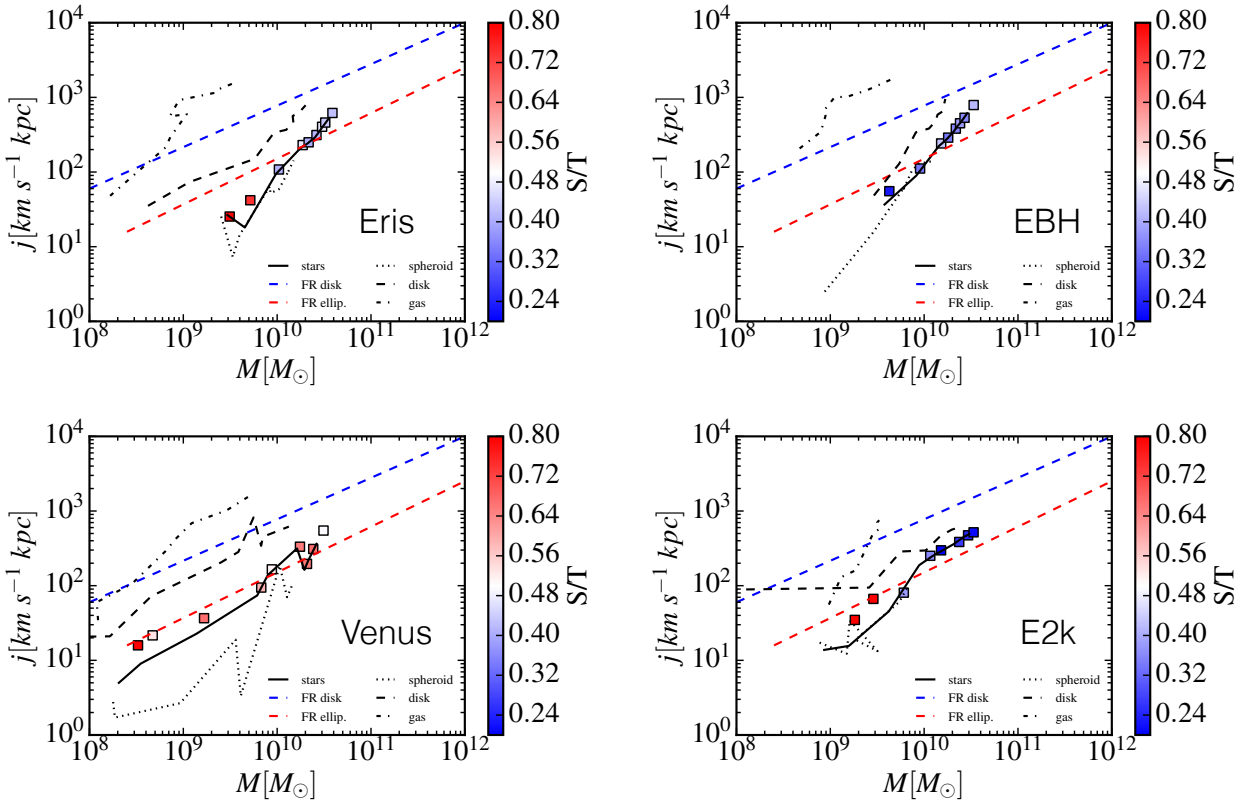

Figure 3.5: Specific angular momentum evolution of various components on the j–M diagram. The gas considered here is cold (i.e. $T < 10^4$ K). "FR disk" and "FR ellip." denote best-fit tracks for disk galaxies and ellipticals of Fall & Romanowsky (2013). Each data-point corresponds to the following redshifts (left to right): $z = (5, 4, 3, 2, 1.5, 1, 0.7, 0.5, 0)$ and represents the joint specific angular momentum of cold gas and stars (for EBH and E2k, respectively, the $z = 5$ and $z = 0$ data-points are missing). The color-coding ascribed to the data-points reflects the S/T ratios of the galaxies at a given redshift.

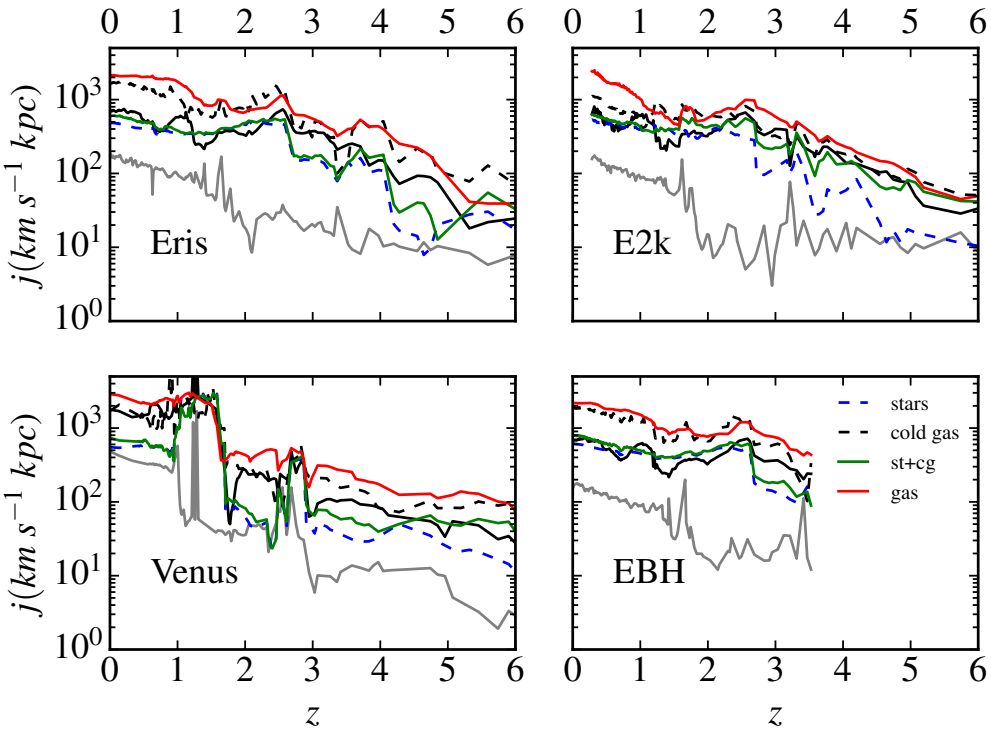

Figure 3.6: Evolution of the specific angular momentum of the different components of our four galaxies: stars, cold gas ($T < 10^4$ K), all gas, and stars with cold gas within the virial radius as a function of redshift. The solid, black and grey lines represent the specific angular momentum for the dark matter within the virial radius and 10% of the virial radius, respectively. Available data for EBH and E2k exist only for $z < 4$ and $z > 0.3$, respectively.

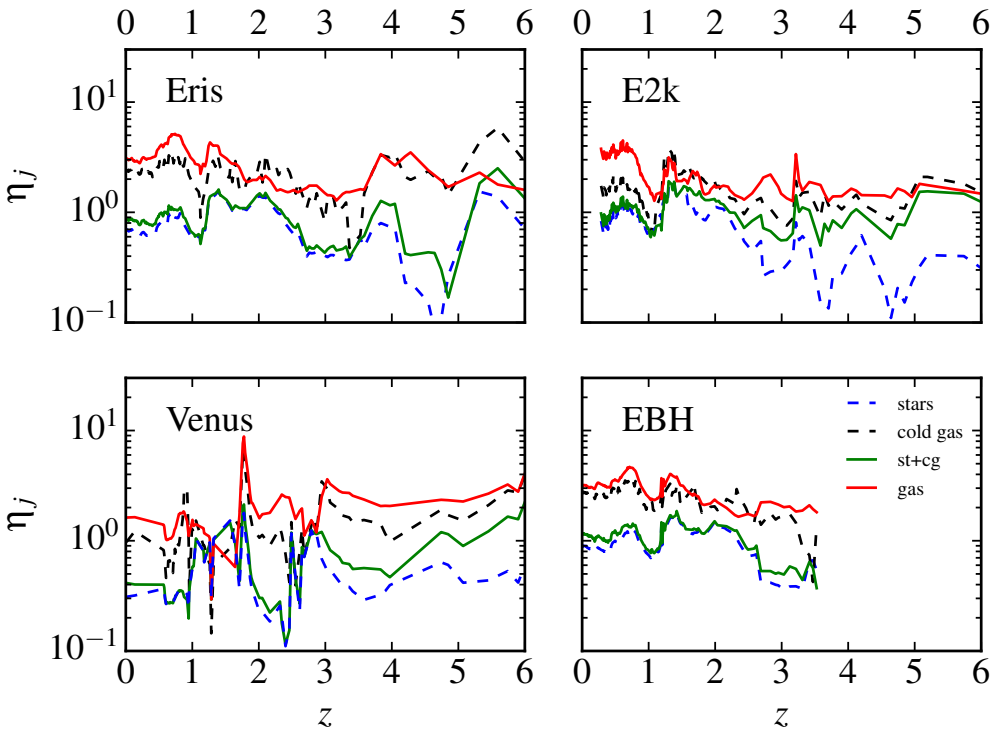

Figure 3.7: Evolution of the retention factor of the different components of our four galaxies: stars, cold gas ($T < 10^4$ K), all gas, and stars with cold gas within the virial radius at a given redshift. Available data for EBH and E2k exist only for $z < 4$ and $z > 0.3$, respectively.

specific angular momentum vectors of various components with time (redshift). To those components count stars (blue dashed line), cold gas ($T < 10^4$ K, black dashed line), total gas (red solid line), stars and cold gas (green solid line), and dark matter (black solid line). The angular momentum per unit mass is calculated within the virial radius of the halo at a corresponding z. Although on average the specific angular momentum of every component increases with time, noticeable fluctuations are present at nearly all redshifts. Those temporary gains and losses of the angular momentum per unit mass are stronger before $z = 1$ in all the runs, regardless of the initial conditions. It has been already shown that the angular momentum can be both lost, e.g. due to torques associated with violent disk instabilities (Danovich et al., 2015), or significantly increased in galactic fountains if material is ejected for long times and to large radii (Übler et al., 2014). We note that Paper II will focus on investigating these and other causes in greater detail.

Zavala et al. (2016) report a better agreement between the specific angular momentum of the luminous matter and the dark matter within 10% of the virial radius, rather than the full $R_{\rm vir}$, in their large-volume simulations. We investigate this possibility and show the specific angular momentum for the dark matter within $0.1R_{\rm vir}$ with a solid grey line in Figure 3.6. On average, the specific angular momentum of stars evolves closer to that of dark matter within the virial radius, rather than only in the central part of the halo. This holds in all runs, except for Venus in two periods of time: between $z = 2.5$–2 and $z = 1$–0. Those two transitions follow sharp changes (reaching an order of magnitude) in the specific angular momentum of all components and are likely associated with major mergers. At those times, the S/T ratios fluctuate (see Figure 3.5).

Low-resolution, large-volume simulations seem to have converged on the high value of the specific angular momentum 'efficiency' or 'retention' factor $\eta_{\rm j} \equiv j/j_{\rm DM} \sim 1$ (Genel et al., 2015; Pedrosa & Tissera, 2015; Teklu et al., 2015). However, the sample of Zavala et al. (2016), although generally consistent, appears to be a factor of a few offset from the observed track of pure disks, favoring a lower retention factor. Perhaps this explains their agreement with the specific angular momentum of the dark matter in a central subregion rather than in the whole halo.

As pointed out in Section 3.5, different initial conditions (active vs. quiet) translate into different locations of the evolutionary tracks of galaxies in Figure 3.5. As a result, Venus evolves closer to the track of ellipticals than the other runs. Since the sequence of

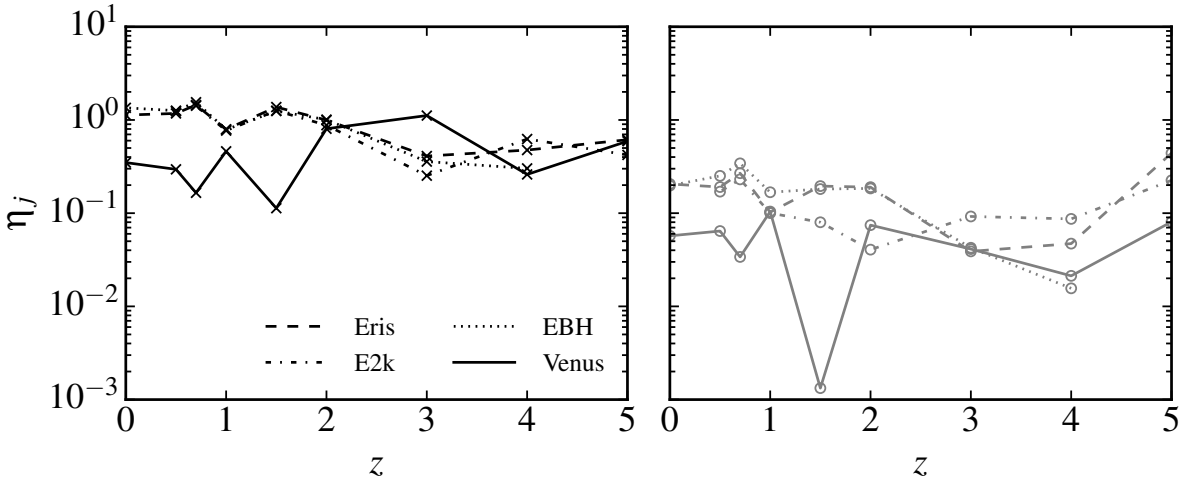

Figure 3.8: Stellar retention factor for disks (left panel) and spheroids (right panel) calculated at a few redshifts, following the kinematic decomposition covered in Section 3.5. Values for different components are marked with distinctive symbols: disks with crosses and spheroids with open circles for spheroids). The lines denote the interpolations between these data points.

ellipticals is offset from that of disks by a factor of ∼5, the retention factor for ellipticals is expected to be lower at the same stellar or halo mass (Fall & Romanowsky, 2013). In fact, one can verify that at the constant M_*/M_h, a hypothetical galaxy with the same specific angular momentum as Venus at $z = 0$ has $j = j_\mathrm{Ven} = 0.23 j_\mathrm{pd}$, where j_pd is the specific angular momentum of pure disks at $M_* = M_{*,\mathrm{Ven}}$. The corresponding retention factor is $\eta = j/j_\mathrm{DM} = 0.23\eta_\mathrm{pd} \simeq 0.2$, assuming $\eta_\mathrm{pd} \simeq 80\%$ (Fall & Romanowsky, 2013), consistent with expectations.

The time-dependence of the retention factor η_j for the baryonic and dark matter within the virial radius of a galaxy is shown in Figure 3.7. The color-coding is consistent with the previous figure. For our sample of simulated galaxies, the stellar retention factor is $\eta_\mathrm{j} \simeq (0.7, 0.8, 0.3, 0.9)$ at z_end for Eris, E2k, Venus, and EBH, respectively. Total gas and cold gas are endowed with a specific angular momentum that is 2–6 times higher than that of dark matter (the peak of Venus attains $\eta_\mathrm{j} = 10$ in a major merger). Generally, the retention factor of the stellar component is confined within 0.1–2 in all cases but most of the time below $z = 3$ it does not exceed 1.5 or fall below 0.5 in the runs with a quiet merger history. The stellar retention factor in all runs is remarkably constant below $z = 1$, which agrees with the theoretical prediction of j_dm evolving as $M^{2/3}$ similarly to baryons. Interestingly,

despite the relatively violent merger history, the retention factor of stars in Venus at $z = 0$ is almost the same as originally (here $z = 6$).

Given the high resolution of our simulations, we can use the results of the last two sections – careful decomposition and the calculation of the specific angular momentum of the stellar components – to characterize the individual stellar retention factors of disks and spheroids at the time steps discussed in Section 3.5. In Figure 3.8, we present for the first time the retention factors of disks and bulges (spheroids) down to $z = 5$. The retention factor of galactic disks is remarkably constant, ranging from 0.3–1.5 over more than 12 Gyr of evolution. This means that the evolution of the rotationally supported component is driven by its dark matter halo, and this relationship is particularly tight for systems with a quiet merger history. In particular after $z = 2$, galactic disks grow approximately homologously with their halos, i.e. $j_{\rm dark}/j_{\rm halo} \approx$ constant, unless a system undergoes multiple major mergers. The retention factor of spheroids, although also correlated, attains values an order of magnitude lower. This offset, along with the irregularities, such as those in the run with an active merger history, requires further investigation.

The results presented in this section raise questions about the physical mechanisms that affect galactic angular momentum, as well as the reasons for relatively constant proportionality between $j_{\rm disk}$, $j_{\rm bulge}$, and $j_{\rm h}$. The reason behind this approximate cancellation of gains and losses of the angular momentum per unit mass of galaxies, and in particular of their disks, is the subject of Paper II. In the context of the feedback processes implemented in these simulations, it appears that the strength of SN (blastwave) feedback or the presence of AGN (thermal) feedback has certainly less impact on the retention factor within $R_{\rm vir}$ than the merging history driven by the environment in which a galaxy is born.

3.7 Conclusions

In this paper, we perform an analysis of the angular momentum evolution of galaxies residing in Milky Way-sized halos, studying the relation between morphological appearance and kinematics as well as the evolutionary tracks on the j_*–M_* diagrams. We use high-resolution cosmological zoom-in simulations, an approach that is essentially complementary to the large-volume calculations, as we are able to follow the assembly of each object separately and in greater detail. Our sample of simulations comprises runs with varying processes

(SN and AGN feedback, as well as different radiative-cooling recipes), different strength of feedback, and different assembly histories for galaxies in halos of identical masses by $z = 0$.

Owing to the high resolution obtained in our simulations, we can also study the specific angular momentum evolution of the stellar components – the disks and spheroids – as the characteristic size of these components is an order of magnitude above the gravitational softening adopted. Additionally, a core part of this paper is devoted to studying the specific angular momentum of gas and dark matter. In what follows, we summarize the main findings of this work and motivate the necessity of a follow-up study.

1. The kinematic decomposition at $z = z_{\rm end}$ ($z_{\rm end} = 0$ for Eris, EBH, and Venus; $z_{\rm end} = 0.3$ for E2k), based on the circularity diagrams as a measure of the kinematics in the plane of the galaxy, and the photometric method yield results that are in perfect agreement for Eris and Venus, slightly deviated in the case of EBH and off by a factor of 3 in E2k (see Section 3.4).

2. Our simulated galaxies represent a variety of morphological types and lie on the j_*–M_* diagrams with the population of spiral galaxies (Figure 3.3). When decomposed into disks and spheroids, the dichotomy in the specific angular momentum of disks and bulges is reproduced. The disks and bulges of our individual galaxies are separated by a factor 5.5–6.8, in agreement with the findings of Romanowsky & Fall (2012). Our galaxies do not suffer from the angular momentum problem and are good laboratories for the in-depth studies of the angular momentum evolution.

3. We present time-dependent diagrams (Figure 3.4) that reveal correlations between the morphological appearance and the stellar kinematics of simulated galaxies, indicating that the latter can be predicted to some extent from the former.

4. On average, galaxies evolve on straight lines past major mergers on the $\log j_*$–$\log M_*$ diagram (Figure 3.5). Eris and EBH evolve on a slope which is steeper than $\alpha = 2/3$, and we find $\alpha = 1.4$. This is likely due to the fact that they undergo a series of morphological changes, which in turn modify their S/T ratios. E2k, which exhibits the least variations in this respect, evolves on the slope close to $\alpha = 2/3$. We argue that galaxies with relatively stable morphologies and secular processes occurring on long timescales move on the $\log j_*$–$\log M_*$ diagrams along these parallel lines. Shorter timescale processes could perturb these tracks: frequent mergers may bring these galaxies closer

to the tracks of ellipticals, as in the case of Venus. Although our sample of galaxies is too small to test these scaling relations at a fixed redshift, the time-dependent j_*–M_* sequence of a single galaxy with a constant B/T ratio provides an indirect test of this relationship. Recent results of Burkert et al. (2016) and Contini et al. (2016) for disk-dominated galaxies at higher redshifts ($0.2 < z < 3$) lend support to this conjecture.

5. The specific angular momentum of baryons within $R_{\rm vir}$ tracks that of the halo (Figure 3.7). The value for the total gas and cold gas is 2–6 times higher than that for the dark matter. The stellar retention factor is nearly constant below $z = 1$ and reaches $(0.7, 0.8, 0.3, 0.9)$ at $z_{\rm end}$ in Eris, E2k, Venus, and EBH, respectively.

6. In general, the specific angular momentum of stars is more consistent with that of the dark matter within the virial radius rather than within its fraction (10%, Figure 3.6). When a galaxy is disrupted by many major mergers (e.g. Venus), the overall specific angular momentum of stars is lowered, bringing the latter closer to the angular momentum content of a central subregion smaller than the virial region.

7. Galactic disks have nearly constant retention factors of order unity, which implies their specific angular momentum is strongly correlated with that of the dark halo at all times. Exceptions are the phases in which major mergers occur, which is more relevant for Venus than for the other galaxies having quiet merging histories. The retention factor of spheroids, although correlated, is an order of magnitude lower for all galaxies, suggesting that the spheroid is more sensitive to mechanisms acting to decouple the dynamical evolution of baryons from that of the dark halo. The investigation of the latter mechanisms will be a focus of a follow-up paper, yet it is interesting that the spheroid could turn out to be a more sensitive probe of the physics of galaxy formation than the disk.

8. We find that the j_*–M_* diagrams at $z_{\rm end}$, as well as the retention factors of the entire galaxies and their components, appear to be more sensitive to the merger history than the difference in the sub-grid physics, in the context of the feedback recipes implemented in our simulations. However, the evolutionary tracks on the j_*–M_* sequence, and in particular of the disks and spheroids separately, exhibit noticeable differences

certainly related to the differences in the sub-grid models.

The good agreement with recent observations for angular momenta of low-redshift galaxies (Fall & Romanowsky, 2013), and the confirmation of a close connection of the specific angular momentum of dark matter and baryons, in particular of the disks, set the groundwork for an in-depth study of physical processes driving the evolution of the angular momentum of baryons in these galaxies. This will be presented in a follow-up paper (Paper II). Paper II will also investigate the role of feedback processes and disk instabilities in the angular momentum transport in these galaxies, as well as how the angular momentum of accreted gas evolves up to the point it joins the disk, shedding more light on the relation between the angular momentum of galaxies and that of their host halos.

3.8 Nature of spheroids

As mentioned in Section 3.4, our sample of galaxies might contain classical bulges (C), pseudobulges (P), "peanut" bulges (box), or so-called composite bulges (COMP, e.g. Kormendy & Barentine, 2010). Here, we use six tests commonly used in literature (summarized in Table 4.3) in order to classify the "bulges" or "spheroids" in our simulations, as well as qualify how sensitive the key results of this paper are to this categorization. These criteria are: visual morphology, presence of a bar, Sérsic index, size–mass relation, star formation rate and vertical distribution (for more details, see e.g. Gadotti & dos Anjos, 2001; Kormendy & Kennicutt, 2004; Gadotti, 2009).

Based on pure visual appearance when seen edge-on (see the last row in Figure 3.4), the bulges of Venus and Eris could be classified as classical bulges at $z = 0$, whereas those of E2k and EBH appear more flat and disky, hence more similar to pseudobulges.

The fact that EBH and E2k are the only two galaxies that host a strong, large-scale bar at low redshift (Eris has a bar at higher redshift which weakens and shortens at low redshift, becoming essentially a nuclear bar a few gravitational softenings long) reinforces this distinction.

In terms of the Sérsic index, all galaxies have a rather low n of order 0.8–1.4 at $z_{\rm end}$ (see Table 4.1). Given that a relatively low Sérsic index photometrically akin to a disk component ($n < 1.5$) is characteristic of pseudobulges, the values obtained from the photometric decomposition are hardly indicative of classical bulges.

Another criterion utilizing our results of the photometric decomposition is the mass–size relation. In Figure 3.9, we compare the location of our bulges on the mass–size diagram with the sample of Gadotti (2009), who found unique relations for ellipticals, classical bulges, and pseudobulges. Our galaxies lie on that diagram in the sequence of decreasing importance of the bar with increasing mass, which places E2k in the area of the graph populated by pseudobulges, Eris by classical bulges, and EBH at the intersection of the two. We note that Figure 3.9 also places Venus high above the line of ellipticals due to a large radius $R_{\rm b}$, which was already argued in Section 3.4 to be unrealistic and likely represents a failure of the photometric method of decomposition. A brighter stellar envelope of Venus suggests that a more prominent stellar halo or a thick disk component contaminates the decomposition. Indeed, restricting the region to a slice of height 1 kpc above and below the disk plane reduces the bulge scale length to $\sim$3 kpc.

criterion	Eris	Venus	E2k	EBH
morphology	C	C	P	box
bar	P	C	P	P
Sérsic	P	P	P	P
size–mass	C	C	P	C/P
star formation	C/P	C	P	C/P
vertical distribution	C	C	P	C/P
summary	COMP	C	P	box

Table 3.3: Types of bulges in the simulation. The results for each classification scheme are labelled as: P – pseudobulge, C – classical bulge, box – peanut bulge, COMP – composite bulge. The "morphology" criterion is based on the surface density stellar maps.

The fifth criterion, stellar ages, is addressed in Figure 3.10, where we show the mass distribution of stellar ages of bulges (left) and disks (right). A massive population of young stars (younger than 4 Gyr) in the bulge of E2k is characteristic of still star-forming pseudobulges. At another extreme, Venus experiences a sharp decline in this distribution near 2 Gyr at the level clearly indicating quenching of star formation, which would be consistent with what is expected of a classical bulge. Eris, EBH, and Venus are good examples of galaxies with a rather old bulge and a young disk.

The final criterion, the vertical kinematics, allows for determining whether disks and spheroids are kinematically and structurally alike. Hence, in the top and bottom panels of Figure 3.11, we show the distribution of the vertical velocity and vertical position of the

stellar particles, respectively. The components of Eris and EBH have very distinct vertical kinematics, which is an attribute of galaxies with classical bulges. In contrast, E2k exhibits very little distinction, whereas the case of Venus is rather ambiguous, yet closer to the classical picture. In the bottom panel of Figure 3.11, the vertical position distributions of the bulge and disk particles of EBH are nearly identical, whereas the disk of E2k is thicker than the spheroid, both certainly indicative of a pseudobulge. The bulges of Eris and Venus have clearly broader distributions than the disks, hence a significant part of their mass is off-planar.

Although the criteria do not always agree on the classification, overall there is more evidence that the spheroids of E2k and EBH are pseudobulges, whereas the spheroid of Venus is a classical bulge. The bulge of Eris, however, appears to be a composite bulge, i.e. a small, star-forming disk-like bulge inside a classical bulge (see the last row of Table 4.3). Our conclusion categorizing the bulge of Eris as a composite bulge rather than a pseudobulge complements the previous in-depth studies of the bar evolution in that simulation (Guedes et al., 2013).

Interestingly, if we look at the problem from the formation point of view, we can notice an interesting trend in Figure 3.5; namely, the bulge of Venus, that is the one for which a classification as classical bulge is more supported, is the one that evolves more differently from the disk in the 'angular momentum vs. stellar mass' track, whereas that of E2k, which is that for which more diagnostics point to a pseudobulge, is the one that evolves closest to the disk track. Hence, our results for spheroids shown in Figure 5 verify that classical bulges (Venus) have lower angular momentum than pseudobulges or composite bulges (the remainder). Also, while in Venus there is a clearly different evolutionary track between the stars as a whole and the bulge, these tracks are almost coincident in the other three cases. This reinforces the notion that formation is reflected in the final bulge properties, although there is enough diversity and scatter in such properties, and in the results of different diagnostics, to preclude any rigorous statements.

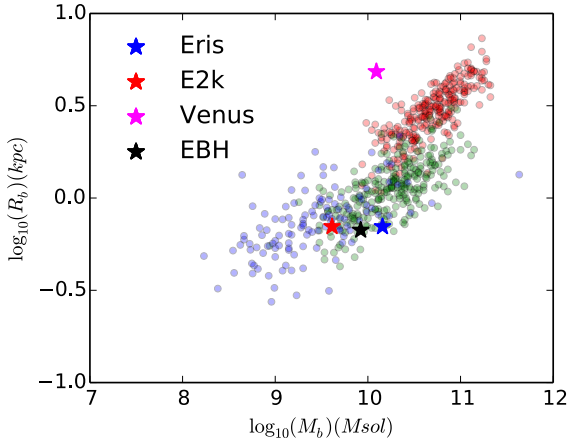

Figure 3.9: The comparison of bulge scale lengths of our sample of galaxies after the photometric decomposition as a function of the stellar mass of their "bulges" (stars) vs. the sample of SDSS elliptical galaxies (red circles), classical bulges (green circles), and pseudobulges (blue circles) from Gadotti (2009).

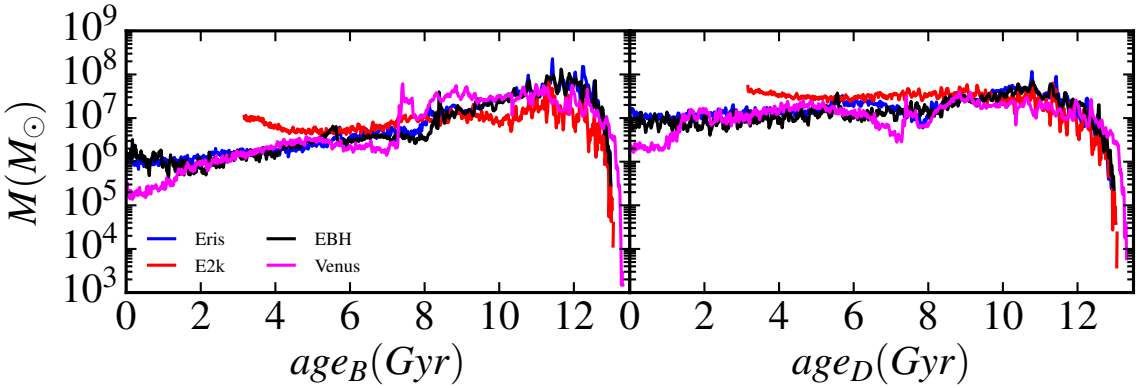

Figure 3.10: Mass distribution of stellar ages of spheroids (left) and disks (right), as would be measured at $z = 0$. Note that the lack of stars of ages lower than 3.5 Gyrs in E2k is due to $z_{\rm end} = 0.3$ of that run.

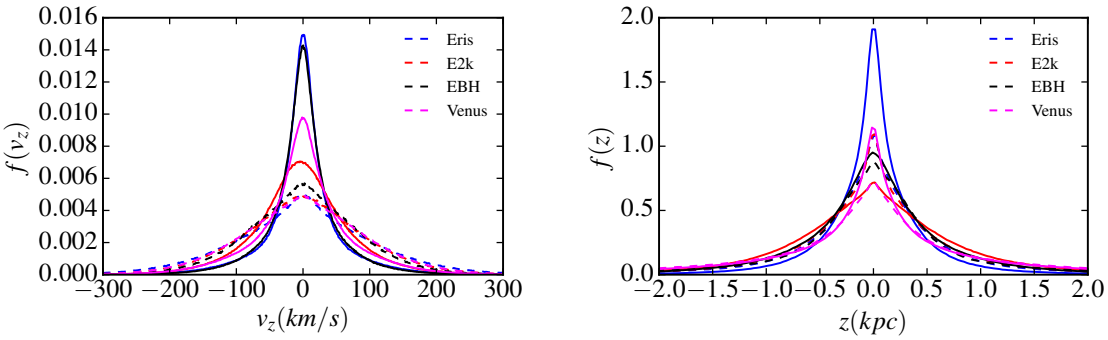

Figure 3.11: Distribution of the vertical kinematics and vertical locations of the stellar particles in galactic bulges (dashed lines) and disks (solid lines) at $z = z_{\rm end}$.

Chapter 4

Observability of hot halos around Milky Way-sized galaxies

Sokolowska, A., Mayer, L., Babul, A., Madau, P., Shen, S. 2016, ApJ, 819, 21

4.1 Abstract

We investigate the properties of halo gas using three cosmological 'zoom-in' simulations of realistic Milky Way-galaxy analogs with varying sub-grid physics. In all three cases, the mass of hot ($T > 10^6$ K) halo gas is $\sim 1\%$ of the host's virial mass. The X-ray luminosity of two of the runs is consistent with observations of the Milky Way, while the third simulation is X-ray bright and resembles more closely a very massive, star-forming spiral. Hot halos extend to 140 kpc from the galactic center and are surrounded by a bubble of warm–hot ($T = 10^5 - 10^6$K) gas that extends to the virial radius. Simulated halos agree well outside 20–30 kpc with the β–model of Miller & Bregman (2013) based on OVII absorption and OVIII emission measurements. Warm–hot and hot gas contribute up to 80% of the total gas reservoir, and contain nearly the same amount of baryons as the stellar component. The mass of warm–hot and hot components falls into the range estimated for L^* galaxies. With key observational constraints on the density of the Milky Way corona being satisfied, we show that concealing of the ubiquitous warm–hot baryons, along with the ejection of just $20 - 30\%$ of the diffuse gas out of the potential wells by supernova–driven outflows, can solve the "missing baryon problem". The recovered baryon fraction within 3 virial radii is

90% of the universal value. With a characteristic density of $\sim 10^{-4}$ cm^{-3} at $50 - 80$ kpc, diffuse coronae meet the requirement for fast and complete ram–pressure stripping of the gas reservoirs in dwarf galaxy satellites.

4.2 Introduction

Spiral galaxies are embedded in coronae of diffuse gas that connect intergalactic medium (IGM) to the star-forming disks of galaxies (Putman et al., 2012). In the absence of any feedback processes, the corona is supplied with accreting gas from intergalactic medium and in turn, the cooling gas from corona provides fresh fuel for star formation. In the presence of feedback, however, outflows from the galaxy also contribute to the corona and may even expel the coronal gas beyond the galactic halo. Thus the ebb and tide of the coronal gas is part and parcel of the galaxy formation process.

High–resolution cosmological simulations performed with hydrodynamical zoom–in codes have made significant progress in reproducing a wealth of galaxies' properties in various mass ranges (dwarfs: Shen et al. (2014); spiral galaxies: Guedes et al. (2011), Marinacci et al. (2014a), Agertz & Kravtsov (2015), Roškar et al. (2014); massive early–types: Fiacconi et al. (2014)), yet the interplay between cooling and heating, and the exchange of mass between galaxies and IGM remain open issues. Crain et al. (2013) inspected gas around massive disc galaxies reproducing X–ray scalings and found that electron densities of hot coronae are dominated by IGM accretion. Recently, the properties of gaseous galactic halos were characterized in massive ($10^{12} M_{\odot}$) halos at $z = 2$ by Nelson et al. (2015) who also pinpoint that inflow stream morphologies become continuously more complex with better numerical resolution. In the Milky Way regime, Marinacci et al. (2014b) emphasized the importance of galactic winds in shaping the structure of circumgalactic medium. These studies have only just scratched the surface in terms of understanding the nature and properties of galactic coronae in simulated galaxies. Such coronae can potentially yield a wealth of complementary constraints on the fidelity of the simulations, as well as on the details of the sub–grid physics, including star formation, radiative cooling and feedback processes. Earlier simulations, which were not succeeding in forming realistic galaxies due to gas overcooling and weak feedback, routinely obtained overly massive hot gaseous coronae and yielded X–ray luminosities an order of magnitude higher than the contemporary observational constraints (Governato et al.,

2004).

Another unresolved issue in galaxy formation is the so-called *missing baryon problem*. Big Bang Nucleosynthesis and three independent cosmological probes – cosmic microwave background (CMB, $z \sim 10^3$), modeling of the Lyman α forest ($z \sim 3$), hot gas fraction in galaxy clusters ($z \sim 0$) – yield $\Omega_b \approx 0.04$ (e.g. Planck Collaboration et al., 2014). However, close to our epoch ($z < 2$) the number of baryons detected add up to just over half of the number seen at $z > 2$ (Nicastro et al., 2005; Fukugita & Peebles, 2004), and on the galactic scales it is even less than that, e.g in Milky Way (Dehnen & Binney, 1998; Sommer-Larsen & Dolgov, 2001), or in M31 (Klypin et al., 2002). In principle, if a substantial portion of gaseous halo's baryons was 'invisible' in infrared, optical or UV light, but shined and absorbed far–UV and X–ray photons, it would pose a major observational challenge due to the faint and extended nature of coronae around spirals. Successful characterization of such medium would require large–field and highly sensitive instruments, which are not yet available.

Nevertheless, the existence of such corona has been confirmed to date in various ways. For instance, it has been detected in ultraviolet and X–ray absorption lines of OVI and OVII against bright background sources (Sembach, 2006; Wang et al., 2005; Peeples et al., 2014; Fang et al., 2015), in OVIII emission (Gupta et al., 2009; Henley & Shelton, 2013), and as excess X–ray emission relative to the background (Rasmussen et al., 2009; Anderson & Bregman, 2011; Bogdán et al., 2013; Tumlinson et al., 2011). Predicted warm–hot (10^{5-6} K) and hot (over 10^6 K) gas in galactic halos seems to be a generic feature, as it is found not only in the Milky Way (Rasmussen et al., 2003; Bregman & Lloyd-Davies, 2007; Miller & Bregman, 2014), but also in extragalactic sources (Anderson & Bregman, 2011; Bogdan et al., 2013). Thus, there is a clear consensus on the sizable contribution of such gas of halo origin to the baryonic budget (Nicastro et al., 2005; Gupta et al., 2012). Nevertheless, mock observations of recent realistic simulations of Milky Way–like galaxies and halos reveal that the detected gas is only a part of the full picture, as some of baryons are missing due to the obscuration by the dense foreground disk. As a consequence, observations of the MW's CGM using various metal lines would generally miss 50% of CGM gas (Zheng et al., 2015). However, even with this degree of boosting, the MW's CGM mass would still be low and therefore, it is unclear whether the coronal gas entirely solves the missing baryon problem (e.g. Danforth & Shull, 2008; Miller & Bregman, 2013; Werk et al., 2014). Additionally,

as discussed in Wu et al. (2001), if halos contained excessive concentration of hot X-ray emitting gas, this may lead to the over-prediction of the soft X–ray background.

In case hot and warm–hot galactic coronae cannot solve the missing baryon problem while simultaneously satisfying key observational constraints, other factors must come into play. Growing body of observational work shows that galactic outflows are ubiquitous (e.g. Martin, 2005; Bradshaw et al., 2013; Turner et al., 2015), therefore baryons could be expelled from the potential wells of galaxies by means of jets, winds and photoionization input from AGN, SNe and OB stars. The resulting distribution of gas would be smoother and more diffuse, reducing the likelihood of detecting this large reservoir of baryons in the Universe. Silk (2003) developed an analytic model for such galactic outflows, suggesting that the supernova–driven ejection of gas could act before a galaxy assembles (see also Benson et al., 2003; Murray et al., 2005). Hence, a galaxy could already be born baryon deficient.

Early hydrodynamical simulations of large cosmological volumes of Davé et al. (2001) predicted that the missing baryons could be contained in intergalactic warm–hot and hot medium at temperatures $10^5\ K < T < 10^7\ K$. Numerical simulations with effective models of SNe feedback such as momentum and energy–driven winds have been extensively studied by Davé and collaborators (e.g. Finlator & Davé, 2008; Oppenheimer & Davé, 2008; Ford et al., 2013). Davé (2009) found that such winds eject a large fraction of the baryons beyond the potential wells of the galaxies and that this effect is stronger for low–mass halos. According to their findings, the Milky Way–sized halo at $z = 0$ is expected to retain 60% of baryons within the potential well, and the effect of outflows may extend to as far out as 3 virial radii of the galactic halos. Slightly weaker but still significant baryonic winds are found at $z > 2.5 - 5$ in recent hydrodynamical zoom–in simulations of individual galaxies, in which outflows are generated from the thermal coupling of the SN energy to the surrounding gas (Shen et al., 2012, 2013).

The goal of this paper is to use three cosmological zoom–ins of Milky Way–sized galaxies from the Eris suite (Guedes et al., 2011; Mayer, 2012; Shen et al., 2013) to address the abundance of the warm–hot and hot gas in the galactic coronae, along with the larger scale WHIM. In addition to the original Eris, we use runs with the same initial conditions but a much richer inventory of physical processes. We focus on the properties of the present–day diffuse coronae, as well as on the impact of varying sub–grid physics on the results. Finally, we compare them to the available observational constraints on the density of the

Run	z_l	$M_{vir}(z_l)$ (10^{11} $M_\odot$)	$R_{vir}(z_l)$ (kpc)	IMF	MC	UVB	c^*	n_{SF} (cm^{-3})	ϵ_{SN} (10^{51}erg)
Eris	0	7.6	233	K1993	low–T	HM1993	0.1	5	0.8
ELE	0	7.8	235	K1993	low–T	HM1993	0.05	5	0.8
E2k	0.5	6.5	170	K2001	all–T	HM2012	0.1	100	1.0

Table 4.1: Virial masses and radii of the Milky Way–sized runs were calculated at the final redshift of each run z_l. Notation: MC – metal cooling, c^* – star formation efficiency, n_{SF}– star formation density threshold, ϵ_{SN}: supernovae efficiency parameter, HM1993: **?**, HM 2012: Haardt & Madau (2012), K1993: Kroupa et al. (1993), K2001: Kroupa (2001).

Component	M_{Eris} ($10^{10}M_\odot$)	M_{ELE} ($10^{10}M_\odot$)	M_{E2k} ($10^{10}M_\odot$)
warm and cold gas ($< 10^5 K$)	1.20	1.27	1.22
warm–hot gas ($10^{5-6} K$)	3.02	3.98	2.43
hot gas ($> 10^6 K$)	0.63	0.72	0.69
total gas	4.85	5.97	4.34
total stellar	3.41	2.75	3.38

Table 4.2: Total masses of various components were calculated within virial radii at the corresponding redshift.

Milky Way gas (Gatto et al., 2013; Miller & Bregman, 2014; Werk et al., 2014) in order to determine whether coronae arising in the simulations may be regarded as realistic. We note that successful recovery of the basic properties of the Milky Way corona is a cornerstone of the forthcoming in–depth study of the coronal assembly (Sokolowska et al., in preparation, hereafter Paper II).

This paper is outlined as follows. In section 2 we motivate why we investigate this particular set of runs and describe the physics included in the simulations. Section 3 contains our results in the context of Milky Way observables and is followed by the summary in section 4.

4.3 Methods

Here we use three unique high–resolution simulations of spiral galaxies performed with the treeSPH code Gasoline (Wadsley et al., 2004) that comprise more than 18 million particles spread over a 90 Mpc box. These runs are all zoom–in simulations of Milky Way–sized galaxies (Table 4.1) that are evolved in the full cosmological context in a Wilkinson Microwave Anisotropy Probe 3-year cosmology, $\Omega_M = 0.24$, $\Omega_\Lambda = 1 - \Omega_M$, $\Omega_b = 0.042$, $H_0 = 73$ km

$s^{-1}Mpc^{-1}$, $n = 0.96$, $\sigma_8 = 0.76$. The first of the runs, Eris, has been shown to be extremely successful, owing to the recovery of various Milky Way properties (Guedes et al., 2011). Namely, 1) its rotation curve is in good agreement with observations of blue HB stars in the Milky Way, and it reproduces the kinematic properties of SDSS halo stars (Rashkov et al., 2013), 2) stellar mass and the disk scale length are both comparable to the values adopted for our Galaxy, 3) bulge-to-disk ratio determined by a two-component fit to the i-band surface brightness profile is typical of Sb spirals and Sbc galaxies, 4) the pulsar dispersion measure gave plausible constraints to the hot halo of the Milky Way (see more in Guedes et al., 2011).

The two other simulations known as ErisLE (here ELE, Bird et al., 2013) and Eris2k (denoted as E2k, Shen et al. in preparation) are the follow–ups of the original Eris. We picked these follow–ups out of a larger set of variants because they made major improvements to the original run and at the same time were able to produce realistic galaxies. We discuss some of these improvements below.

The recipes for star formation and feedback in all runs are the same. Gas particles must be dense (denser than n_{SF} specified in Table 4.1) and cool (cooler than $T_{max} = 30000K$) to form stars. Particles which fulfill these requirements are stochastically selected to form stars, based on the commonly used star formation equation $\frac{dM_*}{dt} = c^* \frac{M_{gas}}{t_{dyn}}$, where M_* is mass of stars created, c^* is a constant star formation efficiency factor, M_{gas} is the mass of gas creating the star, and t_{dyn} is the gas dynamical time. Each star particle then represents a population of stars, covering the entire initial mass function. Stars larger than 8 $M_\odot$ explode as SNII. According to the model of Stinson et al. (2006), the feedback is purely thermal, as the blastwave shocks convert the kinetic energy of ejecta into thermal energy on scales smaller than simulations can resolve. Once energy is ejected, particles receiving the energy are prevented from cooling. The reason for this is to mimic two effects: 1) turbulence in molecular clouds, which inhibits star formation by means of heating up particles, and 2) a high pressure of the blastwave, as high–temperature gas naturally flows outwards.

The star formation efficiency parameter was lowered in ELE with respect to Eris in order to further improve the observed normalization of the star formation density in local galaxies (Governato et al., 2010). All other parameters remained the same, as indicated in Table 4.1 (for a more detailed discussion, see Bird et al. (2013)). In contrast, E2k retains the star formation efficiency of Eris but represents a new generation of runs with a richer inventory of physical processes. These processes include new sub–grid turbulent diffusion prescription

for both metals and thermal energy, as well as cooling via metal lines (Shen et al., 2010, also see the next paragraph). In essence, metals significantly enhance the cooling of the WHIM, while metal diffusion contaminates large amounts of otherwise pristine gas. Shen et al. (2010) have shown that metals mix between winds and surrounding gas before they leave the galaxies, decreasing the metal content in the WHIM and diffuse IGM but increasing it in the galactic halo.

The radiative cooling rates in Eris and ELE (hereafter referred to as the first–generation runs) are obtained by solving non–equilibrium differential equations of primordial gas in the presence of cosmic ionizing background (Wadsley et al., 2004). Additionally, gas of $T < 10^4$ K cools through fine structure and metastable lines of C, N, O, Fe, S and Si (Bromm et al., 2001; Mashchenko et al., 2007). E2k run, instead, employs tabulated cooling rates for metal lines at all temperatures. These rates are calculated with the photoionization code CLOUDY (Ferland et al., 1998), which assumes that metals are in ionization equilibrium. This is a good approximation when extragalactic UV radiation is present.

The strength of feedback depends on the number of produced supernovae, which is in turn governed by the initial mass function. The IMF in Eris and ELE was based on Kroupa et al. (1993), while in E2k an updated IMF was used (Kroupa, 2001). This difference translates into nearly 3 times more stars in the mass range of $8 - 40\ M_\odot$ in the run with the new IMF. Other significant modifications in the parameters of E2k that might boost feedback are: doubled cooling shut–off time, higher supernovae efficiency parameter ϵ_{SN} and the higher star formation density threshold n_{SF} (see Table 4.1). The latter formally increases the star formation rate by a factor of 4.5, since the star formation rate scales as $\sqrt{n_{SF}}$ (see e.g. Guedes et al., 2011; Mayer, 2012). Locally the supernovae rate will therefore increase by the same amount for a given IMF. This has been shown to improve fidelity of galaxies' properties by means of lowering baryonic densities and stellar masses (Mayer, 2012).

E2k is a run that follows an extensive study of sub–grid parameters. The final parameters were chosen in order to closely match the stellar mass–halo mass relation predicted by abundance matching as a function of redshift (e.g. Behroozi et al., 2014). The E2k setup, including the detailed discussion of the stellar component and the structure of the disk, will be presented in the forthcoming paper (Shen et al. in preparation).

In this work we focus on the diffuse ionized gas component exterior to the galactic disk, i.e. the component traced by gas particles of temperatures *over* $3 \cdot 10^4$ K. Our classification

of the gas phases encompassed by such component is inspired by conventions introduced by observers (Putman et al., 2012). Specifically, we term *warm gas* the phase comprising particles at $3 \cdot 10^4$ K$< T < 10^5$ K, *warm–hot gas* that with temperature in the range 10^5 K$< T < 10^6$ K, and *hot gas* the phase at $T > 10^6$ K.

4.4 Results

Given that the E2k has not yet been run to $z = 0$, we compare all three runs at the last common redshift, i.e. at $z = 0.5$. There is no major merger after $z \sim 2$ in any of the runs and no major satellite is accreted below redshift $z \sim 0.5$ (Pillepich et al., 2015). As a consequence, the thermodynamical state of the gas at $z = 0.5$ should not differ appreciably from that at $z = 0$, and we have verified this in the case of Eris and ELE.

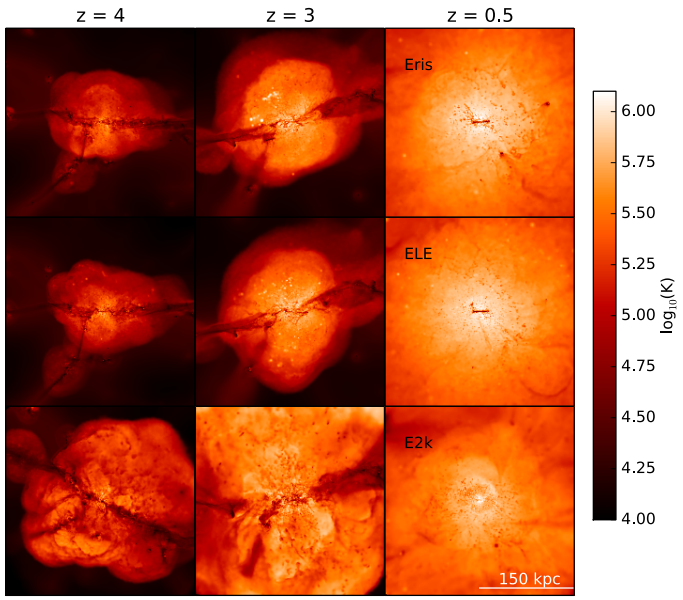

Figure 4.1: Temperature maps of the three representative runs: Eris (top row), ELE(middle) and E2k (bottom row), scale is in the physical units (kpc). Snapshots correspond to three example evolutionary time steps. Virial radii in all three runs are approximately $r_{vir} = (30, 50, 170)$ kpc for the corresponding redshifts $z = (4, 3, 0.5)$. Note the white region at $z = 0.5$ – it is a signature of the spherically–shaped hot coronae.

The most significant similarity of all runs lies in the amount of gas residing in the warm–hot phase at $z = 0.5$, together with the hot gas mass (see Table 4.2). Warm–hot and hot gas together are of the order of stellar mass, and constitute as much as 72–80% of the total

gas content, substantially exceeding the contribution of warm and cold (i.e. $T < 3 \cdot 10^4$ K) gas. This has important implications for the missing baryon problem (see Section 4.4.1).

Fig. 4.1 illustrates the evolution of the gaseous halo across three representative times for the first–generation runs, and for E2k. Filamentary feeding occurs very early on (at $z = 4$) as IGM loads mass into the neighborhood of a protogalaxy. The effect of feedback associated with the majestic expanding bubble seen between redshifts $z = 4$ and $z = 3$ facilitates redistribution of energy and mass far beyond the virial radius. With the passage of time, the halo starts resembling an onion–like structure – a corona of hot gas is embedded in a warm–hot bubble. As argued above, significantly more supernovae explode in E2k relative to the first–generation runs, which explains the differences in temperature between the top and bottom panels of Fig. 4.1. Also, in E2k the stronger feedback can push baryonic matter much farther out from the potential well of the galactic halo with respect to the first–generation runs.

All runs feature generic accumulation of warm–hot and hot gas component through the combination of feedback and shock–heating after the last major merger ($z < 3$, see Figure 4.1). The specific role of these distinct processes in building the galactic halo will be addressed in Paper II. In the remainder of this section we will present the late–time properties of the corona and focus on how they compare with the latest observational constraints on the diffuse gaseous halo of the Milky Way.

4.4.1 Mass budget of the corona

In Fig. 4.4.1, we present the cumulative radial distribution of warm–hot and hot gas mass normalized to the virial mass at $z = 0.5$. Although E2k clearly stands out (red lines), Eris and ELE exhibit similar distribution of both components, with a slight overabundance of gas in ELE with respect to Eris, likely due to the lower efficiency in turning gas into stars.

All three runs share a common attribute – hot gas attains a fraction of the virial mass of order 1%, and the location of this maximum indicates that hot coronae are enclosed within $\sim$100 kpc at $z = 0.5$ (see also Fig. 4.1). At $z = 0$ this translates into hot phase gas enclosed within $\sim$140 kpc, hence much below the virial radius of the galaxy. It is the warm–hot medium that extends to the virial radius ($r_{vir} \sim 240$ kpc at $z = 0$) and beyond. We note that the size of the Milky Way gaseous halo is still a huge uncertainty – according to studies of Local Group by Nicastro et al. (2002) and Rasmussen et al. (2003), the corona of hot gas

Run	f_b ($< r_{vir}$)	f_b ($< 2\ r_{vir}$)	f_b ($< 3\ r_{vir}$)
Eris	0.124 (71%)	0.145 (83%)	0.160 (91%)
ELE	0.130 (74%)	0.149 (85%)	0.162 (92%)
E2k	0.117 (67%)	0.115 (66%)	0.129 (74%)

Table 4.3: Baryonic fraction f_b at $z = 0.5$ was calculated for three spherical regions characterized by a multiple of a virial radius. Numbers in brackets correspond to the percentage of the recovered baryons with respect to the predictions of the Wilkinson Microwave Anisotropy Probe 3-year cosmology, i.e. $f_b = 0.175$. The same cosmological parameters were used to generate initial conditions of all 3 runs.

may extend to 1 Mpc or over 140 kpc respectively; Bregman & Lloyd-Davies (2007) favor the range of 15–100 kpc, while Gupta et al. (2012) mention over 100 kpc.

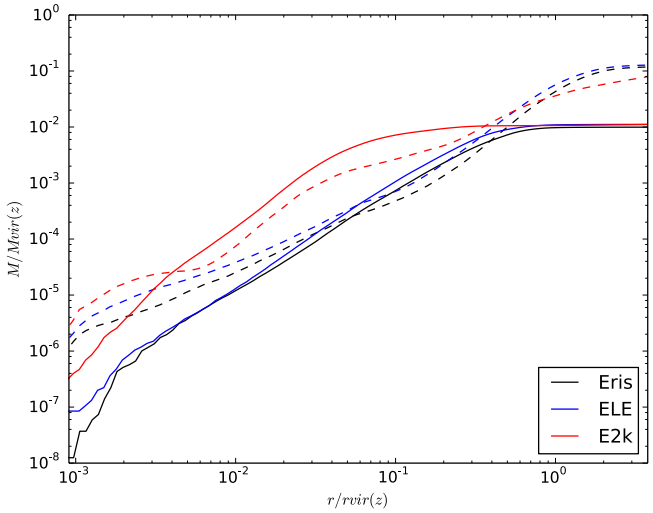

Figure 4.2: Radial profile of the cumulative mass of warm–hot gas (dashed) and hot gas (solid) at $z = 0.5$ for three independent runs. Both mass and radial bins are normalized to the exact virial mass $M_{vir} = (6.5, 6.7, 6.5)\ 10^{11}\ M_\odot$ and virial radius $r_{vir} = (168.5, 170.4, 169.7)$ kpc of Eris, ELE, E2k respectively.

Despite these similarities, we find considerably higher proportion of hot and warm–hot gas in the inner part of the E2k halo relative to the first generation runs, which signals higher efficiency of feedback. We would then expect this to be true even at larger radii, while instead close to the virial radius the relative proportions of hot gas are the same as in the other runs, and of warm–hot gas the lowest of all, as shown in Figure 4.4.1.

Differences in the cooling schemes provide one viable explanation. In this scenario the enhanced metal cooling in E2k transforms the hot phase into the warm–hot phase more efficiently. This would be more evident further away from the center, as the competitive effect of heating by feedback becomes progressively weaker. Similarly, metal cooling below $10^6 K$ could replenish the warm and cold gas phase more efficiently at the expense of the warm–hot gas. This effect should be even stronger, given the higher gas densities implied in this case, as well as the fact that the cooling curve peaks near few times 10^5 K.

However, the numbers presented in Table 4.2 disprove that scenario, as total mass of warm–hot gas of E2k is the lowest of all, and we observe no significant difference in the mass of warm and cold gas relative to the other runs. We thus conclude that some gas in E2k is heated to higher temperatures by stronger feedback and simply leaves the halo. The stronger baryonic outflow is indeed confirmed by the clear difference in the baryon fraction within R_{vir} between E2k and the first generation runs shown in Table 4.3.

The extent, as well as the total mass fraction of the warm–hot medium, are of particular importance for the missing baryon problem. In three independent runs the warm–hot medium exceeds the hot phase in mass by a factor of 4–5. Moreover, as indicated in Table 4.2, warm–hot gas itself constitutes the majority of the global gaseous budget of each galaxy. When the warm–hot component is removed from the calculation, the baryonic fraction amounts to 42–47% of the universal value at $z = 0.5$, in fact a fraction that is very close to the one observed at $z < 2$ (Nicastro et al., 2005).

With the warm–hot gas in the picture, the baryonic fraction is much higher than the one quoted above, though lower than the one inferred from the WMAP3 cosmology (see the first row of Table 4.3). We recover about 67%–74% of the cosmic baryon budget within the virial radius. We are roughly consistent with the work of Davé (2009), who finds that the baryonic fraction in the present–day Milky Way–sized halos ($\sim 10^{12} M_{\odot}$) drops to about 60% of the cosmic value. This agreement is striking, given the very different sub–grid recipes for feedback, as well as more than an order–of–magnitude difference in mass and spatial resolution of the simulations. We note, however, that the different feedback recipe that we adopt is likely crucial in obtaining realistic properties at the level of the galactic disk and below (e.g. Bird et al., 2013; Guedes et al., 2011).

Next, we investigated the efficiency of feedback–driven galactic winds in removing baryons within the different runs. We therefore calculated baryonic fractions within 2 and 3 virial

radii (Table 4.3) and found that they increase substantially beyond the galactic halos, which reveals that galactic halos are surrounded by large reservoirs of baryons. Note that there is a correlation between strength of feedback and the value of the baryonic fraction, that is the stronger the feedback, the lower the mass of baryons encompassed. E2k attains the lowest value of all, while ELE as the run of the lowest stellar mass (hence the weakest feedback) exhibits the highest f_b.

We thus conclude that galactic outflows triggered by supernova feedback are responsible for the *missing* of a significant fraction of the baryons from the galactic halos, and these baryons can be found mostly in warm–hot intergalactic medium that extends even further than 3 virial radii (Fig. 4.4.1). The fact that the first–generation runs assembled up to 92% of cosmic mean in baryons within 3 virial radii suggests that the missing of the baryons is likely a scale–dependent effect. Once the baryonic census is undertaken by designing observations of warm–hot and hot gas extending to sufficiently large radii around virialized structures, the missing baryon problem might be ultimately explained.

4.4.2 Density and entropy of the galactic corona

In this section we scrutinize various components: baryons, stars and gas to pinpoint the differences in thermodynamics of the runs that nevertheless lead to similarities content–wise. To display the collective effect of thermodynamical processes, we use mass density distributions of gas phases mentioned in section 4.3 normalized to the critical density of the Universe at $z = 0.5$, as well as radial entropy profiles. The proxy for entropy that we assumed here is commonly used in studies of clusters (e.g. Babul et al., 2002; Voit et al., 2005; McCarthy et al., 2008), and is defined as $S = k_B T / n_e^{2/3}$. We note that the distributions of the first–generation runs are seemingly alike, therefore we chose Eris to be representative of these in comparison with E2k (see Fig.4.4.2).

Certain similarities are visible at the first glance, such as the dominance of the stellar content in the inner part where the galactic disk resides, along with the convergence of total gaseous and baryonic distribution outside the disk (see Fig. 4.4.2, top row). E2k however exhibits higher stellar concentration in the very center, and so higher concentration of baryons. Nevertheless, a steeper stellar density slope of E2k cancels out this difference, as the total stellar mass for both runs at $z = 0.5$ amounts to $3.4 \cdot 10^{10} M_{\odot}$.

Sub–grid physics behind the two generations of runs shapes the intrinsic properties of the

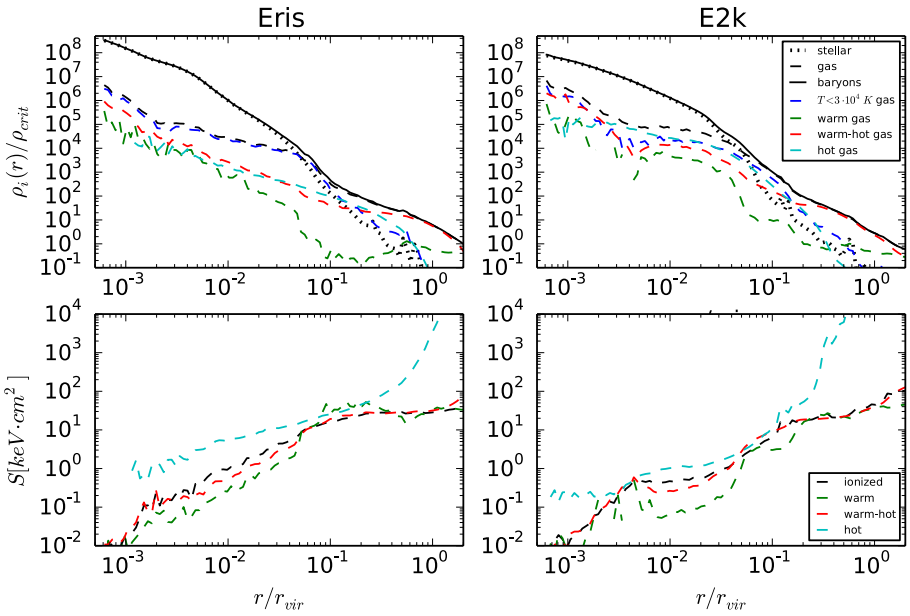

Figure 4.3: Top row: mass density distributions of stars (dotted black), gas (dashed black) and baryons (solid black) at $z = 0.5$. Particular constituents of gas are presented with colored dashed lines (see legend). Although we concentrate on the ionized gas in this work, we included mass density of cold gas of $T < 3 \cdot 10^4$ K (blue dashed line) as well. Bottom row: entropy of ionized gas phases that incorporate an additional *ionized* term to denote all ionized particles.

galactic disks. As a consequence, it governs mass distributions of gas phases, e.g. leading to the closer confinement of hot gas in E2k. Cold gas with temperatures below $3 \cdot 10^4 K$ dominates the first–generation runs in the center, whereas E2k exhibits a comparable contribution of cold, hot and warm–hot gas from ~ 350 pc outward, probably facilitated by the diffusion of metals and thermal energy. Outside a region inhabited by a galactic disk, all simulations appear to have been mildly affected by the tremendous differences in the disk, such as very high metallicity of the disk gas (Shen et al. in prep.). Beyond 0.2 r_{vir}, warm–hot medium forms the majority of baryons, while cold and warm components are allocated comparably.

The warm medium exhibits a characteristic drop down in its mass density distribution (green dashed line in Fig. 4.4.2) localized at roughly 0.4 r_{vir} and continues up to a point where hot and warm–hot gas eventually begin to saturate the cumulative distribution of their mass. A resulting feature, the *density dip*, underlines an on–going thermodynamical process that triggers a local decrement of warm gas. When combined with the temperature maps, which show lack of warm gas in the vicinity of the dip starting at $z = 1$ (visible later

as the hot region in Fig. 4.1), a causal connection with some event implied in the assembly of the corona is strongly suggested. Further time–evolution analysis is necessary to address the origin of such feature and will be undertaken in Paper II.

Cooling and heating mechanisms leave their imprint in the entropy distribution, therefore entropy itself carries information about the thermodynamical history of the gaseous halo. In the bottom row of Fig. 4.4.2 we present a preliminary result of the analysis of the entropy of gaseous halo constituents. The entropy profile of warm gas reflects specific features of the density distribution, due to nearly constant temperature profile of that phase. Hence, the density dip manifests itself as an *entropy bump* in Fig. 4.4.2 (bottom row), indicating the possible deposition of heat in that region.

We note that entropy profiles presented here were shown for the phases as we defined them since the beginning of the paper. In principle, useful physical insight could be gained by re–defining phases based on eventual regularity in their entropy profiles, for example highlighting possible near–equilibrium configurations. Such an approach would be physics–driven rather than observationally–driven, and will be adopted in Paper II. Nevertheless, the entropy of the diffuse component is free of potential bias, and appears to be consistent with predictions for the hot X–ray emitting gas in clusters, as discussed in the next paragraphs.

Unlike the case of the warm phase, the temperature profiles of warm–hot, hot and all ionized gas are far more complex than simple power laws. Reflecting the different strength of radiative cooling and heating by feedback, the shape of entropy profiles of such phases differs substantially between the runs. For example, the entropy distribution of hot gas in Eris has a shallower slope than any other component up to 0.1 r_{vir}(cyan line), whereas in E2k flattens towards the center of the halo in a sort of "entropy core", resembling that found in some galaxy clusters. In both cases entropy rises dramatically beyond that radius, though at a different rate. Therefore entropy, as widely shown in the literature on galaxy cluster simulations, is a sensitive diagnostic of sub–grid physics.

Despite differences, we identify a generic feature – the entropy distributions of the warm–hot component (red line) and the entire ionized gas (black line) are nearly identical for a given run. This follows from the fact that warm–hot medium constitutes the majority of the overall gas mass. Moreover, the specific entropy of the ionized gas is leveled in both cases between 0.1– 1 r_{vir} and reaches $40 - 50$ keV cm^2 at the virial radius. We compared with McCarthy et al. (2008) that this is consistent with the value of a characteristic entropy at

large radii expected for a halo of mass of order $10^{12} M_{\odot}$. In case of E2k, the entropy rises further beyond the virial radius, which is due to the stronger effect of feedback, as discussed in section 4.4.1.

4.4.3 X–ray luminosity

One of the hot halo thermal properties that can be readily compared with the observations is the X–ray luminosity. We compute the $0.5-2.0$ keV band X–ray luminosity of the coronal gas using the radiative rates of Astrophysical Plasma Emission Code3 (APEC) from Smith et al. (2001). APEC assumes the optically thin gas in collisional ionization equilibrium. The final value is a sum over the X–ray luminosities of individual gas particles within a distance r_{vir} of the halo center, taking into account contributions to line and continuum emission associated with each of the individually tracked elements (iron, oxygen, hydrogen and helium). Total X–ray luminosity is defined as

$$L_X = \sum_k n_{e,k} n_{i,k} \Lambda_k V_k, \tag{4.1}$$

with $n_{e,k}$ the number density of electrons, $n_{i,k}$ the number density of ions, $V_k = m_k/\rho_k$ the volume and Λ_k the cooling rate of an individual gas particle k. The resultant X–ray luminosities for Eris, ELE and E2k are: 4×10^{39} erg s^{-1}, 10^{40} erg s^{-1} and 3×10^{42} erg s^{-1}, respectively.

Snowden et al. (1997) modeled a bulge of hot gas surrounding the Galactic center, based on the maps of the soft X-ray background from the ROSAT all-sky survey. They assumed a cylindrical geometry with an exponential fall–off of density. At the radial extent of ~ 5.6 kpc and a scale height ~ 1.9 kpc, the total luminosity in the 0.5–2 keV band that they find is $\sim 2 \cdot 10^{39}$erg s^{-1}. Other constraints follow from Wang (1998), who characterized the soft X–ray background of the hot polytropic corona of the Galaxy, using all–sky ROSAT emission. In their model, Galactic corona is assumed to be axisymmetric and quasi–hydrostatic. The integrated luminosity in the 0.5–2 keV range that they find is $\sim 3 \cdot 10^{39}$erg s^{-1}. More recently, Miller & Bregman (2014) reported the X–ray luminosity of the Milky Way corona in that band in the metallicity–dependent range of $0.8 - 5.0 \cdot 10^{39}$erg s^{-1}. They confirm the luminosity found by Wang (1998) for the $Z = 0.3\ Z_{\odot}$ corona, which lies in–between the mean metallicities of the gaseous galactic halos of Eris ($Z \sim 0.1\ Z_{\odot}$) and Eris2k ($Z \sim 0.6\ Z_{\odot}$),

and is comparable with the mean metallicities of hot gas beyond 20 kpc (in our simulations, $Z \in (0.22, 0.26) Z_{\odot}$). We conclude that the X–ray luminosities of the coronae of Eris and ELE are consistent with the constraints inferred for the Milky Way corona, whereas E2k attains L_X that is 100 times higher than these constraints.We discuss this difference in section 4.5.

Numerous works reported measurements of X–ray luminosities of the coronae of other spiral galaxies, which cover the broad range of luminosities found in our runs. For example, Bogdan et al. (2013) find luminosities of order $\sim 2 \cdot 10^{40}$erg s^{-1} in the radial bin (0.05–0.15) r$_{vir}$ of massive halos ($\sim 10^{13} M_{\odot}$) of highly star–forming (15 $M_{\odot} yr^{-1}$) spirals. Bogdan et al. (2015) attempted to detect X–ray coronae around lower–mass spirals and derived the 3σ limits on their characteristics. The smallest objects in their sample – NGC 1097, NGC 5170 – have estimated SFRs of $(5.8, 0.4)$ $M_{\odot}$yr^{-1} and radii enclosing 200 times the Universe's critical density of $r_{200} = (238, 269)$ kpc, which roughly corresponds to the enclosed halo masses of $M_{200} \simeq (1.6, 3.7) \cdot 10^{12} M_{\odot}$. The measurements yield the upper limits on their X–ray luminosities in the 0.5–2 keV band of order $(1.5, 3.0) \cdot 10^{39}$erg s^{-1}, respectively. Among other works, Strickland et al. (2004) measured 0.3–2 keV band luminosity of a Milky Way–like, L^* galaxy NGC 891 and obtained $L_X = 1.3 \cdot 10^{39}$erg s^{-1}, while Tüllmann et al. (2006) reported gas luminosities in the same band of $9 \cdot 10^{38}$erg s^{-1} and $3 \cdot 10^{38}$erg s^{-1} for two non–starburst, "normal" SBc, Sc galaxies NGC 3044 and NGC 4634.

4.4.4 Comparison with the Milky Way corona

Understanding the true nature of galactic coronae is a crucial part of the galaxy formation theory. In order to assess our models, we need to determine whether the structure of the simulated halos agrees with the available observational limits. In what follows, we describe three most recent works focused on constraining the number density of the Milky Way halo gas, as well as discuss how our three runs compare with observed Milky Way–like galaxies.

One of the most recent successful detections of hot gas in the Milky Way is based on the measurements of column densities of electrons derived from OVII absorption lines (see Sembach, 2006; Bregman & Lloyd-Davies, 2007; Miller & Bregman, 2013). Miller & Bregman (2013) find their absorption measurements to be well described by a spherical β model

$$n_e(r) = n_o[1 + (r/r_c)^2]^{-3\beta/2}, \tag{4.2}$$

hereafter denoted as M&B model. Due to low number of targets passing near the Galactic center, the degeneracy between central density n_o and the core radius r_c occurs. Therefore in the regime $r >> r_c$ (typically $r_c \lesssim 1$ kpc) the function may be approximated by $n_e(r) \approx n_o(r_c/r)^{3\beta}$ with $n_o r_c^{3\beta} = 0.013^{+0.016}_{-0.010}$ cm^{-3} kpc$^{3\beta}$ being the core density, and $\beta = 0.56^{+0.10}_{-0.12}$ the slope at large radii, parameters found for the optically thin medium. This asymptotic profile is what we use in this work as the reference data.

Miller & Bregman (2013) derive the electron number density profile, $n_e(r)$, from the electron column density N_e. As shown in their work, the latter is related to the metallicity Z and OVII ionization fraction f of the gas as $N_e \propto f^{-1}Z^{-1}$. Metallicity and ionization fractions are assumed to be constant in the M&B model, i.e. $Z = Z_\odot$ and $f = 0.5$ throughout the entire gaseous halo. This is an oversimplification, as in reality both of these quantities have radial distributions. We therefore modify the above M&B model by replacing the constant factors with the functions of the distance $Z = Z(r)$ and $f = f(r)$ that are inferred from the simulations. We explain this procedure in more detail below.

The distances between an observer at $r = 0$ and a target r_i are in fact equivalent to the path lengths l_i. Following the M&B model, since the number of targets is limited, we assume both the spherical symmetry and the constant mean number density $\bar{n}_{e,i}$ between these targets (see also Bregman & Lloyd-Davies, 2007). Then, for example, equation (3) holds in case of the first target in a sample, while the number density towards the next target can be obtained from the equation (4).

$$N_{e,1} = \int_0^{l_1} n_e dr = \bar{n}_{e,1} l_1 \tag{4.3}$$

$$N_{e,2} = \int_0^{l_2} n_e dr = \int_0^{l_1} n_e dr + \int_{l_1}^{l_2} n_e dr = \bar{n}_{e,1} l_1 + \bar{n}_{e,2}(l_2 - l_1) \tag{4.4}$$

In general, with known path lengths l_i and electron column densities $N_{e,i}$, the mean number density of each spherical shell $\bar{n}_{e,i}$ can be obtained recursively, according to

$$N_{e,i} = \int_0^{l_i} n_e(r) dr = \sum_i \bar{n}_{e,i}(l_{i+1} - l_i). \tag{4.5}$$

Combined information about the number densities between available targets allows for the recovery of the approximate distribution $n_e(r)$.

Total electron column density N_e stems from the measured column density of oxygen ions, N_{OVII}, hence the relationship $N_e \propto f^{-1}Z^{-1}$ cited above. We thus apply the correction for $f(r)$ and $Z(r)$ in two steps: 1) we remove the constant Z and f, which is a straightforward multiplication of equation (5) for all i, 2) we correct each slab of volume between the targets individually for its mean metallicity $\bar{Z}_i$ and mean ionization fraction of OVII $\bar{f}_i$ computed in the simulation. In this procedure the re–calibration factor $\bar{f}_i^{-1}\bar{Z}_i^{-1}$ is thus simply a scaling factor applied to the integrals that varies shell–by–shell. We re–calibrate each run separately in this way.

As our simulations do not trace OVII, we use the photoionization code CLOUDY to compute, in post–processing, the ionization fractions of oxygen for each SPH particle. The code assumes an optically thin slab of gas at the density, temperature and metallicity of the SPH particle, irradiated under an isotropic cosmological UV background (Haardt & Madau, 2012). The effect of local radiation is not included in the calculation.

In Figure 4.4.4, we present a comparison of the total electron number density distributions inferred from our simulations (Eris at $z = 0$ and E2k at $z = 0.5$) and the two corrected M&B model curves. The sharp drop-off in the electron density profile at about 10 kpc likely signals the extent of the star–forming disk. Clearly, the Eris run agrees with the predicted density distribution for the Milky Way even in the central part, while the E2k run fails to recover the inner 30 kpc.

Different metallicity and ionization fraction profiles of the runs trigger the discrepancy between the two theoretical curves in Fig. 4.4.4 in this region (dashed lines). As seen in Fig. 4.4.2, E2k has a higher density of hot gas in the center than the first generation runs, which goes hand in hand with the higher ionization fraction in the vicinity of the disk (roughly a factor of 6). Additionally, metals are consistently more abundant within the radial 30 kpc – we refer to this in section 4.5. Both, the higher ionization fraction and metallicity are causally linked to the more powerful SN feedback in E2k.

Despite the differences in the inner part of the corona, this simulation and the derived corrected M&B model results are in excellent agreement beyond the immediate vicinity of the disk (within the error bars). Additionally, Anderson & Bregman (2010) report an average electron number density between the Sun and LMC (50 kpc) of 5×10^{-4} cm^{-3}. In Eris and E2k, the mean electron number densities are 3×10^{-4} and 5×10^{-4} cm^{-3}, respectively.

Another constraint follows from Gatto et al. (2013), who deduced upper and lower limits

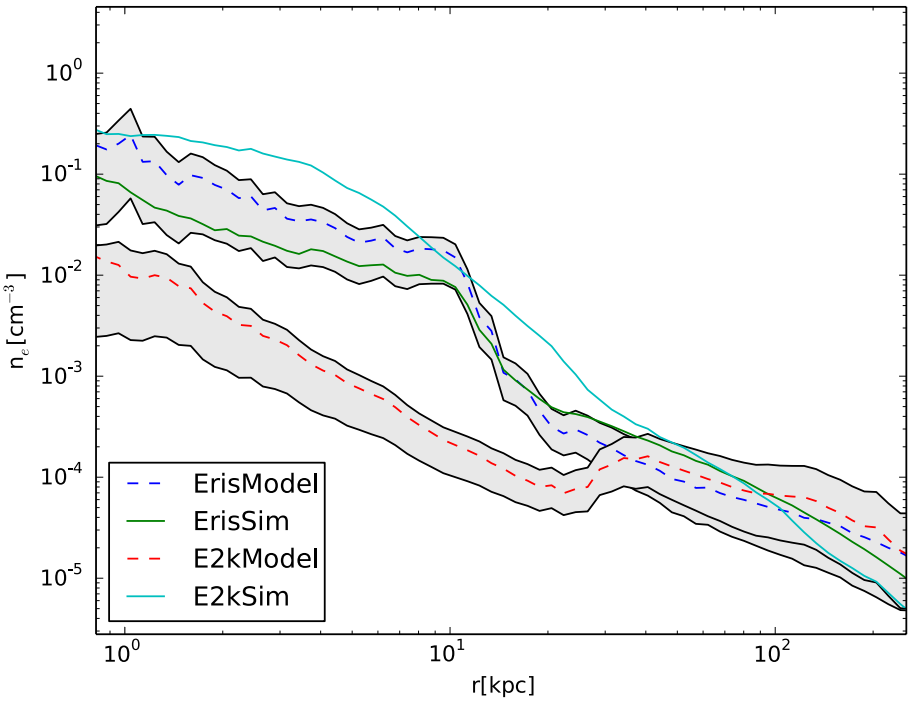

Figure 4.4: Total electron number density of the Milky Way inferred from corrected M&B models – ErisModel, E2kModel (dashed lines) – set against our MW-like runs ErisSim, E2kSim (solid lines). Both runs are presented at the latest redshift this time, i.e. Eris is plotted at $z = 0$, while E2k at $z = 0.5$. The grey shaded regions represent expected error bars on OVII absorption measurements taken from Miller & Bregman (2014).

on the number density of the Milky Way gaseous halo from the argument of ram–pressure gas stripping of dwarf satellites Sextans and Carina. We use their results as yet another test for the similarity of the gas in simulations and in the Milky Way and we set them in Fig. 4.4.4, where we present coronal number density distributions at different redshifts. n_{cor} incorporates all particles: neutral atoms (in the part where cold gas resides), ions and electrons. The density of gas necessary to efficiently remove gas from the Milky Way dwarfs (shown by the data points with the corresponding error bars) is in excellent agreement with the density of gas in all simulations, as long as satellites plunge in to at least $50 - 80$ kpc, which is expected based on the estimates for the orbital parameters of most dSphs.

Recently, Salem et al. (2015) modeled the ram pressure stripping of another satellite of Milky Way, LMC, both analytically and numerically. They obtained a lower value than Gatto et al. (2013), namely 1.1×10^{-4} cm^{-3} at ~ 50 kpc , which we also show in Fig. 4.4.4. This

density is also lower than the gas density in all three of our simulations, by approximately a factor of 3. We will discuss the scatter in halo density inferred from the observations as well as the apparent tension between the Salem et al. (2015) results and our simulations further in section 4.5.

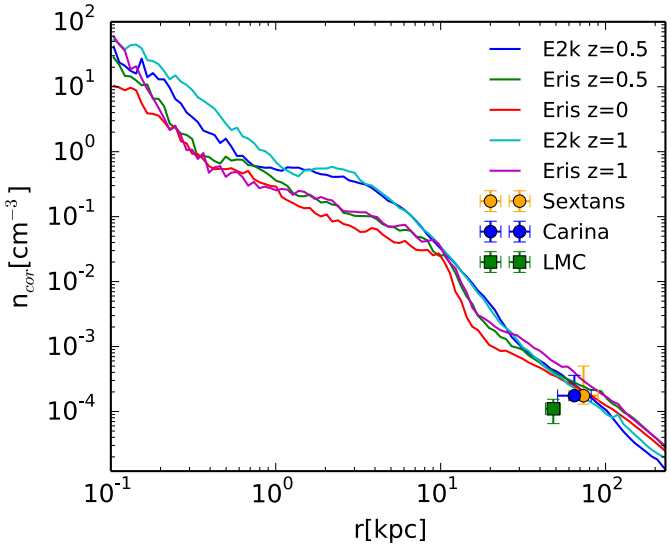

Figure 4.5: Spherically–averaged gas number density profiles in Eris and E2k after $z = 1$. The two data points for satellites Sextans and Carina were taken from the Table 6 of Gatto et al. (2013) , and the data point for the LMC is from Salem et al. (2015).

4.4.5 $L \sim L^*$ galaxies

In sections 4.4 and 4.4.1 we discussed the relevance of warm–hot and hot phases in accounting for the missing baryons, and in Table 4.2 we compared their masses to the other baryonic components. Here, we perform another comparison with observations that addresses the weight of the different phases as a fraction of the cosmic baryonic budget. The data is inferred from the recent analysis of a large sample of bright galaxies surveyed by COS (Werk et al., 2014, see also references therein). COS investigated gaseous halos of 44 $L \sim L^*$ low–redshift galaxies extending out to 160 kpc away from the center – in fact a value that corresponds to the virial radius of our simulated galaxies at $z = 0.5$. While the direct focus of the survey was to use a set of low ionization–state tracers to measure the mass of the gas at $T < 2 \times 10^5$ K, it combined input from other surveys of tracers of hotter gas to

provide a fairly complete census. Werk et al. (2014) assumed the cosmic baryon fraction of 0.17 M_{vir}, therefore, to be consistent, we change their normalization from 0.17 to 0.175 which is a cosmic baryonic fraction in the cosmological framework of the simulations.

We calculated that the combined warm–hot and hot components in the simulations represent 32%, 40% and 27% of the baryonic budget in Eris, ELE and E2k respectively, which agrees with the predicted range of 7–45% in the COS Halos, assuming the cosmic baryon fraction in the WMAP3 cosmology. Given the large span between the lower and the upper limit on the mass of the components, we treat this comparison with caution. The tendency of our results to lie at the upper end of the values inferred by Werk et al. (2014) reflects the fact that their typical galaxy has a higher fraction of warm and cold gas relative to what we find in our runs.

Among caveats to take into account in this comparison is that the mean estimated halo mass in the COS sample, $10^{12.2} M_{\odot}$, is higher than the virial mass of our galaxies. In particular, the fiducial COS halo would lie above the transition mass scale between cold and hot mode dominance in the accretion flow, which could have an impact on gas thermodynamics. Furthermore, the stellar mass of the galaxies in the COS sample, which enters in the computation of baryonic mass fractions, is not determined observationally but simply deduced from the abundance matching. Finally, COS–Halos sample the redshift $z = 0.2$, while the simulation outputs are taken at $z = 0.5$. Notwithstanding these caveats, this comparison strengthens the relevance of our results, since it gives them statistical significance as opposed to restricting the comparison only to the Milky Way. As pointed out by Zheng et al. (2015), there are discrepancies between the mass budgets of MW's and COS halos' CGM, opening up a possibility that either the Milky Way is an outlier, or that the observations are still incomplete. Hence, this complementary comparison going beyond the Milky Way data is of a tremendous value for our results.

4.5 Concluding remarks

In this paper we presented three simulations of MW–like galaxies. It is important to emphasize that these simulations are high–resolution zoom–ins carried out in a fully cosmological context. These simulations produce disk–dominated galaxies that are devoid of overcooling problem or an overly massive stellar component, as thoroughly discussed in previous pa-

pers on the Eris suite of simulations. The differences in gas distributions between Eris and ELE were minor, therefore we chose Eris to represent the group regarded here as the *first–generation* runs. E2k run differs from that group, as it comprises richer inventory of physical processes. As will be discussed in Shen et al. (in prep.), E2k yields a lower stellar mass at high redshift relative to first generation runs, showing a better agreement with abundance matching. At the same time, it hosts a more turbulent, thicker disk compared to that of Eris and ELE, which in turn closely match the structural and kinematical properties of the MW disk (Bird et al., 2013).

Despite the differences between the three simulations, we found that hot gas constitutes nearly 1% of the total virial mass at $z = 0.5$ regardless of the thermodynamical model. The close confinement of the hot gas (within 100 kpc at that redshift) goes hand in hand with the morphology of that phase presented in the temperature maps at $z = 0.5$ of Fig. 4.1, justifying the usage of the term *corona*. The hot coronal gas is surrounded by an envelope of warm–hot gas that extends beyond the virial radius of a galaxy.

The warm–hot and hot gas together are of the order of stellar mass, and constitute as much as 72–80% of the total gas content. As they correspond to the matter in the temperature regime, which to date remains incompletely mapped, this unequivocally points to the possibility of the existence of undetected large reservoir of matter around spiral galaxies. It therefore favors the already known claim (Nicastro et al., 2005) that the warm–hot medium is a potential solution to the missing baryon problem.

COS–Halos results imply that most of the missing baryons actually reside within the virial radius of spiral galaxies , which is consistent with our findings. Indeed, all variations of Eris contain 67–74% of expected baryon budget at $z = 0.5$ (fractions in the same range are found at $z = 0$ for Eris and ELE). The relative contributions of the warm–hot and hot medium to the baryon budget are also consistent with, although closer to the upper end of, the range inferred for L^* galaxies by Werk et al. (2014). The latter work also reports a large amount of warm and cold gas, larger than both what we find in our simulations and what is found in the Milky Way, even after accounting for the mass in the MW halo likely missed by observers. The correction derived by Zheng et al. (2015) is premised on the fact that they find a good agreement between the kinematics of the CGM gas in their simulations and the observations of the CGM in COS-Halos. Our simulation results are not subject to this correction because it is not necessary for haloes viewed from the outside.

Zheng et al. (2015) reports that the HI mass of HVCs (high velocity clouds) corrected for the velocity obscuration and the HI mass of the high–velocity gas in the Magellanic System (excluding Magellanic Clouds) scales as $M_{HI} = 3 \times 10^8 (d[kpc]/55)^2 M_\odot$ (see also Putman et al., 2003, for the details on the origin of that relation). This in turn implies: 2.5×10^9 $M_\odot$ at 160 kpc, as opposed to 2×10^{10} $M_\odot$ reported by COS-Halos based on estimates derived from HI surveys and baryonic Tully-Fisher relation (see for the reference: Martin et al., 2010; McGaugh et al., 2010; Werk et al., 2014). In our simulations, the mass of HI at 160 kpc amounts to $1.5 - 3 \times 10^9$ $M_\odot$ and thus is in agreement with the Milky Way HI results.

Our results also suggest that either our MW-like galaxy formed in a region that was rendered somewhat baryon deficient by winds from smaller systems, from which our final galaxy was assembled (c.f. Liang et al., 2016; Ford et al., 2013) or that the remaining missing baryons were vented out of the dark halo by powerful supernovae–driven outflows. The fact that the first–generation runs assembled up to 93% of cosmic mean in baryons within 3 virial radii implies that the missing baryon problem is a scale–dependent problem, which would be solved by extending measurements sufficiently far from the virialized region of a halo.

Since the warm–hot medium is shown to be sensitive to the details of the simulation setup, measuring its density and entropy profiles in several nearby galaxies would yield important constraints on sub–grid models for galaxy formation, in contrast to that of hot coronal gas. The hot gas seems to be much less sensitive to significant changes in feedback strength in our simulations in terms of its extension and abundance. Once reliable spatial mapping of the warm–hot medium becomes available, in particular from near the galactic disk to beyond the virial radius, the baryon fraction as a function of radius will provide a stringent test for feedback models (Table 4.3).

Recently, Marinacci et al. (2014b) considered 8 gaseous halos of Milky Way-sized objects. Their temperature cuts of gas phases are similar to ours and some of their findings align well with the conclusions of this work. Namely, the cumulative mass profiles of the galaxies studied by Marinacci et al. (2014b) (see their Fig. 3) show clearly that their hot gas phase is confined within the inner halo, between 50 and 100 kpc, while their warm–hot phase extends beyond the virial radius and in most cases dominates the baryon budget of the diffuse halo. For these two phases, thus, results are in line with ours. However, their galaxies show a cool ($< 10^5 K$) phase, which often extends beyond the region of the hot corona and dominates over the latter in the baryon budget. This latter difference may be traced to differences in

the feedback model as well as in the numerical hydrodynamics technique (Lagrangian mesh vs. SPH).

For example, on the one hand the GASOLINE implementation of the SN feedback prevents a part of the heated gas from cooling on a Myr scale (Stinson et al., 2006), which could in principle facilitate retaining higher temperatures by the halo gas while at the same time depleting the reservoir of cool gas. On the other hand, the kinetic feedback implementation of Davé and collaborators (e.g. Finlator & Davé, 2008; Oppenheimer & Davé, 2008; Ford et al., 2013; Liang et al., 2016) and Vogelsberger et al. (2013) entails a component of hydrodynamically decoupled winds with cold ejecta. In the AREPO simulations (Vogelsberger et al., 2013), such winds have been found to trigger the formation of cold string–like features in the CGM. To prevent artefactual star formation in these regions, Marinacci et al. (2014a) split the energy given to the wind into equal thermal and kinetic parts, thus solving the problem with warmer ejecta. It has been shown that the intermediate gas phase between the low-density medium at temperatures around $10^{5.5}$ K and the dense cold gas in the proximity of a galaxy at temperatures of order 10^4 K is causally connected with the ejecta (Marinacci et al., 2014b), although AGN feedback and the cooling of the warm–hot gas are also at play. Thus, both the thermalization of the galactic wind energy and the cooling shut–off would have a non–negligible impact on the difference in the total cool ($< 10^5$ K) mass budget of Marinacci et al. (2014b) gaseous galactic halos and ours. We stress that these conjectures put forward here require actual testing by a direct comparison of the two types of simulations.

In this paper special attention has been given to the major constraints available on the Milky Way gaseous halo. Firstly, we computed X–ray luminosities of coronae in the 0.5–2 keV band. The X–ray luminosity of E2k is much higher than that of Eris or ELE because the coronal gas of E2k is hotter, denser and more metal enriched, which in turn boosts the radiative cooling rate. Moreover, E2k has a significantly higher star formation rate at $z < 1$ compared to Eris and ELE (Mayer et al. in prep.). The latter could be the result of both the stronger feedback delaying SF to low z and the metal cooling allowing for attaining higher star formation rates once the feedback becomes weaker. A very bright X–ray halo is thus likely connected with being still vigorously star forming, a state which is at odds with what is found for the Milky Way. Nevertheless, the X–ray luminosity of E2k lies within the range observed in normal galaxies.

Although one simulation, E2k, has an X-ray luminosity that is comparable with that of

very massive spirals, its L_X is 2 orders of magnitude higher than what is observed for the Milky Way. However, the other two runs are instead consistent with a number of constraints on the corona of the MW. In particular, their L_X is only a factor of 2 (Eris) and 5 (ELE) larger than the value for the $Z = 0.3$ $Z_\odot$ corona reported by Miller & Bregman (2014). This difference likely reflects the underlying assumption of the constant metallicity and a cooling flow in the calculation of L_X performed by Miller & Bregman (2014). Our results are free of these limitations.

Secondly, we were also able to fit well the spherical β model of Miller & Bregman (2013) to the electron number densities in our simulations, although the gas structure in the region within twice the radius of the disk turns out to be sensitive to the choice of the feedback model. More explicitly, very energetic feedback of E2k gives rise to the discrepancy in the electron density profile in the region up to 30 kpc that we attribute to both the higher ionization fraction and higher metallicity near the disk.

The agreement of the simulations with refined M&B model implies that electron number densities are rather unaffected by feedback strength beyond a radial distance of 30 kpc in contrast to the central part of the halo. A caveat is that all our runs adopted the same feedback sub–grid model, namely, blastwave feedback. Future investigations with radically different feedback models, such as the new superbubble feedback developed in GASOLINE2 (Woods et al., 2014), will be mandatory.

The growing body of observational work goes now beyond the OVII absorption measurements analyzed in this paper. Miller & Bregman (2014) recently published a similar analysis for OVII emission that is in good agreement with our simulations as well, though outside the galactic disk. The authors in the latter paper also report the independent measurements of OVIII emission, which are consistent with the OVII absorption model. We recall that in this paper we focused on the results of Miller & Bregman (2013) for the optically thin corona, although Miller & Bregman (2013) inspect the saturated case as well. Note that Miller & Bregman (2014) report a shallower slope β for the OVII emission line measurements than for the absorption line results in the optically thick regime. This discrepancy is expected due to a combination of their treatment of optical depth corrections and the overall variation in the OVII emission lines. It is because of the latter uncertainties, as well as the requirement of consistency accompanying computation of ionization fractions with CLOUDY, that we decided to focus our analysis on their optically thin model.

The total number densities of coronal gas are compatible with the number density inferred from Gatto et al. (2013), based on the ram–pressure stripping argument for dwarf galaxy satellites. While in their work authors explicitly focus on the single-phase, isothermal hot gas only, the constraints are general because ram pressure depends on the density of gas and the velocity of a dwarf, not the temperature of gas. We thus conclude that our halos could have stripped Sextans and Carina, as well as most MW dSphs with orbits coming within 100 kpc. Although the number densities of our simulations are slightly higher than the estimate from the ram pressure stripping of LMC, this discrepancy could stem from the fact that Salem et al. (2015) use the Miller & Bregman (2013) best–fit without accounting for the metallicity gradient in gaseous halos. In fact, such correction would make the number density profile shallower, hence closer to our results. Moreover, the tidal interactions between the LMC and SMC must play a dominant role in shaping the gaseous Magellanic System, likely causing some of the gas stripping. Not accounting for this effect places an important limitation on the model of Salem et al. (2015). All in all, our results lend support to models, in which the combination of tidal shocks and ram pressure stripping alone explains the origin of dSphs as the descendants of an early in-falling population of gas–rich dwarfs (Mayer et al., 2007).

With the increasing adequacy of cosmological, hydrodynamical simulations of MW–like galaxies, we have reached the era when the gaseous galactic halos have become realistic. Thus with this work we fulfilled the key requirement to justify the future usage of the Eris suite of simulations in order to understand in depth the physical nature, assembly and evolution of the coronal gas, which will be the focus of Paper II. As suggested by the present–day entropy distributions, distinct gas phases likely had different thermodynamical histories. Therefore extending our work to multiple tracers, especially for the warm-hot and warm phase, such as CII, SiIII, MgII (e.g. Herenz et al., 2013), as soon as the sensitivity of observational instruments enables mapping of their spatial distributions, will be of tremendous value to constrain the physics implemented in the simulations.

Chapter 5

Processes that yield X-ray coronae

Sokolowska, A., Babul, A., Mayer, L. et al., arXiv:1708.07820

5.1 Abstract

We use cosmological hydrodynamical simulations of Milky Way-sized halos with different feedback strengths or merger histories to investigate the formation of X-ray luminous coronae. We show that a galactic corona is not a consequence of hot spherical accretion onto a galaxy but of mergers-induced shock heating and supernova feedback. Coronae grow inside-out and detach galaxies from the filamentary network as they outbalance the pressure of cold flows. Additionally, ram pressure strips cold flows at the intersection of the two fronts. Coronae thus drive the transition from the cold mode to hot mode accretion. Our results predict the presence of gas at high temperatures even as early as $z = 3 - 4$, and in halos of much lower mass than the critical mass for hot mode accretion suggested by previous simulations and analytical models (Dekel et al.). All this is quite different from the standard picture in which diffuse halos are a consequence of the thermalisation of kinetic energy derived from gravity and/or the geometric effect of cross sections of halos vs. filaments, and may be more relevant for halos harbouring typical spiral galaxies. We show that SN feedback impacts the galaxy-cold flows connection, which has also consequences for the large-scale gas supply and may contribute to galaxy quenching.

5.2 Introduction

Normal galaxies observed today are surrounded by envelopes of diffuse gas, which can attain temperatures exceeding $10^5 - 10^6$ K (see the review on gaseous halos by Putman et al., 2012). Such media have already been detected in ultraviolet and X–ray absorption lines (Sembach, 2006; Wang et al., 2005; Bregman & Lloyd-Davies, 2007; Peeples et al., 2014; Miller & Bregman, 2014; Fang et al., 2015), in OVIII emission (Gupta et al., 2009; Henley & Shelton, 2013), and as excess X–ray emission relative to the background (Rasmussen et al., 2009; Anderson & Bregman, 2011; Bogdán et al., 2013; Tumlinson et al., 2011). The direct detection of hot halo gas ($T > 10^6$ K) at extragalactic distances is currently possible only around massive galaxies (e.g. Anderson & Bregman, 2011; Bogdan et al., 2013), but in the future a more sensitive X-ray observatory such as *Athena+* may bring spatially resolved images also of lower-mass spirals (Kaastra et al., 2013). For the time being, the hot halo around our Galaxy is the best probe of hot halos around lower-mass galaxies ($M_{halo} \simeq 10^{12} M_{\odot}$). Recent modelling of a million degree gaseous halo in the Milky Way results in a hot halo mass estimate of $M(200kpc) = 3.8 \times 10^{10} M_{\odot}$ (Miller & Bregman, 2013).

The question of the origin of diffuse gas has been under investigation for several decades. Until about a decade ago, the standard paradigm of galaxy formation assumed that dark matter relaxes to a virial equilibrium, and gas follows the dark matter during collapse (Rees & Ostriker, 1977; White & Rees, 1978). The resulting supersonic accretion triggers an accretion shock (Binney, 1977). The shock develops at the virial radius or closer to the galaxy, depending on the ratio of the cooling and dynamical timescales (White & Frenk, 1991). In this framework, halos in the mass range $M_{halo} \simeq 10^{12-13} M_{\odot}$ are expected to support an accretion shock at their virial radius, and thus contain a quasi-hydrostatic atmosphere of hot gas. A detailed analytical treatment of shock stability in Birnboim & Dekel (2003) brought down the critical halo mass for a stable shock at the virial radius to over $10^{11} M_{\odot}$ for primordial gas and around $10^{12} M_{\odot}$ for solar metallicity gas. The accretion shock relies on the presence of a stable atmosphere of post-shock gas to support itself.

However, both the models of White & Frenk (1991); Birnboim & Dekel (2003) assumed spherical symmetry, and thus could not capture the scenario of asymmetric halo configurations. 3D simulations have revealed that most of the gravitational cooling radiation comes from gas at temperatures far below the typical virial temperatures of galaxies (Fardal et al.,

2001),and that a significant fraction of gas in galaxies at the low-mass end of this range has never been shock heated (Katz et al., 2003; Kereš et al., 2005, 2009; Dekel et al., 2009; Brooks et al., 2009). Kereš et al. (2005, 2009) showed that, for all halos below a critical mass of $3 \times 10^{11} M_{\odot}$ and at redshifts in range $z = 0 - 3$, the infall is predominantly cold. In fact, these simulations have identified two thermodynamically and geometrically distinct modes of accretion: "cold mode" (filamentary inflow resulting in the maximum gas temperature that is lower than the virial temperature) and "hot mode" (spherical accretion with heating of gas up to $T > 10^{5-7}$ K before cooling, see also Dekel & Birnboim, 2006; Kereš et al., 2009; Dekel et al., 2009). The diffuse X-ray luminous halo is thus generated by the hot mode accretion, in halos which grow sufficiently in mass (i.e. beyond the critical mass threshold). The time of this transition depends on the halo growth rate but is often seen around $z \sim 2$. This picture, however, has yet to be reassessed in the presence of effective feedback scheme preventing excessive star formation, particularly in the high redshift universe, which was foreshadowed by White & Frenk (1991). This is the main topic of this paper.

We focus on the Milky Way mass scale in order to probe the impact of supernova feedback on the evolution of the diffuse halo. This is motivated by the observed presence of both gas at $T \simeq 10^{5-6}$ K and significant mass of cold, neutral gas in high velocity clouds (Putman et al., 2003). The simultaneous existence of both phases of gas suggests that the Milky Way ($M_{halo} \simeq 10^{12} M_{\odot}$) is undergoing a transition between cold and hot accretion. Supernova feedback is still very important on this mass scale (see a review of Somerville & Davé, 2015). It is a crucial ingredient for regulating star formation in galaxies and drive winds. Either alone or in combination with other stellar feedback processes, such as radiation pressure or photoionization, is crucial to obtain realistic stellar and baryonic masses and star formation efficiencies, perhaps up to a mass scale as large as $10^{13} M_{\odot}$, and especially as it shapes the lower-mass end of the galaxy mass function (e.g. Bower et al., 2012; Puchwein & Springel, 2013). Various forms of stellar and SN feedback can reproduce the structure of disk galaxies satisfactorily, both at the level of global parameters and internal properties in various mass ranges (dwarfs: Shen et al. (2014); spiral galaxies: Guedes et al. (2011), Marinacci et al. (2014a), Agertz & Kravtsov (2015), Roškar et al. (2014); massive early–types: Fiacconi et al. (2014)).

van de Voort et al. (2016) have shown that the diffuse X-ray luminosity around galaxies correlates with the star formation rate up to a few times $10^{12} M_{\odot}$, as expected if feedback

plays a role in the origin of an extended gaseous corona up to a certain mass scale. However, a detailed study of its impact on the build-up on the hot mode in high-resolution simulations is lacking. We thus test the possibility that hot diffuse galactic coronae do not reflect shock-heating induced by gravitational infall, rather are the consequence of feedback-driven heating and outflows. This is particularly important from the point of view of galaxy formation, as the transition from cold to hot accretion seems to be the key to galaxy quenching (Dekel & Birnboim, 2006). Observations reveal a robust bimodality in the galaxy population which divides into the so-called blue and red sequences. The threshold for the transition between these sequences is $3 \times 10^{10} M_{\odot}$ (equivalent to a critical halo mass of $\simeq 10^{12} M_{\odot}$).

In the previous paper (Sokołowska et al., 2016, hereafter Paper I), we studied present-day diffuse halos of Milky Way-sized galaxies using a suite of zoomed-in simulations. Our foundational model, Eris, employs subgrid physical recipe for supernova feedback, which turned out to be successful in reproducing a realistic Milky Way-like galaxy (Guedes et al., 2011). We showed in Paper I that this recipe also results in a realistic present-day gaseous halo with key properties being in agreement with recent constraints: namely, a X-ray luminosity in the 0.5-2 keV band of $\sim 10^{39}$ erg/s; coronal density sufficient to ram-pressure strip Milky Way satellites; and radial halo electron density profile consistent with that implied buy the OVII absorption line measurements (see Paper I for the details). Additionally, we studied a run with much stronger supernova feedback in the same context, E2k (Shen et al., 2012). We identified a feature in our simulated galaxies that we referred to as *a corona*. Coronae are central regions of hot gas with temperatures exeeding 10^6 K, characterised by approximately spherical geometry and a high degree of localization, as they tend to extend no farther than 100-140 kpc (0.6 r_{vir}). They are embedded in massive reservoirs of baryons of T= 10^{5-6} K.

In this second paper in the series, we address the question of their origin. We investigate the key physical processes that build the MW-like halos and their coronae, including supernovae (SN) feedback and merger-induced shocks, both of which are known to raise the temperature of the halo gas. To do so, we run a default subgrid model of Eris with SN feedback off, ErisNFB, and compare the resultant halo with the original variant of Eris. This work also includes a new run in the inventory of our hydrodynamical zoom-in simulations, namely Venus, which represents a case with a violent merger history (Sokołowska et al., 2017).

This paper is outlined as follows. In section 2 we motivate why we investigate this

particular set of runs and describe the physics included in the simulations. Section 3 contains our results in the context of the inside-out growth of the coronae and the role of feedback in their formation. We also explore the connection between the growth of coronae and the cold filamentary network. This is then followed by the summary in section 4.

5.3 Simulations

We use two unique high-resolution simulations of spiral galaxies, Eris and Venus, performed with the tree-smoothed particle hydrodynamics (SPH) code GASOLINE (Wadsley et al., 2004) with mass resolution $m_{\rm dm} \simeq 9.8 \times 10^4$ M$_\odot$ and $m_{\rm SPH} \simeq 2 \times 10^4$ M$_\odot$, and spatial resolution $\simeq 120$ pc. These runs are all cosmological zoom-in simulations of Milky Way-sized galaxies. Additionally, we investigate the consequences of the exclusion of feedback (model of Eris without supernova feedback, see section 3.2), as well as include a discussion of the impact of enhanced feedback on our results (model E2k, see the Appendix).

The first of the runs, Eris, has been shown to be successful in matching various properties of late-type spirals such as the Milky Way (Guedes et al., 2011). The second run, Venus, adopts the same subrgrid model as Eris but with different initial conditions (IC). These ICs were chosen to have an active merging history down to a low redshift in contrast to the quiet merging history of Eris, while at the same time ensuring that final virial halo mass ($\sim 8 \times 10^{11}$ M$_\odot$) and a halo spin parameter ($\lambda \sim 0.03$) are the same in both Eris and Venus.

Both simulations include radiative and Compton cooling. The radiative cooling is computed for a simple mixture of H and He via non-equilibrium cooling rates in the presence of the ionizing cosmic ultraviolet (UV; Haardt & Madau 1996) background (Wadsley et al., 2004). Additionally, gas of $T < 10^4$ K can cool through fine structure and metastable lines of C, N, O, Fe, S, and Si (Bromm et al., 2001; Mashchenko et al., 2007).

The recipes for star formation and SN feedback are the same in all the runs and are described in Stinson et al. (2006). Briefly, gas particles must be dense – namely have a density above the threshold $n_{\rm SF}$ (5 atom cm^{-3}) – and cool (cooler than $T_{\rm max} = 10^4$ K) in order to form stars. Particles that fulfill these requirements are stochastically selected to form stars according to $dM_*/dt = c^* M_{\rm gas}/t_{\rm dyn}$, where M_* is the mass of stars created, c^* is a constant star formation efficiency factor (set to 0.1 in all runs), $M_{\rm gas}$ is the mass of gas creating the star, and $t_{\rm dyn}$ is the gas dynamical time. Each star particle then represents a

population of stars, covering the entire initial mass function (IMF). We adopt the Kroupa et al. (1993) IMF.

In all the runs, metals come from SNI and SNII (Stinson et al., 2006). Stars more massive than 8 $M_\odot$ explode as SNII. According to the "blastwave feedback" model of Stinson et al. (2006), feedback is purely thermal, as the blastwave shocks are expected to convert the kinetic energy of ejecta into thermal energy on scales smaller than those resolved by our simulations. Once energy is ejected (the fraction of SN energy that couples to the interstellar medium is $\epsilon_{\rm SN} = 0.8$), particles receiving the energy are prevented from cooling for typically 10–50 Myr, with the cooling shut-off timescale being computed as the sum of the Sedov–Taylor (Taylor, 1950; Sedov, 1959) and snow-plough phases in the ejecta (McKee & Ostriker, 1977). By delaying the cooling, we model in a phenomenological way the unresolved effect of momentum and heating by turbulent dissipation in the ejecta before they reach the radiative phase. Delaying the cooling also prevents artificial overcooling of gas heated by SN feedback. The strength of feedback depends on the number of SNe produced, which is in turn governed by the IMF and, locally, by the star formation density threshold.

The Venus simulation employs different initial conditions than Eris. The ICs of Eris were generated with GRAFIC2 (Bertschinger, 2001). The "zoom-in" of Venus was initialized using the MUSIC code (Hahn & Abel, 2011), which allows a computationally more efficient topological identification of the Lagrangian subvolume for the refinement. Eris and Venus both form at the intersection of four dark matter filaments, but their convergence pattern is different (see Figure 5.1). In general, Venus experiences twice as many major mergers as Eris, with the last major merger (defined as a merger with mass ratio > 0.1 between the two galaxies) occurring at $z = 0.9$, as opposed to $z = 3.1$. While in Eris, a central dominant halo assembles very early, in Venus, multiple progenitors of comparable mass evolve separately for a long time, with one single halo and its associated galaxy only appearing after the last major merger at $z < 0.9$. The amount of substructure at $z = 0$ is also more abundant in Venus relative to Eris, both in the stellar and in the dark matter component. In particular, a large satellite orbits around the primary galaxy in Venus even at late times, causing a perturbation on the main disk at pericenter passages, the last of which induces perturbations in the structure of the main disk as late as $z = 0.24$.

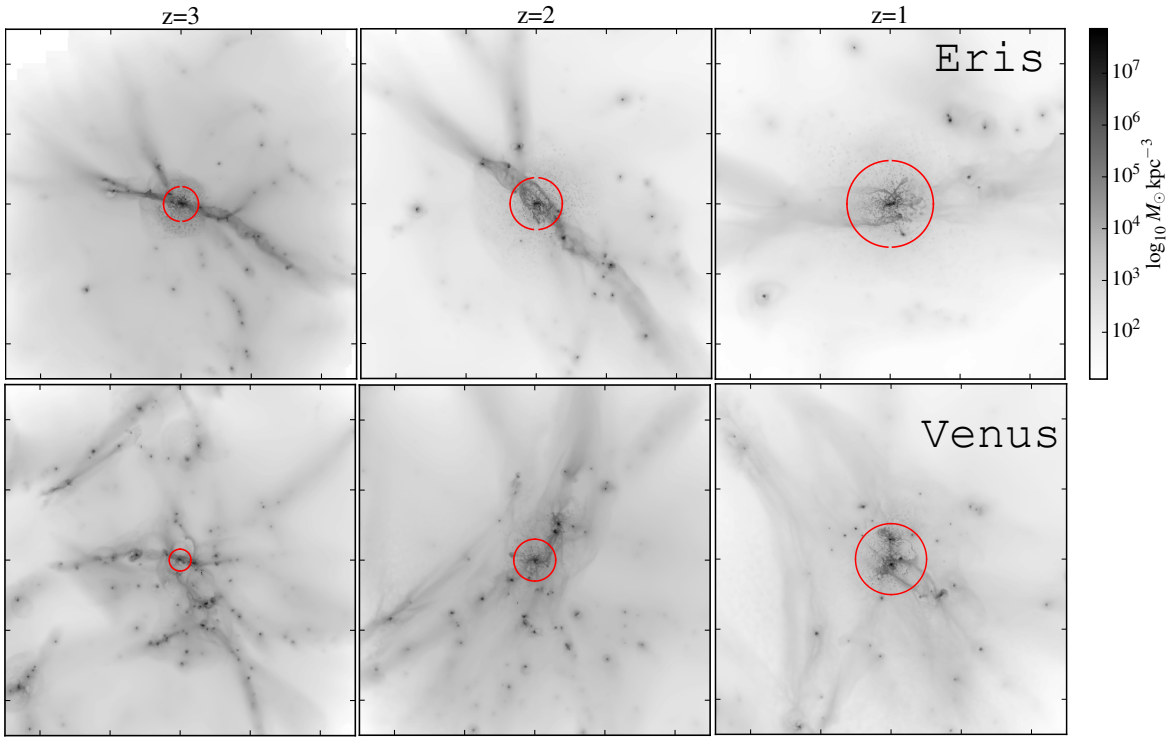

Figure 5.1: Density maps of gas around edge-on galaxies in two examples of initial conditions: quiet (Eris) and active (Venus). Width of each square is 1 comoving Mpc. The cross sections of the halo at each time step are shown as red circles.

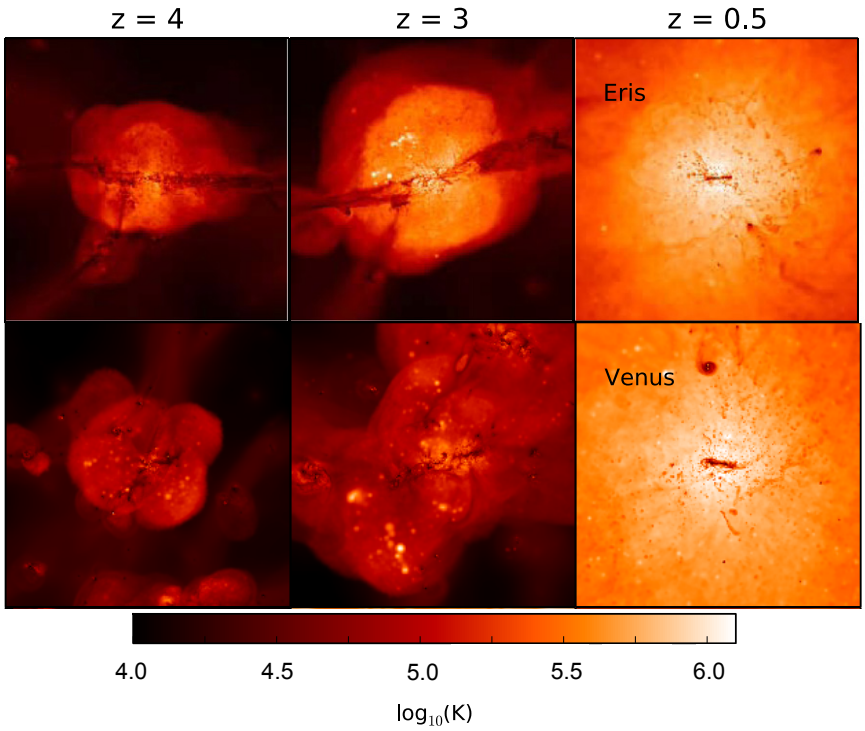

Figure 5.2: Two pathways to the same result: a galaxy surrounded by an X-ray-bright corona. Temperature maps of the gaseous halo of Venus and Eris are shown at three various timesteps. The width of each square is 300 comoving kpc. Compare with Fig. 1 of Sokołowska et al. (2016).

5.4 Results

In Paper I, we defined the hot corona to be the gas at $T > 10^6$ K localized in a spherical region around the main galaxy with a radius of about 100 kpc at $z = 0.5$ (140 kpc at $z = 0$, equivalent to 0.6 R_{vir}). We observed that gaseous halo undergoes a transformation over time that creates an onion-like structure, with the hot corona being embedded in the warm-hot (10^{5-6} K) envelope rich in baryons. The properties of this diffuse gas in Eris turned out to be in good agreement with a range of observational constraints on the Milky Way halo gas, including the X–ray luminosity in the 0.5-2 keV band (Snowden et al., 1997; Wang, 1998; Miller & Bregman, 2014, $\sim 10^{39}$erg/s).

Here, we start by assesing Venus. As previously, we compute the X-ray luminosity of all its gas particles that can be found within the virial radius of a halo. Our calculation is based on the radiative rates of Astrophysical Plasma Emission Code3 (APEC) (Smith et al., 2001), which assumes the optically thin gas in collisional ionization equilibrium (for more details on the calculation, see Paper I). With this method, the X-ray luminosity of Venus is $L_X = 1.2 \times 10^{39}$ erg/s, hence also in good agreement with the Milky Way observations.

Figure 5.2 compares temperature maps of gas of Eris and Venus at three different time steps: $z = 4, 3, 0.5$. The configuration of the filamentary network of these two simulations is different, resulting in two distinct evolutionary sequences for the gas. For example, at $z = 4$, cold flows penetrate the halos of both of the main progenitors but gas in Eris is hotter. At $z = 3$, a hot bubble of gas in Eris is associated with single main progenitor, whereas in Venus diffuse gas is distributed among multiple progenitors. By $z = 0.5$ Venus acquires a similar corona as Eris, albeit through a different evolutionary pathway.

The existence of similar diffuse halos that appear in different environments opens a question of what governs their evolution, and how they arrive at this end-state. In what follows, we investigate which processes are essential for explaining their origin. Then, we focus our attention on the role of supernova (SN) feedback in shaping these halos. Finally, we discuss the impact of growing hot coronae on the transition from cold filamentary to hot quasi-spherical accretion mode.

5.4.1 Growth of the diffuse medium

The conventional description of the formation of diffuse X-ray luminous halos assumes that

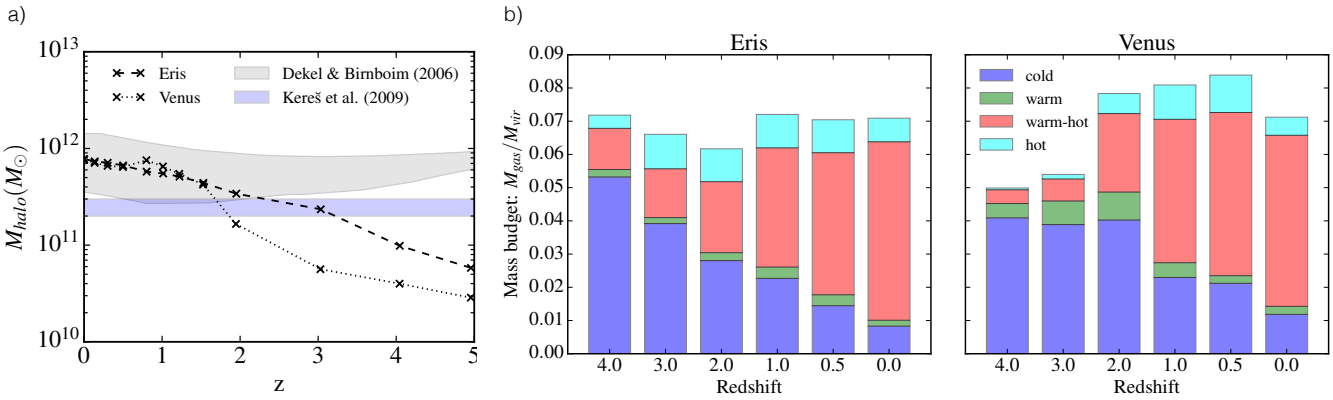

Figure 5.3: The stable shock condition vs. the formation of diffuse gas in halos. a) Halo mass as a function of redshift is compared with the critical mass for the development of a stable shock. The grey band repesents the metallicity-dependent expectation for the critical mass necessary to develop a stable inner shock at 0.1 R_{vir}(Dekel & Birnboim, 2006, metallicity range 0-0.3 $Z_\odot$). The blue band marks a mass range of halos from Kereš et al. (2009) that can sustain atmospheres of hot, virialized gas. b) Gas mass budget of the gaseous galactic halos around galaxies at various redshifts, measured within their virial radii. Cold gas: $T < 3 \times 10^4$ K; warm gas: 3×10^4K $< T < 10^5$K; warm-hot gas: $T = 10^{5-6}$K; hot gas: $T > 10^6$K.

they are generated due to the hot mode accretion, in halos which grow sufficiently in mass (i.e. beyond the critical mass threshold). Here, we test the validity of this scenario in our simulations. First, we investigate when halos of our galaxies enter the critical mass regime; then, we compare the resulting redshift with the time, during which hot diffuse atmospheres of gas begin to appear around those halos.

In the left panel (a) of Figure 5.3, we show the total halo mass of Eris and Venus as a function of redshift. The grey band indicates the metallicity-dependent lower limit for the mass of the halo, necessary to develop a stable inner shock at 0.1 R_{vir} and it covers a metallicity range of $0.03Z_{\odot}$ to $0.3Z_{\odot}$ (Dekel & Birnboim, 2006). The critical mass for the development of the stable virial shock (at R_{vir}) exceeds $10^{12}M_{\odot}$ already at $Z = 0.03Z_{\odot}$, hence would fall in this diagram above the grey band. The blue band corresponds to the mass range of $2-3\times10^{11}$ $M_{\odot}$, which was found to be the nearly constant critical mass threshold between $z = 3$ and $z = 0$ in the simulations of Kereš et al. (2009). Beyond that transition mass, simulated galaxies were able to sustain atmospheres of hot virialized gas. In the right panel (b) of Figure 5.3, we show the gas mass budget of Eris and Venus at 6 different redshifts that is normalized to the virial mass of the halo at a corresponding redshift. Each gas mass budget is divided into gas phases: cold ($T < 3 \times 10^4$ K), warm (3×10^4K $< T < 10^5$K), warm-hot gas ($T = 10^{5-6}$K) and hot ($T > 10^6$K). This plot excludes gas in the galactic disk, i.e. all gas particles with densities higher than the star formation density threshold (5 atoms/cc), in order to isolate the gaseous halo. Note that any differences in the gas fraction between the runs can be attributed to their assembly history (e.g. relatively low gas fraction before $z = 2$ in Venus is correlated with the later halo assembly). When the halo masses of Eris and Venus converge, and Venus settles down after the last major merger, final gas fractions of both runs ($z = 0$) become very similar.

Our galaxies enter the regimes for hot mode accretion at different times: Eris crosses the blue band at $z = 3$ and can develop a stable shock at 0.1 R_{vir} after $z = 2$, but never the virial shock. Venus, on the other hand, attains a halo mass that exceeds both thresholds drawn with blue and grey bands later, i.e. between $z = 2$ and $z = 1.5$. This implies that a significant fraction of diffuse gas (red and cyan bars in the panel (b) of Figure 5.3) should appear close to these redshifts. However, this is not what we observe. Although the cold gas is the most abundant gas phase until $z = 2$, both halos can sustain hot and warm-hot atmospheres earlier than that. Taking the example of Eris, already at $z = 4$, the diffuse gas

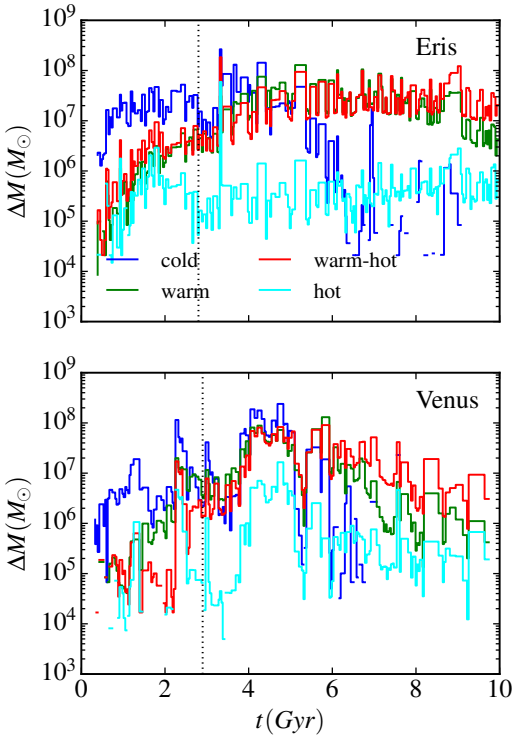

Figure 5.4: Temperature of gas particles present in a $z = 0$ hot corona at first R_{vir} crossing, showing two-stage halo gas evolution. The dotted line marks approximately the time of the equivalence of the cold and hot mode accretion ($z = 2.5$).

(warm-hot and hot combined) amounts to 40% of cold gas; at $z = 3$, to 70%. Diffuse gas appears in Venus way before the halo reaches the critical mass as well – at $z = 4$, it amounts to 12%, at $z = 3$ to 25% and at $z = 2$ to 75% of the cold gas, respectively. These results imply that hot accretion cannot be the source of diffuse halos developing at early redshifts.

Although hot gas is not the most abundant gas phase, it contributes the most to the X-ray emission and it can be observed in OVII/OVIII absorption/emission. Our diffuse halos match well these constraints, therefore we investigate under what conditions this agreement is achievable. We select particles, which are hot ($T > 10^6$ K) at $z = 0$ and at distances smaller than the virial radius, and trace their temperature and their time of accretion onto a halo. We treat a particle as accreted, if it crosses the virial radius of the halo for the first time. We show in Figure 5.4 that gas, which ends up in a hot corona at $z = 0$ (T$> 10^6$ K), does not come exclusively from late epochs. A significant fraction of gas building the present-day coronae is coming in at early times, and is cold as it passes the virial radius the first

time. The contribution to the coronae of cold-accreted gas becomes negligible after 5-6 Gyrs of evolution (after $z \sim 1.5$) in favor of the first-time warm-hot accretion. This significant mass of cold-accreted gas must then be heated to over a million degrees in order to become a part of a hot corona. In principle, stable inner shock could be responsible for shock-heating of the cold infalling gas close to the center of the halo. However, we already showed this is impossible before $z \sim 2$ (earlier on, $\mathrm{M_{halo}}$ is below the grey band in Figure 5.3). Hence, cold-accreted gas must be either shock-heated via mergers and end up in a hot state with a very long cooling time, or it must be kept hot by the energy of supernovae (or both). It could also become a part of outflows and return as second-generation hot accretion at later times. The exact cause of the generation of hot coronae is the main topic of the paper, and we focus on this problem in the next section.

We note that the epoch of equivalence of cold and warm-hot accretion in Figure 5.4, as well as the time of the extinction of the cold accretion, are similar in these simulations for two different reasons. 1) The epoch of equivalence (dotted line in Figure 5.4) occurs at approximately $z = 2.5$ in both runs, even though Venus and Eris are different in their halo mass by a factor of a few at that redshift (see Figure 5.3a). However, before $z = 2$, Venus experiences gas-rich mergers, which raise the diffuse gas fraction to the similar level as in Eris by $z = 2$ (panel b of Figure 5.3). It is likely that the shock-heating from frequent mergers and/or accompanying SN blasts raised the temperature of gas both inside and outside the halo. As a result, the warm-hot accretion becomes important before halos acquire the critical mass. 2) The second similarity – the drop-off in the mass of cold-accreted gas near $z \sim 1$ – is less surprising because the gravitational heating is expected to take over as soon as the simulations align in the $M_{halo}(z)$ space and cross the blue and grey bands (Figure 5.3a).

In the rest of this section, we study the distribution of diffuse gas and characterize its thermodynamical state as a function of time. As previously, in the following analysis we remove those gas particles, which belong to the disk, i.e. discount all gas particles with densities higher than the star formation density threshold (5 atoms/cc).

First, we present the temperature profile of the gaseous halo in Figure 5.5. The mass-weighted average temperature of gas is calculated in the radial shells around the galactic center and normalized to the virial temperature of the halo, with $\mathrm{T_{vir}} = (\mathrm{GM_{vir}}\mu\mathrm{m_p})/(2\mathrm{R_{vir}}\mathrm{k_B})$ and assuming $\mu \simeq 0.6$. Virial temperature T_{vir} of the halo is $(5.3, 7.5, 7.1, 6.8, 6.1) \times 10^5$ K for Eris and $(2.9, 2.8, 4.5, 7.4, 6.0) \times 10^5$ K for Venus at $z = (4, 3, 2, 1, 0.5)$, respectively. One can

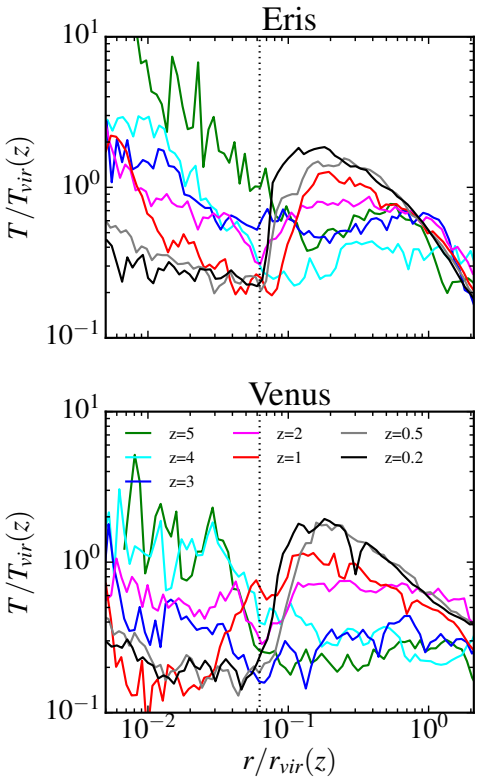

Figure 5.5: Radial distributions of gas temperature normalized to the virial temperature of the halo at a given redshift, showing the diffuse halo in formation. The vertical line marks the approximate extent of the disk at $z = 0$. Top to bottom: Eris, Venus.

distinguish two regions in these profiles that show different behavior with redshift, indicated by the black vertical line ($r/r_{vir} = 0.06$) which marks the approximate extent of the disk at $z = 0$. Left of that line, gas cools over time to a fraction of the virial temperature, and supplies fresh gas to the galactic disk. Right of that line, the temperature increases over time relatively to the virial temperature of the halo. The distribution beyond the area of the galactic disk becomes peaked after $z = 2$. The peak is localized near $0.2R_{vir}$ (40 kpc at $z = 0.2$), and attains its maximum at twice the virial temperature near the end of the calculation ($z = 0.2$, $\sim 2 \times 10^6$ K). Beyond R_{vir}, temperature fractions of T_{vir} are convergent, becoming nearly redshift-independent in Eris. The peak of the function T/T_{vir} in Figure 5.5 exposes that some heating process (or a combination of processes) is acting just above a disk, forming a hot corona.

Next, we divide the diffuse gas into hot ($> 10^6$ K) and warm-hot (10^{5-6} K) gas to

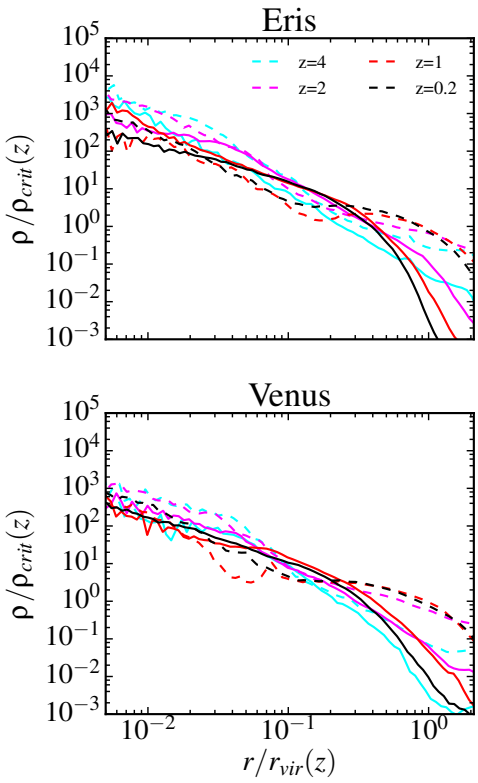

Figure 5.6: Radial density distribution of gas and its evolution with redshift. Dashed and solid lines denote the warm-hot and hot components of gas, respectively. Quantities are normalized to the critical density and the virial radius of the galaxy at a given redshift, and show the development of the onion-like structure: a corona embedded in the warm-hot soup of gas.

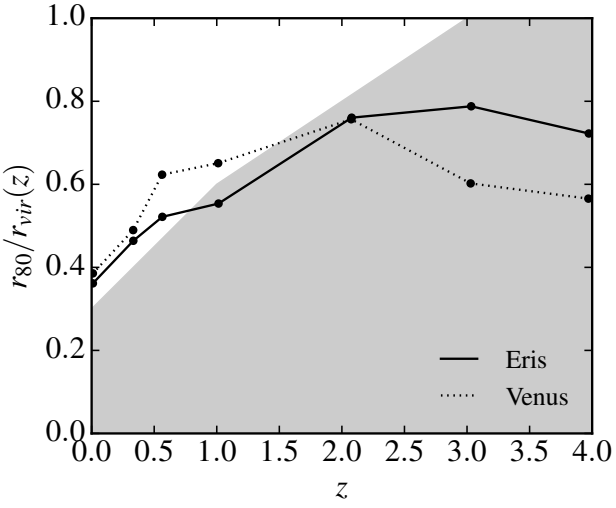

Figure 5.7: The size evolution of hot gas halo. r_{80}, defined as a radius encompassing 80% of its mass, is normalized to the virial radius (r_{vir}). Grey-shaded region indicates where cooling of hot gas is still important (i.e. $t_{cool} << t_{Hubble}$).

study their spatial distribution. In Figure 5.6, we compare their density profiles at different redshifts. At first ($z = 4$), warm-hot and hot gas in both simulations fall off monotonically with radius. After $z = 2$, however, striking differences arise: 1) the distribution of warm-hot gas has an inflection point around $0.2 - 0.3\mathrm{R_{vir}}$, preceding a local maximum beyond this radius; 2) the drop-off of the density profile of hot gas becomes increasingly steeper. The steep drop-off indicates that hot gas can be found only within a fraction of a virial radius and not beyond. Thus, after $z = 2$, a hot corona of both galaxies becomes surrounded by warm-hot medium increasing in density, which is what is seen in the end state. The envelope of warm-hot gas spreads out to a few virial radii.

We quantify the extent of hot gas as a function of time in Figure 5.7. As a proxy, we defined its extent as a radius encompassing 80% of its total mass within a virial radius (r_{80}). We find that, before the formation time of the corona (around $z = 4 - 3$), most of the hot gas spreads out to 80% of the virial radius. After $z = 2$, both hot halos are confined to 0.4 R_{vir} at $z = 0$.

The grey-shaded region in Figure 5.7 shows, approximately within which radius cooling of hot gas proceeds on a timescale that is shorter than the Hubble time. To provide this estimate, we calculated cooling time as a function of radius based on the actual radiative

cooling rates from the simulation, Λ, and the internal energy, U, according to $t_{cool} = U/\Lambda$. We verified that in both simulations the cooling time is very short near the galactic center (e.g., within 0.1 r_{vir} it drops to orders of magnitude below 1 Gyr even at $z = 1$), and monotonically increases with radius. At $z = 3$, hot gas within the virial radius cools on a less than 1 Gyr time scale. With the passage of time, cooling rate of the outer layer of the halo ($r > 0.6R_{vir}$ at $z = 1$, $r > 0.3R_{vir}$ at $z = 0$) increases to $t_{cool} >> t_{Hubble}$. Thus, a hot corona heated inside-out would partially cool radiatively and partially adiabatically as it expands, transforming into the warm-hot phase of gas, and contributing to the local density peak of warm-hot gas past the inflection point in Figure 5.6. We refer to this transformation in the next section.

5.4.2 Role of feedback and mergers

In this section we investigate what the impact of major heating mechanisms is on the build-up of the diffuse halo. In particular, we determine whether the energy injection by feedback plays a role in building up a corona. The design of the code GASOLINE allows us to disentangle the following heating mechanisms per particle: heating due to atomic/radiative processes only (rad_{heat}), supernovae thermal feedback (SN), artificial viscosity (AV), and work done by adiabatic contraction (or expansion, in which case pdV will be negative and hence contribute to adiabatic cooling). We are particularly interested in the relevance of each of these mechanisms for a build-up of two phases of gas: the warm-hot gas ($T = 10^{5-6}$K) and the hot gas ($T > 10^6$K). Hence, we measure the mass-weighted energy rates of those heating mechanisms within the virial radius per gas phase as a function of a redshift, and present them in Figure 5.8. We normalize all energy injection rates to the total heating rate $\dot{E}_{sum} = \sum_i \dot{E}_i$, where i stands for each of the processes mentioned above.

The lines in Figure 5.8 are color-coded according to the gas phase; the energy rates of warm-hot gas are denoted with red lines, and of hot gas with cyan lines. The pdV work of both phases is negative at all times, meaning that the diffuse gas is expanding, and thus adiabatically cooling. In fact, in the aftermath of a major merger at $z = 0.9$, hot gas of Venus cools adiabatically so efficiently that the net energy injection rate $\dot{\mathrm{E}}_{\mathrm{sum}}$ becomes negative (hence $\dot{\mathrm{E}}_{\mathrm{SN}}/\dot{\mathrm{E}}_{\mathrm{sum}} < 0$, $\dot{\mathrm{E}}_{\mathrm{pdV}}/\dot{\mathrm{E}}_{\mathrm{sum}} > 0$).

The heating of the warm-hot gas is dominated by supernovae across all redshifts. The second-most important heating source of that phase is artificial viscosity, with a rate that is

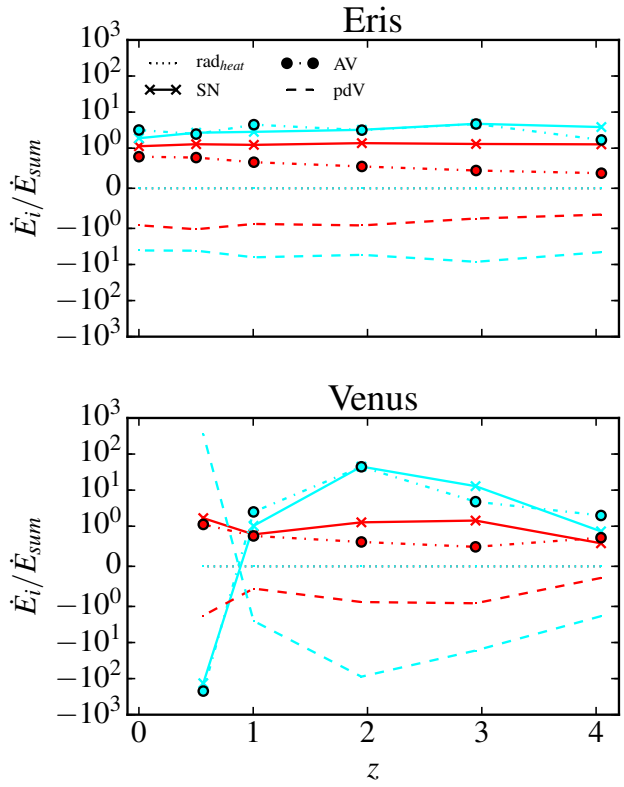

Figure 5.8: Energy injection rates for various gas phases in the region encompassed by a sphere of a virial radius around a galaxy, normalized to the total heating rate. The color coding corresponds to the warm-hot (red) and hot (cyan) gas phases. Legend: rad_{heat} – heating due to atomic/radiative processes only, SN – supernovae thermal feedback, AV – artificial viscosity, pdV – work done by/on the gas.

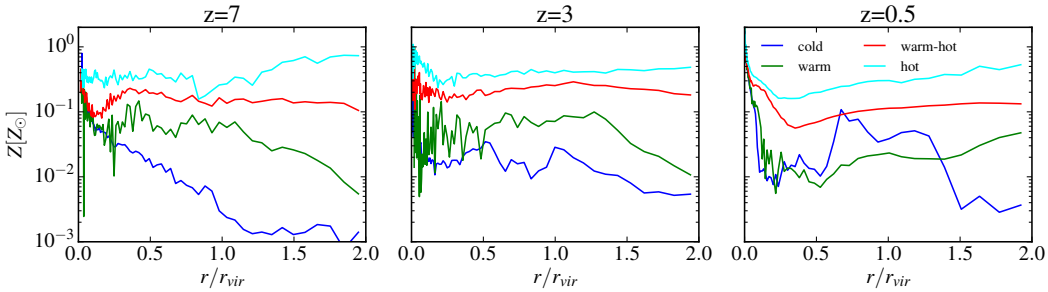

Figure 5.9: Example of radial metallicity profiles per gas phase at 3 different time steps. Case study: Eris. Profiles of Venus are very similar and show the same trend: hot gas is the most metal-enriched gas phase, and warm-hot gas is the second-most metal-enriched gas phase.

lower within a factor of two. The build-up of the hot phase, however, is aproximately equally driven by both of these heating agents, as is shown with the cyan lines. We note that, as AV is only a tracer of shocks and not the measure of shock heating in these simulations, we treat it as such. The core result of this analysis is thus that, since supernovae heating is more, or at least equally, important source of heating, it must play a major role in shaping the diffuse halos of our galaxies.

Another argument pointing towards the relevance of feedback is the high metal enrichment of the diffuse gas both as early as $z = 7$ and late as $z = 0.5$. Figure 5.9 shows radial distributions of metallicity of various phases of gas at 3 epochs: $z = 7$, $z = 3$, $z = 0.5$, assuming $Z_\odot = 0.0194$ (Anders & Grevesse, 1989). We use the results for Eris as an example of trends which are common for both simulations. As in the previous section, we are interested in the metallicity distributions in the gaseous halo only and not in the disk, therefore we discount particles above the star formation threshold. The resultant radial metallicity profiles of the halo gas show that the hot phase of gas is always the most metal-enriched. The warm-hot gas is second most metal-enriched to at least as far as 2 virial radii. Metals is our simulations come from SNI and SNII.

The fact that SN feedback has a significant impact on the warm-hot gas phase explains the puzzling feature of the warm-hot density profile, which we discussed in the previous section (Figure 5.6). The warm-hot gas envelope forms at the intersection of outflowing material and warm-hot/hot intergalactic medium (IGM) accretion. This explanation is supported by the fact that hot gas is indeed adiabatically expanding. Moreover, metal-enriched outflow-

ing warm-hot gas mixes with the hot/warm-hot IGM accretion, making it the second-most metal-enriched gas phase. This is illustrated in Figure 5.10, which summarizes the following experiment.

First, we divide a gaseous halo at $z = 0$ into three distinct regions: 1) dominated by the disk ($r_0 < 15$ kpc), 2) harboring a corona ($r_0 \in (15, 100)$ kpc), 3) encompassing the extended warm-hot reservoir $r_0 \in (100, 240)$ kpc. We measure the fractions of gas mass per gas phase in all these regions at $z = 0$ (region 1: 90%, 1%, 4%, 5%; region 2: 9%, 0%, 58%, 33%; region 3: 2%, 3%, 92%, 3%; for cold, warm, warm-hot, hot phase, respectively). Then, we select randomly 100 particles according to these weights (e.g., the central region then consists of 90 cold, 1 warm, 4 warm-hot and 5 hot particles), and color-code them according to their final temperature at $z = 0$. Next, these representative particles are traced back in time to redshifts higher than $z = 0$ and plotted on the radius-temperature ($r - T$) diagrams (a corresponding movie can be found in the supplementary material). As a result, we are able to distinguish three different patterns of accretion, and capture their variations, which are dependent on the stage of the halo evolution. We show them in Figure 5.10, where we indicate the typical trajectories of particles with black arrows. The left and right columns of Figure 5.10 are examples of the first ($z = 2.72$) and the second stages ($z = 0.54$) of accretion. We use Eris as the case study.

The central region (top panel in each column) is always dominated by the "cold flows". Even at a later stage, when gas is heated up to 10^5 K upon entering the virial radius, its temperature drops down to below 3×10^4 K while accreting. Although feedback dramatically increases the temperature of some gas particles, they manage to cool very rapidly and efficiently, hence on average they never migrate outwards.

The middle layer (second panel in each column) of a present-day gaseous halo is built by circulation flows. At first, gas enters the virial radius through cold flows, obtains SNe energy or shock-heats because of mergers, and is ejected outward, even beyond the virial radius. Then in the second stage, the trajectory of the incoming particles forks in the $r - T$ diagram: some gas enters as relatively cool particles, and some is heated. At the end, the resultant high-temperature population ($T > 10^5$ K) is formed at the intersection of freshly accreted gas (or re-accreted after the particles' turnaround), and the gas in outflows.

Similarly to the middle layer, the outmost region (third panel) is first supplied by the warm/cold inflow of gas. However, outflows powered by feedback and mergers push this

gas efficiently beyond the virial radius. Around $z = 1.5$, the inflow-to-outflow channel is overtaken by a different pathway: gas particles undergo gradual heating during and after crossing the virial radius. This is also the time when the halo of Eris exceeds the critical mass necessary to develop a stable shock at 0.1 R_{vir}. Outside the virial radius, it is common that the temperature of gas particles sharply increases with no shift in the radial location. These particles also receive no SNe energy, suggesting shock-heating as the relevant heating agent.

In what follows, we quantify the difference that the presence of SN feedback makes on the diffuse gas budget and its evolution. In order to achieve that, we perform a direct test of the impact of SN feedback on the halo; namely, we run another simulation, which is a variation of Eris but without SN feedback (herafter this run is referred to as ErisNFB). We chose $z = 4$ to be the starting redshift to compromise between the two requirements: 1) the diffuse gaseous halo should ideally be absent; 2) lack of feedback should have as little influence on the assembly history as possible. Although without feedback one cannot produce realistic galaxies due to overcooling, the benefit of this test lies in being able to isolate the effect of SN heating from gravitational heating by accretion shocks and merger-induced shocks.

Figure 5.11 illustrates a violent heating episode, which is an example of a series of such events occuring repeatedly over the lifetime of a galaxy, and compares its magnitude between a run with feedback (top row) and without (bottom row). The temperature maps in Figure 5.11 capture the evolution of the "blast" over 0.3 Gyr in the environment of Eris; however, similar occurrences are also common in Venus. In both Eris and ErisNFB, the general sequence is similar: at $z = 3.42$, the gaseous halo consists of two blobs of warm-hot gas that are separated by inflows of cold/warm gas. The central concentration of over one million-degree gas grows significantly into a nearly spherical region, attaining an extent of approximately 20 kpc by $z = 3.26$. Afterwards, the inner part of the halo expands and cools. Early "blasts" in Eris are easy to detect in the temperature maps, and their timing is coincidental with the peaks in the star formation rate (see Figure 5.15 in the Appendix).

The second row of Figure 5.11 shows that hot gas can also be generated much earlier than what is expected based on conventional cold/hot mode threshold even in the absence of feedback. Already at $z = 3.42$, gas in the center of ErisNFB exceeds the temperature threshold of 10^6 K. Here, powerful outflows are generated during a major merger, seen in the map as conical warm-hot and hot patches, which reach distances exceeding the virial

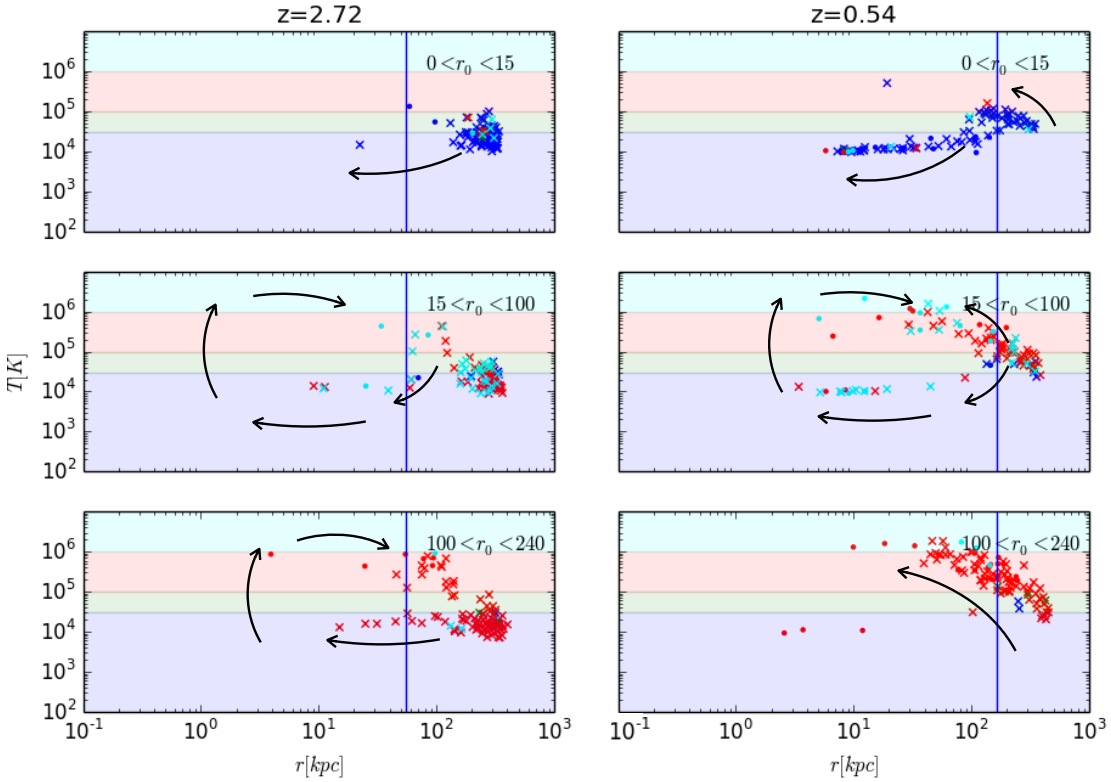

Figure 5.10: Radius-temperature diagram for a selection of particles from $z = 0$ traced back in time to $z = 2.72$ (left column) and $z = 0.54$ (right column). Each row distinguishes between particles which build a different region of a gaseous halo at $z = 0$ (top to bottom: $r_0 < 15$ pkpc, $r_0 \in (15, 100)$ pkpc, $r_0 \in (100, 240)$ kpc). Background of each panel is color-coded according to the temperature range of each phase of gas (hot, warm-hot, warm, cold) and particle color-coding represents their end state at $z = 0$. Arrows mark the typical trajectories of particles in these two accretion epochs. Individual particles are marked with a dot or a cross, depending on whether they receive feedback energy or not (dot = yes). Vertical line marks the virial radius. For a detailed description of the experiment, including the selection method, see the text. Case study: Eris.

radius of a galaxy. The metal-poor outflows generated without feedback are triggered by shock-heating associated with mergers. However, those outflows are much less powerful than those combined with SN feedback, as they have a limited range compared with the heat maps of Eris at $z = 2.99$. This result indicates that SN feedback has a significant impact on the gas distribution of a gaseous halo even as early as $z = 3.5$.

In Figure 5.12, we show the radial density profiles of the two gas phases: warm-hot (top) and hot (bottom) for the run with SN feedback (solid lines) and without (dashed lines) at $z = 3$ and $z = 2$. The presence of feedback makes a major difference in the center of a diffuse halo ($\sim 0.1\mathrm{R_{vir}}$), in particular in the warm-hot phase. The density of the warm-hot gas in that region is about 2 orders of magnitude higher if SN feedback is switched on. The discrepancy between the density of hot gas in Eris and ErisNFB is smaller but also significant, namely hot gas is about 5 times denser in Eris than in ErisNFB. Beyond $\sim 0.1\mathrm{R_{vir}}$, density profiles of both gas phases tend to converge (warm-hot at $\sim \mathrm{R_{vir}}$ and hot at $\sim 0.4\mathrm{R_{vir}}$). Overall, a run with supernovae feedback switched on produces more hot gas. For example, already at $z = 3$ we find 1.3 times more hot gas in Eris than in ErisNFB within the virial radius, and by $z = 1$ that ratio increases to 1.5. In total, introducing feedback increased the abundance of $T > 10^5$ K gas by a factor of 1.3-1.4 between $z = 3 - 1$ within the virial radius.

Halos are not only structurally different but also imply a different X-ray evolution with redshift. We compute X-ray luminosities at $z = 3, 2, 1$ in the 0.5-2 keV band for Eris and ErisNFB using the same procedures as described in the beginning of the section 5.4. We find that X-ray luminosities are higher when feedback is included, namely 3.40×10^{41}, 8.9×10^{40}, 5.9×10^{40} erg/s as opposed to 2.4×10^{38}, 1.1×10^{38}, 1.3×10^{37} erg/s at $z = 3, 2, 1$ respectively. Lack of feedback thus likely violates the X-ray luminosity constraints on the present-day halos, suggesting that SN feedback is not only essential to obtain realistic disk galaxies but also their diffuse halos.

5.4.3 Coronae and cold flows

As discussed in the introduction, Milky Way-like galaxies occupy a mass scale, at which galaxies are expected to acquire gas initially via the "cold mode" and then, via the "hot mode". Two effects are at play in building up the diffuse halo and driving the transition from cold filamentary accretion to hot spherical accretion: 1) halos grow sufficiently in

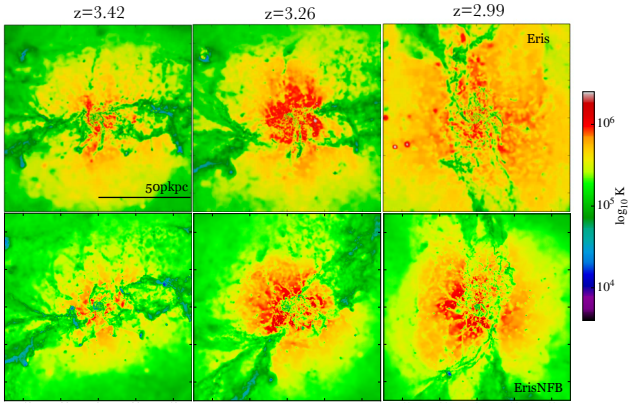

Figure 5.11: Temperature maps of a gaseous halo at 3 timesteps, illustrating a typical "blast" in action in case with feedback (Eris) and without (ErisNFB). Red regions (hot gas, first and second subplots) cool down and expand adiabatically over time (orange-yellow regions in the last subplot). The width of each square is 100 pkpc.

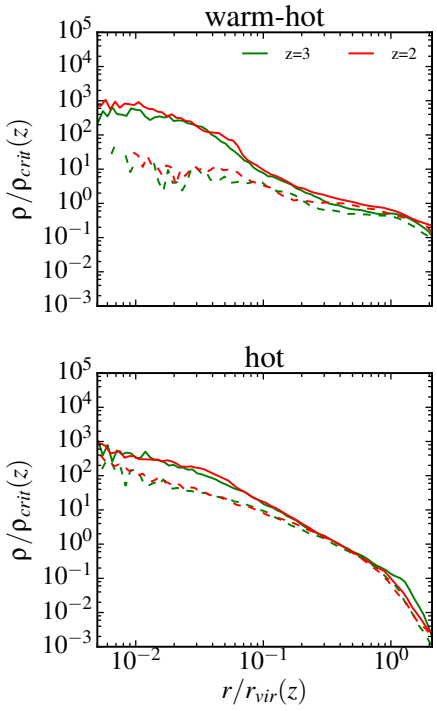

Figure 5.12: Density profiles of warm-hot (top) and hot (bottom) with SN feedback (solid lines) and without (dashed lines). The normalization of the axes are critical density of the universe and virial radii of halos at the corresponding redshifts.

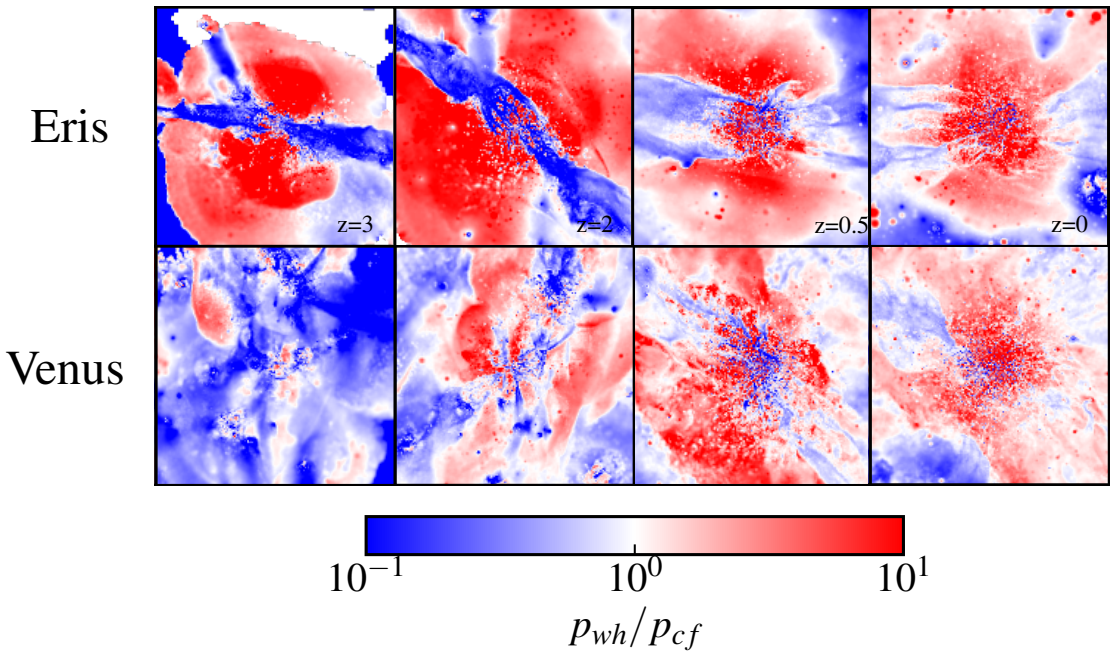

Figure 5.13: Evolutionary sequences of the total pressure fractions of the "warm-hot accretion" (a sum of ram and thermal pressure) to the total pressure of the "cold flow". A width of each square is 1 pMpc.

mass beyond a threshold, after which a stable shock develops, thereafter heated accretion occurs; 2) initially compact filaments thicken over time; as they reach a cross section that is comparable with that of the halos, they lose the ability to penetrate gaseous halos down to a galaxy. This work adds a new factor to this framework, namely it emphasizes the importance of the processes heating the gas inside-out. Energy injections from mergers and supernovae explosions lead to an earlier formation of the diffuse halos than what was previously established, and in halos of mass much lower than the critical mass of $\sim 10^{12} M_{\odot}$.

The remaining question is whether the presence of those early diffuse halos affects the galaxy-filaments connection and thus the accretion mode switch, which we touch upon in this section.

Early on, hot and warm-hot gas phases are outflowing, which is a consequence of their origin. An early gaseous halo thus can be thought of as hosting two fronts on a collisional trajectory: cold dense filamentary flows with a negative radial velocity, and an expanding diffuse halo with a positive radial velocity. Naturally, those two fronts will exchange momentum and energy upon a collision. In Figure 5.13, we show that the inside-out growing

corona shields a galaxy from the cold flows. Following the literature, we define the *cold flow* to be the gas at temperatures below 10^5 K that is moving towards the galactic center; gas at $T > 10^5$ K is assigned to the diffuse halo. Ram pressure, p_{ram}, is defined as $p_{ram} = \frac{1}{2}\rho v_r^2$, and thermal pressure, p_{th}, is given by $p_{th} = \frac{kT\rho}{\mu m_p}$. Figure 5.13 illustrates how the ratio of the total pressure (sum of thermal and ram pressure) of the diffuse halo and the cold flows (p_{wh}/p_{cf}) is reversed in the immediate vicinity of the galaxy over time.

Initially, cold flows penetrate the galactic halo and easily reach the disk. The filamentary structure of Eris at $z = 3$ consists of branches, which clearly mark preferential directions of accretion, whereas Venus is bombarded by such flows from nearly all directions, although after a few Gyrs, Venus exhibits the same pattern as Eris. Namely, the energy released from the center of the halo gradually generates a thermally pressurized central bubble, which expands outward and engulfs the filaments. A cold filament in Eris at $z = 2$ behaves analogically to the river mouth that widens upon encountering an obstacle (hot corona), and tries to flow through it and around it via paths of least resistence. These accretion channels become thinner over time (examples of such narrow streams are shown at $z = 0.5$, $z = 0$ in Figure 5.13). Note the nearly spherically symmetric distribution of the ratio p_{wh}/p_{cf} after $z = 2$, when the outflow-induced corona driven by both mergers and feedback outbalances the pressure of the filaments. Additionally, filaments are weakened in structure by the ram pressure stripping that acts with a magnitude of velocity that is a sum of both fronts (e.g. before $z = 2$, $|\frac{v_{wh}}{v_{cf}}| \lesssim 10$).

We showed in section 3.2 that inclusion of SN feedback increases the density of diffuse gas near the galaxy by up to two orders of magnitude. Hereafter, we describe qualitatively the consequences of efficient SN feedback for the galaxy-cold flow connection. Figure 5.14 presents the temperature maps of gas in a face-on view on the central galaxy. The width of each square is 500 comoving Mpc. Top row shows a few early snapshots of the Eris simulation and is set against the snapshots of ErisNFB in the bottom row in order to show the structural differences in the halo at the absence of feedback.

Looking first at Eris results (top row), focused streams of intergalactic material initially easily reach and feed the galactic disk of Eris (a, top row of Fig. 5.14). Prominent outflows isolate the central galaxy from the filamentary network for extended periods of time (b, the pushback region is marked by two dashed lines). After some time, filaments continue loading cold gas, however, via scattered channels (c). Their structure is also notably weak-

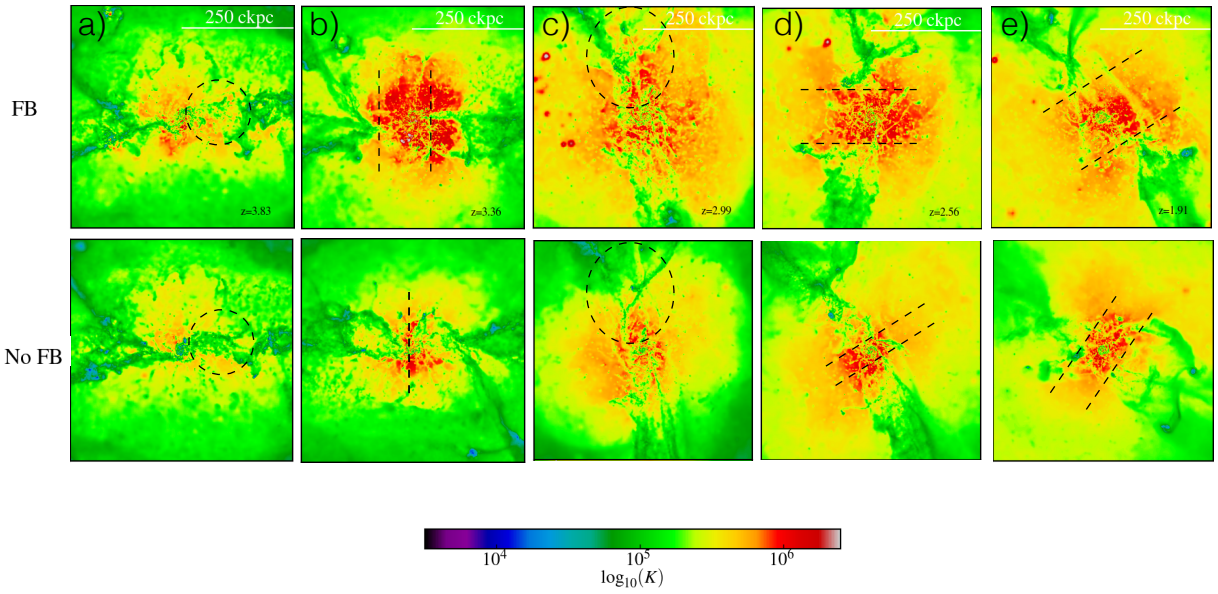

Figure 5.14: Temperature maps of Eris (top row) and ErisNFB (bottom row) between $z \sim 4$ and $z \sim 2$ comparing the change in the location (lines, columns b, d and e) and structure (circles, columns a and c) of the filaments with and without feedback.

ened already at $z = 2.99$. The growth of hot coronal gas (i.e. of the thermal and ram pressure front) gradually pushes filaments back and away from a galaxy (d,e). Compared with Eris, the diffuse gas of ErisNFB develops a visibly weaker pressure front (bottom row of Fig. 5.14). Feedback-supported pressure front forces filaments, even if temporarily, to much larger distances (columns b, d, e; compare top and bottom of Fig. 5.14). Feedback also heats up and strips filaments already as early as $z = 3.83$ (columns a,c circles). Thus, SN feedback not only charges coronae with additional hot material but also affects the intersection corona-filament in a way that efficiently isolates a galaxy from the cold inflow. We expect this mechanism to regulate star formation and make it less efficient (either temporarily or permanently). The exact details of this mechanism, however, will be studied in the future work.

5.5 Conclusions

In this paper, we use a set of 3 hydrodynamical zoom-in simulations of Milky Way-sized halos ($M_{halo} \lesssim 10^{12} M_{\odot}$) in order to investigate the formation of X-ray luminous gas around these galaxies. Two of our runs are variations of the default Eris simulation: 1) the SN feedback mechanisms are switched off, which allows for quantifying the effect of SN feedback on the halo evolution (ErisNFB); 2) the initial conditions are changed, providing a case study of active merger history (Venus).

In Paper I of this series, we studied present-day diffuse halos of simulated galaxies and matched them against available constraints on the Milky Way. This paper (Paper II) investigates how these diffuse halos form. In particular, we focus on two gas phases: hot ($T > 10^6$ K) and warm-hot ($T = 10^{5-6}$ K) that have different characteristics. For example, we showed in Paper I that hot coronae are localized within 0.4 R_{vir} of their halos, while the warm-hot gas stretches to beyond 2-3R_{vir}. We explain this configuration in physical terms.

1. We investigated when halos of our realistic galaxies (Eris, Venus) enter the critical mass regime for the development of the stable shock at 0.1 and 1.0 R_{vir}. We compared the resulting redshift with the time, during which hot diffuse atmospheres of gas begin to appear around those halos. We found that diffuse halos can develop earlier than is expected in the standard picture (White & Frenk, 1991; Dekel & Birnboim, 2006), even as early as $z = 4 - 3$, but also in low-mass halos. The most striking example is

Venus, as its halo mass, for instance at $z = 3$, is about an order of magnitude below the critical mass threshold of few times $10^{11} M_{\odot}$. This opens a question of how galaxies build hot reservoirs of gas via alternative channels. Two other heating mechanisms we put forward are merger-induced shocks and SN heating.

2. Hot coronae are built by gas crossing R_{vir} across all redshifts. Most of this accretion is cold at high redshifts when it passes the virial radius the first time. This cold-accreted gas must then be heated to over a million degrees in order to become a part of the hot corona. The halo mass is too small to sustain a stable shock at $0.1R_{vir}$, therefore we conclude that cold-accreted gas must be shock-heated via mergers and the energy of supernovae. It could then remain in the diffuse state with a long cooling time, or be ejected outside the virial radius and return as the second-generation hot accretion at later times.

3. The onion-like structure (a hot corona embedded in a warm-hot envelope of gas) develops after $z = 2$. The warm-hot envelope forms at the intersection of two fronts: 1) the expanding and adiabatically cooling hot gas; 2) the IGM accretion of warm-hot gas, which becomes possible as soon as a halo mass crosses the critical mass for the development of a stable shock. Since hot gas is converted into the warm-hot phase during the adiabatic expansion, the density profile of hot gas begins to drop off sharply. Simultaneously, the density of warm-hot gas develops an inflection point around $0.2 - 0.3R_{vir}$ and a local maximum (a conglomerate of the two fronts). The size of an adiabatically cooling hot corona decreases with time to $0.4R_{vir}$ at $z = 0$.

4. A direct measurement of energy injection rates reveals that the heating of the warm-hot gas is dominated by supernovae across all redshifts, while the second-most important heating source is artificial viscosity (lower within a factor of two). The energy rates for hot gas show that SN are at least as important as other heating mechanisms generating shocks (artificial viscosity). Hot gas is also most metal-enriched at all evolutionary stages ($z = 7, 3, 0.5$).

In order to determine whether coronae can form in the absence of feedback, we ran a high-resolution cosmological simulation without SNe feedback (ErisNFB) from $z = 4$. Switching off feedback allows for isolating SN heating from gravitational heating by accretion shocks and merger-induced shocks. Below are our major findings.

1. The metal-poor hot outflows can be generated without feedback, and they are likely triggered by mergers. However, outflows are much more powerful and have a greater range when SN feedback is present, even as early as $z = 3.5$. This is why diffuse halos can form earlier and in considerably lower mass halos than expected. Feedback and no-feedback runs should align as halos reach a critical mass for the development of a stable shock.

2. Already at $z = 3$ we find 1.3 times more hot gas within the virial radius in the simulation with feedback compared to the same run without feedback, and by $z = 1$ that ratio increases to 1.5. Introducing feedback also increased the abundance of $T > 10^5$ K gas by a factor of 1.3-1.4 between $z = 3 - 1$ and within the virial radius. The presence of feedback makes a major difference in the center of a diffuse halo (within $\sim 0.1\mathrm{R_{vir}}$); the density of the warm-hot gas in that region is about 2 orders of magnitude higher if SN feedback is switched on. Hot gas in the center of Eris is about 5 times denser than in ErisNFB.

3. The X-ray luminosity of our gaseous halos without SN feedback is lower than with feedback by two orders of magnitude. Eris with SN feedback attains 3.40×10^{41}, 8.9×10^{40}, 5.9×10^{40} erg/s at $z = 3, 2, 1$ respectively. Our results imply that low-luminosity spirals with M_* and M_{halo} similar to the progenitors of Eris and Venus at $z > 2$, and with similar star formation rates, should be surrounded by the extended X-ray emitting gas.

In this work we also emphasized on the connection between coronae and the accretion bimodality of Milky Way–like galaxies. We investigate what happens at the intersection of growing hot gas concentrations and cold filaments, and the role of feedback therein. Our findings are summarized in the points below.

1. The growth of a corona cuts a galaxy off the filamentary network. It happens due to change in the pressure balance around the galaxy – an outflow-induced corona (from both mergers and feedback) outbalances the pressure of the filaments. The pressure bubble propelled by galactic outflows pushes the filaments (cold flows) away, and at the same time ram pressure strips the filaments with the relative velocity of the expanding bubble and the inflow. Thus, the growth of a corona might be responsible for the

accretion mode switch. The switch happens gradually – a galaxy accretes cold IGM material via narrow channels, these channels are however weakened and progressively stripped as they pass through a high-pressure medium.

2. We showed that SN feedback not only charges coronae with additional hot material but also affects the intersection corona-filament in a way that efficiently isolates a galaxy from the cold inflow. This has also consequences for the large-scale gas supply, and may contribute to quenching of galaxies.

The most important finding of this work is that *a galactic corona is not a consequence of hot spherical accretion onto a galaxy.* The corona is a consequence of mergers-induced shock heating and feedback, grows inside-out, is X-ray luminous and detaches a galaxy from the filamentary network.

All this is quite different from the mainstream picture, in which hot mode accretion is a consequence of thermalisation of kinetic energy derived from gravity. It is possible that at larger mass scales, gravitational compression and stable shocks play a more important role than supernovae feedback or mergers. However, the picture drawn in this paper is more relevant for typical spiral galaxies with the virial mass near $10^{12} M_{\odot}$. Future X-ray surveys sensitive to such mass scale will test this model.

This study leaves a few open questions. For example, it is still unclear how the hot IGM accretion is affected by the presence of SN feedback at the virial and galactic radii. As we are expecting outflows to leave the halo at early redshifts, it is possible that the recurrent accretion (circulation flows) is additionally contributing to the hot accretion as early as $z = 3 - 4$. The recurrent accretion could be metal-enriched by feedback or also metal-poor, if it originates in major mergers. Perhaps both factors would alter the time of the accretion mode switch. These topics have yet to be investigated in the future work.

5.6 The case of strong SN feedback

In this Appendix, we discuss what happens in the models, in which SN feedback is excessively boosted to quench star formation at early times. First, we describe the parameters of an additional simulation, a variation of Eris with strong supernovae feedback. Then, we discuss its outcome in the context of several observables and main results of this paper.

5.6.1 Simulation with strong feedback: description

Eris2k (hereafter E2k, described in more detail in Sokołowska et al. 2016), stems from the same initial conditions as Eris but differs in the choice of some sub-grid parameters. Its parameters were tuned in order to yield a stronger effect of supernova (SN) feedback to lower star formation rates at high redshift. E2k also has a richer inventory of physical processes, including not only metal-line cooling but also a sub-grid turbulent diffusion prescription for both metals and thermal energy which allows mixing to be captured in SPH (Shen et al., 2010). Some of the important simulation parameters of E2k and other runs of this paper, including the choice of the UV background and aspects of the sub-grid physics, are listed in Table 5.1 and discussed below.

In contrast to Eris and Venus, the metal-line cooling in E2k is computed at all temperatures, employing tabulated rates computed with the code CLOUDY (Ferland et al., 1998), under the assumption that metals are in ionization equilibrium (Shen et al., 2010). We also use the updated cosmic ionizing background (Haardt & Madau, 2012). The recipes for star formation and SN feedback are the same in all the runs and are described in Stinson et al. (2006) but there are a few differences in associated parameters. Namely, the star formation threshold $n_{\rm SF}$ of E2k is set to 100 atom cm^{-3}; the maximum temperature of a particle allowed for star formation is $T_{\rm max} = 3 \times 10^4$ K; supernova efficiency parameter is increased to $\epsilon_{\rm SN} = 1.0$; and the initial mass function is updated to (Kroupa, 2001) (see Table 5.1).

The strength of feedback depends on the number of SNe produced, which is in turn governed by the IMF and, locally, by the star formation density threshold. An updated IMF yields about a factor of 2.8 more SNe at equivalent star formation rate than Eris/Venus. Furthermore, as explained in detail in Guedes et al. (2011) and Mayer (2012), the local star formation rate, and thus the local effect of SNe, can be boosted significantly by raising the star formation density threshold as the interstellar medium is allowed to become more inhomogeneous, an effect that saturates only at very high resolution and density thresholds, well above those resolved in cosmological simulations (Hopkins et al., 2012). This implies that in E2k, heating by SN feedback is boosted both globally and locally. We recall that E2k is a run that follows an extensive study of sub-grid parameters by running many different simulations with the same Eris-type initial conditions in order to determine the combination of parameters that yields realistic stellar masses in accordance with abundance matching at both high and low redshift, these being shown in Table 5.1.

Run	UVB	IMF	$n_{\rm SF}$	$\epsilon_{\rm SN}$	MC	IC
Eris	HM96	K93	5	0.8	low-T	Q
E2k	HM12	K01	100	1.0	all-T	Q
Venus	HM96	K93	5	0.8	low-T	A

Table 5.1: Input parameters of the runs. Notation: UVB – UV background (HM96: Haardt & Madau 1996, HM12: Haardt & Madau 2012), IMF – initial mass function (K93: Kroupa et al. 1993, K01: Kroupa 2001), $n_{\rm SF}$ – star formation density threshold in cm^{-3}, $\epsilon_{\rm SN}$ – SN efficiency parameter in 10^{51} erg, MC – metal cooling, and IC – initial conditions (Q: quiet merger history, A: active merger history).

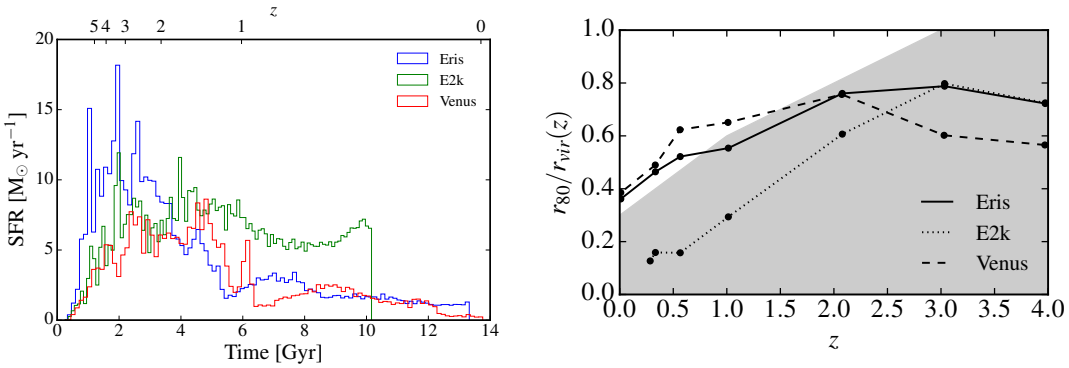

Figure 5.15: Left. The comparison of star formation histories of Eris, E2k and Venus. Note that the run E2k was stopped after 10 Gyrs of evolution. Right. The radius of a hot corona encompassing 80% of its mass as a function of redshift.

5.6.2 Impact of strong feedback on our main results

Star formation history. In the left panel of Figure 5.15, we compare star formation histories of Eris, Venus and E2k. Eris and Venus differ at early times (Eris has much higher star formation rate until $z = 2$; the star formation of Venus is delayed with respect to Eris because of its late assembly history). The assembly history of E2k is the same as Eris, however, the differences lie in the subgrid physics, which is discussed above. Feedback was boosted in E2k in order to quench star formation at early times, and hence be closer to the abundance matching. This works well until approximately 8 Gyrs, after which the model breaks down. The material, which was ejected via strong winds, turns around and feeds the star formation, which begins to increase to several times the star formation rate of the Milky Way.

Radius of the corona $r80$**.** In the right panel of Figure 5.15, we compare the radius encompassing 80% of a hot corona between Eris, Venus and E2k. After $z = 3$, r_{80} of E2k begins to shrink to less than a half of the size of the remainder. At the same time, we showed in Paper I that the present-day hot mass budget of both E2k amounts to 1% M_{vir}, similarly to other runs in this study. This means that a corona of E2k is much more compact.

X-ray luminosity. The X–ray luminosity of diffuse gas in the 0.5-2 keV band is a mismatch with the known constraints on the Milky Way discussed in this paper, namely it is about 100 times higher than that ($L_X \sim 10^{42}$erg/s). In Paper I, we linked this result with a too-strong feedback.

Summary. Early ejective feedback quenches star formation until late epochs, when the gas turns around and begins to feed star formation at a high level. This affects not only the observables for the galactic disk, but also the diffuse gaseous halo, which turns out to be too metal-enriched, and produces too many X-rays due to the compactness of its hot halo.

Chapter 6

Conclusion

This thesis presents advancements in the understanding of the dynamics and thermodynamics of baryons in the Milky Way-like halos. We use high-resolution cosmological zoom-in simulations of galaxy formation as our main tool. Those zoom-ins are: Eris (our default model with a quiescent merger history), ErisBH (the default model with AGN feedback), Eris2k (the model with overall strong SN feedback), ErisLE (the default model with low star formation efficiency), ErisNFB (the default model with no feedback energy), and Venus (the default model with an active merger history). Below we list our major findings.

- Galaxies and their halos grow approximately homologously with each other. Owing to high resolution of the runs, we were able to credibly decompose galaxies into their bulges and disks. Unless a system undergoes multiple major mergers, the retention factors of extracted disks are always close to unity.

- We showed evolutionary tracks of galaxies and their stellar/gaseous components in the $\log j_*$–$\log M_*$ diagram. Galaxies in the low-density environments evolve on straight lines past major mergers.

- The state-of-the-art models of galaxy formation produce not only realistic galaxies but also realistic present-day gaseous galactic halos, which was determined based on a number of Milky Way and extragalactic observables.

- Concealing of the ubiquitous warm–hot baryons, along with the ejection of just $20-30\%$ of the diffuse gas out of the potential wells by supernova–driven outflows, can solve the "missing baryon problem".

- The diffuse gas around the Milky Way has an onion-like structure, i.e. consists of the quasi-spherical X-ray luminous corona surrounded by an envelope of an order of magnitude cooler gas.

- A typical galactic corona is not a consequence of hot spherical accretion onto a galaxy but of mergers-induced shock heating and supernova feedback. Coronae grow inside-out and detach galaxies from the filamentary network as they outbalance the pressure of cold flows.

- Supernova feedback impacts the galaxy-cold flows connection, which has also consequences for the large-scale gas supply and may contribute to galaxy quenching.

Chapter 7

Limitations and prospects

Thermodynamics of baryons. Our studies of zoom-in simulations is limited to one type of subgrid recipe for feedback only, i.e. the blastwave feedback (Stinson et al., 2006). One of the possible extensions of this work could include a comparison with a simulation employing the superbubble feedback model (Keller et al., 2014), which is known to heat up gas to higher temperatures and alter the thermodynamics of clumpy high-redshift galaxies (Mayer et al., 2016). However, we do not expect a change in feedback to invalidate our main conclusions on the formation of hot X-ray coronae, since we have shown that most of the early-stage hot gas comes from the merger-induced shock heating (i.e. is the result of the dynamical effects). Future work on the topic of cold mode-hot mode accretion could include quantifying the contribution of the recurrent accretion (circulation flows) to the hot accretion at high redshifts.

Another caveat of this study is the lack of statistical power because our data comprised a small sample of zoom-in simulations. The preliminary extension of this work is presented in the Appendix, where we test the robustness of our findings of chapter 4 on a larger sample of simulated galaxies performed with a different simulation technique (EAGLE). Additionally, we use a number of realizations of this large scale cosmological simulation with varied feedback subrid physics (both supernova and AGN feedback) in order to quantify the incurring changes in the properties of hot gas ($> 10^6$ K). The ErisBH simulation (Bellovary et al., 2010; Bonoli et al., 2016) with a different implementation of AGN feedback from Booth & Schaye (2011) will be added to the sample in the future work.

In addition, the measurement of the X-ray luminosity of hot Milky Way-sized coronae

in different feedback realizations of EAGLE would provide yet another constraint on that model, in particular whether AGN feedback is too effective at expelling gas compared with more baryon-rich zoom-ins presented in chapter 4 (which do satisfy this constraint).

Dynamics of baryons. The shortcoming of our work is that our sample of zoom-in galaxies is scarce. However, our simulations are complementary to large scale simulations capable of conducting statystical analysis, since we can trace the evolution of angular momentum of individual halos in high resolution. In particular, determining what effect various physical processes have on the specific angular momentum is a formidable challange, and could be tackled with particle tracing. Ideas for the extension of this work are mentioned below.

- The disk and spheroid could form through different physical processes. Can we capture the differences triggered by these processes in the cross-correlation functions of various properties for these components?

- Mergers shaped the angular momentum distribution of baryons in a different way than the filamentary/spherical accretion. Can we see any correlations showing that, e.g. upon flagging stellar particles by their origin (smooth accretion/part of another halo)?

- Individual particles are noisy in terms of their properties. We can select big samples of particles, average over their properties and cross-correlate that. In particular, fountain-not fountain particles should show different signatures (and a different history of specific angular momentum).

- What shapes the angular momentum of gas before it becomes a star? Is their specific angular momentum stable after the star formation (in other words, is the spin of galaxies set by the gas physics) or are there 2 modes of the spin evolution: gaseous and stellar?

- Is stronger feedback leaving a different imprint on the specific angular momentum of gas than the weaker feedback? How is the evolution of specific angular momentum of different stellar/gaseous components changed when feedback is absent?

- Is the growth of the corona (aka the push-out of the filaments from the galaxy) leaving a specific signature in specific angular momentum of the accreted mass (future stars)?

- Sales et al. (2012) showed that the spheroid-dominated galaxies have misaligned spins as a function of radius, in contrast to the disk-dominated ones, at the time of the collapse. What causes this misalignment and how does it lead to the destruction of the disks?

One could thus expand the work presented in this thesis on multiple fronts. The angular momentum of spiral galaxies and their environment is currently a vibrant field as of yet full of open interesting questions.

Appendix A

OVII absorption in EAGLE cosmological simulations

Sokolowska, A., Rahmati, A. Mayer, L. et al., in prep.

A.1 Introduction

Galaxies are surrounded by extended coronae of hot gas, which constitute vast reservoirs for gas accretion onto galaxies (Fraternali et al., 2013). These coronae are a part of multi-phase gaseous galactic haloes, which extend to the virial radii of their halos (Putman et al., 2012). The existence of hot coronae was first debated by Spitzer (1956) who argued that ubiquitous HI clouds must be confined by an external medium. Since then, substantial evidence has been accumulated in favor of such medium. For example, gas depletion in dwarfs of the Milky Way is well-understood in terms of ram-pressure stripping of the hot medium (Nichols & Bland-Hawthorn, 2011; Gatto et al., 2013). Direct detection of hot gas around massive disk galaxies provides tangible proof of their existence (e.g. Anderson et al., 2013; Bogdán et al., 2013). The best evidence for the hot coronae comes from bright AGN sight lines with detections of OVII and OVIII in absorption (Miller & Bregman, 2014), and from high-resolution X-ray spectra of the soft X-ray background (Snowden et al., 1997; Henley & Shelton, 2012).

The sensitivity of current X-ray spectroscopy limits the detections to a handful of sight lines. Observational studies that use OVII absorption lines as tracers of the hot gaseous halo of the Milky Way have gained more constraining power in recent years due to the increase in

the number of those sight lines (~ 30, see Miller & Bregman, 2014, and references therein). Through studies of the distribution of such absorbers, these observations provide additional tests of the commonly used recipes for the galaxy formation and evolution. In turn, realistic hydrodynamical simulations can be used to improve the treatment of caveats associated with the observational methods.

Recent zoom–in cosmological simulations of Milky Way–type galaxies, i.e., Eris (Guedes et al., 2011) and Eris2k (Sokołowska et al., 2017), show good agreement with those observations and suggest that a large fraction of baryons in the halo of the Milky Way–sized galaxies is in the warm–hot (10^{5-6} K) and hot phase (10^6 K) (Sokołowska et al., 2016, and references therein). The robustness of those findings, however, needs to be tested, using a larger sample of simulated galaxies and different simulation techniques. To do this, we use the EAGLE suite of cosmological hydrodynamic simulations (Schaye et al., 2015) to study the distribution of highly ionized oxygen absorbers (OVII) around Milky Way–type galaxies. Additionally, we test if the density of the diffuse coronae of Milky Way-sized galaxies in EAGLE fulfills constraints following from ram pressure stripping of the Milky Way dwarf galaxies. Finally, we asses the impact of the type and presence of various implementations of feedback on our findings.

A.2 Simulations

We use the set of simulations called Evolution and Assembly of GaLaxies and their Environments (EAGLE, Schaye et al., 2015; Crain et al., 2015). The EAGLE simulations were run with a modified version of the smoothed particle hydrodynamics (SPH) code GADGET3 (Springel, 2005; Schaller et al., 2015), with cosmological parameters from Planck Collaboration et al. (2014), i.e. $[\Omega_m, \Omega_b, \Omega_\Lambda, \sigma_8, n_s, h] = [0.307, 0.04825, 0.693, 0.8288, 0.9611, 0.6777]$. The details of the subgrid physics are explained in Schaye et al. (2015). Below, we summarize their most important aspects, and briefly describe their variations, which are used in this work and covered more in detail by Crain et al. (2015).

A.2.1 Subgrid recipes

Gas particles are stochastically converted into stellar particles according to the pressure-dependent prescription of Schaye & Dalla Vecchia (2008) and a metallicity-dependent density

threshold (Schaye, 2004). The resolution of the simulations is insufficient to model the cold phase of gas, therefore a global temperature floor, corresponding to the equation of state $p \propto \rho^{4/3}$ normalized to 8000 K at a density of $n_H = 0.1cm^{-3}$, has been introduced. The temperature of star-forming gas is then set to $T = 10^4$ K for the computation of the ionization balance.

Stellar particles release mass and metals in stellar winds and supernova explosions (Wiersma et al., 2009). Each stellar particle represents a population of stars, whose distribution is described by the initial mass function (Chabrier, 2003). The abundances of 11 elements (i.e. H, He, C, N, O, Ne, Mg, Si, Fe, Ca and Si) are used to calculate the equilibrium rates of radiative cooling and heating in the presence of cosmic microwave background, UV (Haardt & Madau, 2001) and X-ray (Wiersma et al., 2009) background radiation. Energy feedback from supernovae and active galactic nuclei (AGN) is distributed among the neighbours of newly formed stellar and black hole (BH) particles (Dalla Vecchia & Schaye, 2012). Black holes grow through mergers and gas accretion (see for more details Springel, 2005; Schaye et al., 2015; Rosas-Guevara et al., 2015). In general, the subgrid feedback parameters have been calibrated to reproduce the observed present-day galaxy stellar mass function, the sizes of galaxies, and the relation between stellar mass and black hole mass. Haloes and galaxies are identified from the simulation using the Friends-of-Friends and SUBFIND algorithms (Dolag et al., 2009).

A.2.2 Reference runs and their variations

Ref100, Ref50, Ref25. EAGLE reference simulations (L100N1504, L050N0752, L025N0376). Periodic boxes have sizes of 100, 50 and 25 cMpc, and contain N=1504^3, 752^3, 376^3 particles (dark matter and additionally equal numbers of baryons), respectively. The resolution of the simulations is the same, with particle masses of $m_{dm} = 9.7 \times 10^6 M_\odot$ for dark matter, and $m_b = 1.8 \times 10^6 M_\odot$, for baryons. These simulations are described in Schaye et al. (2015).

noAGN. EAGLE simulation with reference stellar feedback but no AGN feedback. Other parameters are the same as for the reference box of the size 50 cMpc. For more details, see Rahmati et al. (2016).

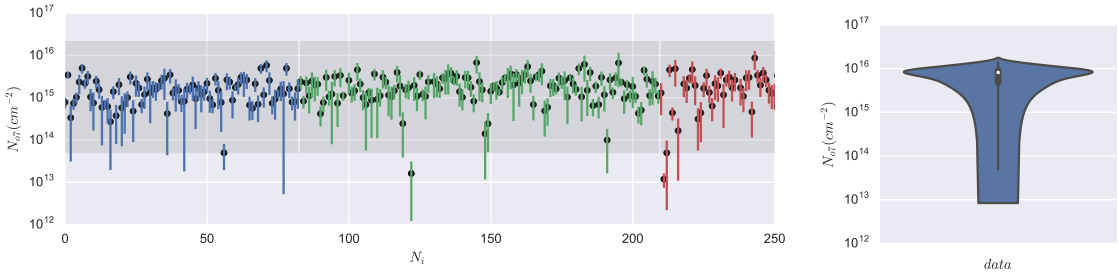

Figure A.1: Column densities of OVII absorbers in real and mock observations. Left. Column densities of individual halos of EAGLE. Each measurement was integrated out to 240 kpc (approximately the virial radius). The error bars of each data point indicate the mean absolute deviation of 20 sightlines. Three samples in different mass ranges are color-coded, namely $6.16 - 6.45 \times 10^{11} M_{\odot}$ (blue); $9.55 - 10.47 \times 10^{11} M_{\odot}$ (green); $1.00 - 1.65 \times 10^{12} M_{\odot}$ (red). Right. The distribution of the dataset used in this work as a benchmark (Miller & Bregman, 2013). For more details, see the text.

AGNdT9. An alternative model of the reference EAGLE simulation. The temperature of SPH neighbours in an AGN feedback event is increased by $\Delta T = 10^9$ K as opposed to $\Delta T = 10^{8.5}$ K chosen for the reference runs. This parameter change was found to more accurately reproduce the observed gas fractions and X-ray luminosities of galaxy groups (Schaye et al., 2015).

StrongSN, WeakSN. EAGLE simulations with the reference AGN feedback but strong/weak stellar feedback. The physical efficiency of feedback is controlled by a parameter representing the fixed quantity of feedback energy per stellar mass formed. StrongSN and WeakSN use twice and half the value chosen for the reference simulation, respectively. Other parameters of the simulations are the same as for the reference box of size 25 cMpc. These simulations are described in greater detail in Crain et al. (2015).

A.3 Results

In the course of this work, we are interested in galaxies which can be classified as close Milky Way analogues. We thus define such objects as those whose total mass is similar to the halo mass expected for the Milky Way ($\simeq 10^{12} M_{\odot}$). The total mass comprising all dark matter and baryons is enclosed within the radius that marks the distance from the center of a galactic potential to the point at which the density of matter drops below 200 times the

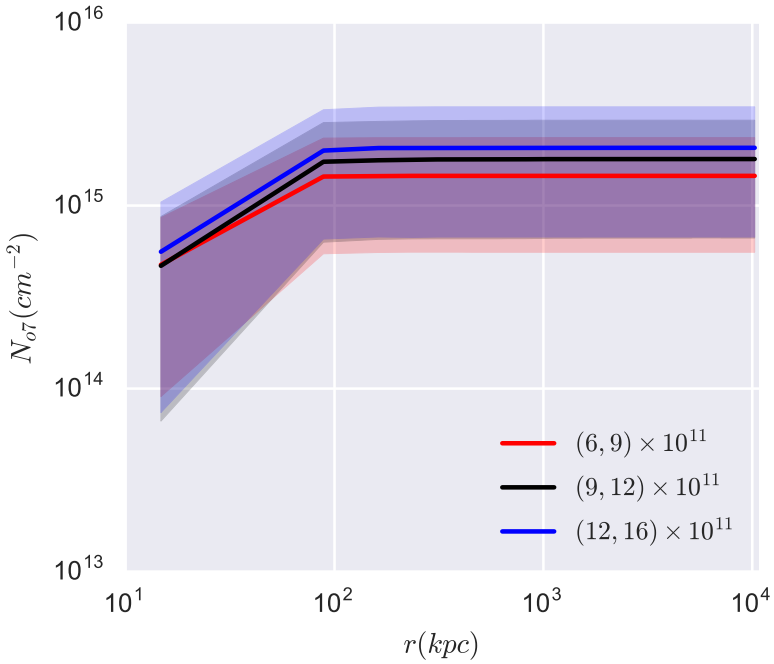

Figure A.2: The cumulative column density of OVII absorbers integrated out to the given radius. Each line represents the mean of the population falling into different mass ranges. The shaded regions indicate the mean absolute deviation of the sample.

critical density of the Universe.

In this section, we first calculate column densities of OVII absorbers in the Ref100 box and study their distribution. Then, we construct density profiles of coronae in the Ref50 and noAGN simulations to show the change in the results triggered by the presence of AGN feedback, and match them against constraints on the Milky Way halo. Finally, we compare hot gas properties in general of Ref50, noAGN and AGNdT9 (stronger AGN feedback), as well as StrongSN and WeakSN (strong vs. weak supernova feedback), to quantify the change in these properties with the varied feedback parameters.

A.3.1 Mock observations of OVII

Miller & Bregman (2013); Miller & Bregman (2014) studied all-sky catalog of OVII and OVIII emission in combination with OVII absorption measurements to determine halo electron density under a few assumptions, namely on the spherical symmetry, isothermal gas distribution and collisional ionization equilibrium. Here, we choose to compare our simulations directly with the column density of OVII absorbers. The advantage of this approach lies in reducing the assumptions of a dataset used in this work as a benchmark, thereby allowing us to test the consistency of EAGLE gaseous halos with the observational data. Hence, in what follows, we calculate column densities of OVII absorbers for the 100 cMpc reference box (Ref100) and for a sub-sample of halos of mass close to the Milky Way's mass ($6 \times 10^{11} M_{\odot}$ to $\sim 2 \times 10^{12} M_{\odot}$). The method is described below.

Dataset (benchmark). We use 29 absorption-line measurements of Miller & Bregman (2013) given in their Table 1. We choose the column density values resulting from a conversion assuming an optically thin medium. Three of the data points have negative values, therefore we remove them from the dataset.

Method (mock data). Our sample of galaxies from the 100 cMpc box comprises over 250 objects falling into the range of $\sim 6 \times 10^{11}$–2×10^{12} $M_{\odot}$. The box is divided into thin vertical slabs, each going through the individual halos. We measure column densities for each halo from a perspective of an observer situated on the annulus of 8 kpc from the center (the equivalent of the solar annulus). Column densities are measured in increments in both z directions, i.e. above and below the plane perpendicular to the vertical slabs containing the

center of a halo. The size of one incremental cell is 15 ckpc. The total number of sight lines per halo is 20 (10 above the plane, 10 below the plane). Note this approach does not enforce that measurements are done from the plane of the galaxy, as galaxies are randomly oriented in the box. Each sight line may thus cross the disk or be measured from a perspective of an observer situated way above the disk. A combination of multiple halos thus probes sufficiently the parameter space of possible inclinations of a sight line with respect to the galactic disk.

Results. The left panel of Figure A.1 shows our measurements of column densities of OVII absorbers in individual halos. Each data point represents a median result for 20 sight lines, and each error bar marks the median absolute deviation, a robust version of the standard deviation, defined as the median of $|N_{o7} - median(N_{o7})|$, where N_{o7} are the column density measurements. The grey band spans the range between the minimum and the maximum values of the observed dataset shown in the right panel of Figure A.1. The data points are color-coded according to the mass range of the sample, namely blue: $6.2 - 6.5 \times 10^{11} M_{\odot}$; green: $9.5 - 10.5 \times 10^{11} M_{\odot}$; red: $1.00 - 1.65 \times 10^{12} M_{\odot}$. These representative samples allow us to probe changes of the column density with increasing mass.

In the right panel of Figure A.1 we show the violin plot of the benchmark dataset (Miller & Bregman, 2013) with the kernel density distribution on each side. The white dot marks the median of the data, and the box around it indicates interquartile ranges. Black vertical line corresponds to the 95% confidence interval. Probablity density of the data peaks near 10^{16} cm^{-2}, indicating the most likely value of column density of OVII absorbers in the Milky Way.

All measurements presented in Figure A.1, except for two outliers, have column densities in the observational range (within the minimum and the maximum of observed values). Individual halos tend to have column densities of order $\sim 10^{15}$ cm^{-2}. The average column density of intermediate-mass halos (green) is slightly higher than low-mass halos (blue, high-mass halos should be hotter). The scatter is the biggest in the most massive halos (red), which could be the manifestation of a greater number of mergers. Compared with the dataset, which shows that the most probable value of the column density of OVII for the Galaxy is near 10^{16} cm^{-2}, column densities of simulated halos are lower by a factor of a few.

Figure A.2 shows the cumulative column densities integrated out to different radii in

three different mass bins: 6-9, 9-12 and 12-16 $\times 10^{11} M_{\odot}$. In all three populations, most of the OVII absorbers are located within 100 kpc from the galactic center. Moreover, there is a statistically significant trend of higher column density of OVII with higher mass. If the simulation Ref100 was a benchmark, one could argue this indicates that Milky Way is a high-mass halo (higher than $1.6 \times 10^{12} M_{\odot}$), as the constraint following from Milky Way observations can be fulfilled only by higher-mass halos. In practice, however, the mass of OVII (and thus the column) may be sensitive to the feedback prescription. We address this problem later in the paper.

A.3.2 Probing diffuse halos

Recent zoom-in cosmological simulations of Milky Way-sized galaxies suggest that the large fraction of baryons resides in the diffuse halos of galaxies (Sokołowska et al., 2016, hereafter S16, and references therein). EAGLE simulations are performed with a different code and different prescriptions for star formation, feedback, and cooling of gas. We do not attempt to compare the different codes directly, as this itself deserves an extensive study. However, we note that if these fundamentally different models yield similar answers to questions posed in this paper, it would considerably strengthen the robustness of our findings.

In what follows, we analyse the baryonic mass budget of a large sample of galaxies, and compute gaseous halo density profiles, limiting the discussion to two scientific questions, whether or not: 1) diffuse reservoirs of EAGLE Milky Way-sized halos are hot and baryon-rich; 2) diffuse halos of EAGLE galaxies have the right density to ram pressure strip Milky Way satellites. In the recent studies, modeling ram pressure stripping of Milky Way satellites provided additional constraints on the circumgalactic medium (CGM) surrounding our Galaxy at large distances. This comparison is thus complementary to the previous analysis of OVII absorbers.

Method. We use two variations of EAGLE simulations in this comparison: the reference run, Ref50, and the run with no AGN feedback (noAGN). The choice of the latter one in this comparison is motivated by the fact that Eris simulations from S16 do not include AGN feedback. We comment on the implications of inclusion/exclusion of that feedback component later in this section. 50 cMpc boxes are expected to have 2^3 times less objects in the same mass range as the 100 cMpc box, therefore we extend the previous mass range

to $3 \times 10^{11} - 3 \times 10^{12} M_{\odot}$ in order to include more objects, and hence gain greater statistical power. We expect density to be sensitive to the virial mass, therefore we probe halos in 6 mass bins. Median values of each sample are: 0.39, 0.68, 1.2, 1.7, 2.3, 2.7 $\times 10^{12} M_{\odot}$. We calculate number density profiles of gas, n_{cor}, assuming mean molecular weight of $\mu = 0.6$. We also investigate mass budget for gas phases identified based on the temperature of the particles: warm and cold ($T < 10^5$), warm–hot ($T = 10^{5-6}$) and hot ($T > 10^6 K$).

Data. Gatto et al. (2013) obtained upper and lower limits on the number density of the Milky Way gaseous halo under the assumption that Milky Way satellites, Sextans and Carina, were ram-pressure stripped of their gas. Salem et al. (2015) modelled the evolution of Large Magellanic Cloud under the same assumption but neglected the tidal interactions between LMC and SMC. Although tidal stripping must play a dominant role in shaping the gaseous Magellanic System and its inclusion would change the resulting constraint on the number density of the Milky Way gas, we show it for a comparison.

Results. We show the coronal number densities of halos in Figure A.3 and set them against three data points (Sextans, Carina and LMC). Unless in reality the CGM density profile exhibits a local dip around 50 kpc, the data points of Salem et al. (2015) and Gatto et al. (2013) are rather inconsistent with each other, although their location suggests that Milky Way corona should attain the density of order $10^{-4} cm^{-3}$ at about 50-80 kpc. What is clear, nevertheless, is that both the intermediate-mass halos of EAGLE and Eris/E2k simulations fall closer to the results of Gatto et al. (2013) than the recent results concerning the LMC of Salem et al. (2015). Additionally, both runs with and without AGN feedback obtain sensible coronal densities, and thus can be a subject to ram pressure stripping of dwarfs.

The presence of AGN feedback makes a major difference in the inner 2 kpc on all mass scales, and it removes an order of magnitude of gas mass in this region. Profiles without AGN feedback are more dissimilar between different halo masses out to 200 kpc. At the radii relevant for the ram pressure stripping, if the AGN feedback is present, halos of masses $10^{12} M_{\odot}$ and above fulfill the constraint following from Sextans and Carina. If the AGN feedback is absent, that range goes down to $7 \times 10^{11} - 2 \times 10^{12} M_{\odot}$, meaning that halos with masses above $2 \times 10^{12} M_{\odot}$ would violate those constraints. Moreover, Eris/E2k are more consistent with the same-mass sample of noAGN run than Ref50 at the radii of efficient

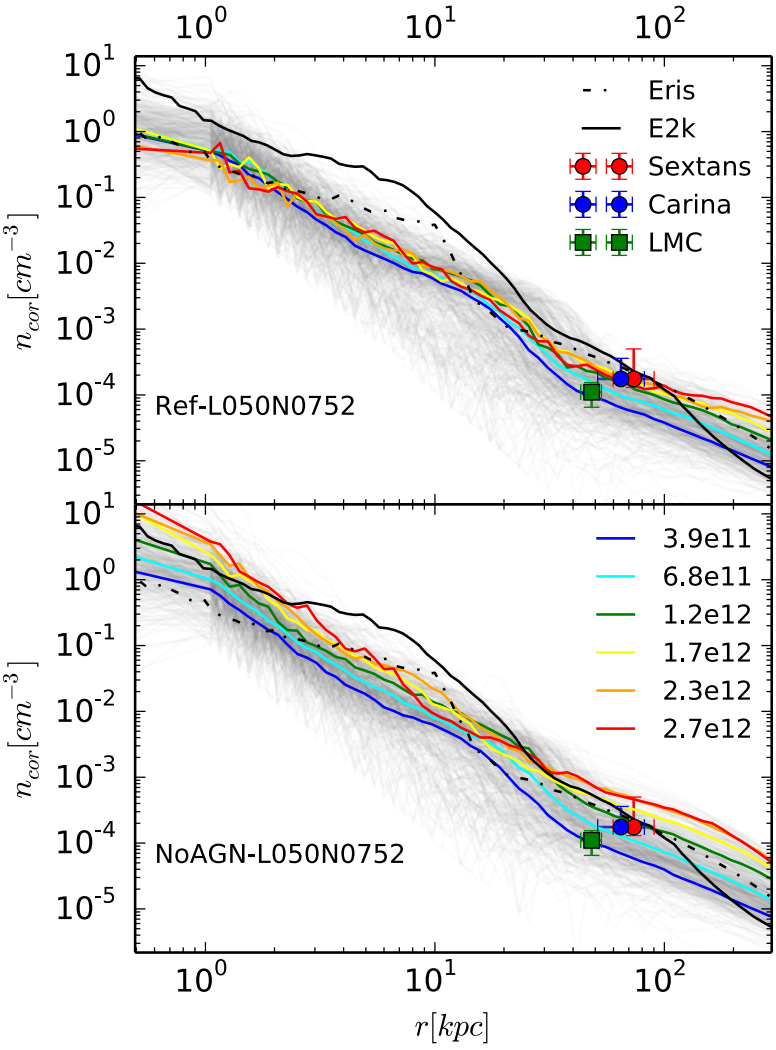

Figure A.3: Number density profiles of EAGLE halos in different mass bins vs. expected number density of the radii of efficient ram pressure stripping. Top: the reference run. Bottom: the run without AGN feedback. Grey lines represent the entire population of MW-sized halos (the total of 468 halos). Black solid and dashed lines show density profiles of zoom-in simulations E2k and Eris from S16, respectively.

ram-pressure stripping.

In Table A.1, we show the mean total stellar and gas mass of halos within their r_{200}. We also decompose gaseous halos into warm and cold ($T < 10^5$), warm–hot ($T = 10^{5-6}$) and hot ($T > 10^6 K$) components, since we are interested in identifying the most relevant gas component in these galaxies. To capture the statistically significant trends with increasing mass, we also divide the sample into six smaller mass subgroups indicated in Table A.1.

The results show that the more massive the halo, the more hot X-ray emitting gas it harbours (both with and without AGN feedback), and the more stellar mass it produces, within the boundaries of our sample (i.e. halo masses of $0.3 - 3 \times 10^{12} M_\odot$). The warm-hot gas, on the other hand, grows with the halo mass until the halo mass of $2.5 \times 10^{12} M_\odot$ ($2 \times 10^{12} M_\odot$ without AGN feedback), and then decreases. The presence of AGN feedback also modifies the cold gas - halo mass function, which increases up to the inflection point of $2.5 \times 10^{12} M_\odot$.

In the range of $0.5 - 10 \times 10^{11} M_\odot$, the hot gas mass fraction of the virial mass is of order 1%, which is in agreement with what was found in S16. In their zoom-in simulations, the present-day gaseous halos were composed of mostly the warm-hot gas ($\sim 80\%$ of gas). However, that is not the case in the EAGLE simulations. The warm-hot gas mass fraction of all gas attains at most $\sim 50\%$, both with and without AGN feedback, and we find two times more hot gas in EAGLE at the corresponding mass scale, which can be attributed to the different treatment of feedback. Namely, the feedback in EAGLE (SN + AGN) heats up the gas to higher temperatures than the blastwave feedback of S16 (well above 10^6 K). As a result, hotter gas not only cools on longer time scales but is also more pressurized, enabling a greater number of particles to escape the halo. The baryon fractions in EAGLE are lower than in zoom-ins of S16 by a factor of 2 at the corresponding mass scale (with and without AGN feedback). The baryon fraction without AGN feedback is much higher, particularly above $\sim 10^{12} M_\odot$ (note also that the stellar mass is higher too, as AGN activity inhibits star formation). The presence of AGN feedback keeps the baryon fraction at the high-mass end at about 40% of the cosmic fraction.

Nevertheless, the numbers confirm that the warm–hot gas – the low–density, diluted medium – is the most significant gas component of all, as long as we consider halos below 2×10^{12} $M_\odot$. Hot gas dominates above this mass scale. We note that EAGLE sample in the same mass range as Eris/E2k has on average the same amount of cold-warm gas, which is

sample (10^{12})	$\bar{m}_h(M_\odot)$ (10^{10})	$\bar{m}_{wh}(M_\odot)$ (10^{10})	$\bar{m}_{cw}(M_\odot)$ (10^{10})	$\bar{m}_*(M_\odot)$ (10^{10})	f_b
AGN					
$(0.3-0.5)$	0.06	0.60	0.65	0.61	0.045 (29%)
$(0.5-1.0)$	0.38	1.64	1.19	1.41	0.054 (34%)
$(1.0-1.5)$	1.73	3.89	1.99	2.58	0.058 (37%)
$(1.5-2.0)$	4.81	5.89	1.86	3.84	0.061 (39%)
$(2.0-2.5)$	9.09	7.75	2.34	4.95	0.061 (39%)
$(2.5-3.0)$	10.9	5.51	2.24	5.62	0.067 (43%)
noAGN					
$(0.3-0.5)$	0.06	0.52	0.63	0.66	0.046 (29%)
$(0.5-1.0)$	0.28	1.17	0.95	1.68	0.067 (44%)
$(1.0-1.5)$	1.13	2.01	1.32	3.63	0.091 (58%)
$(1.5-2.0)$	2.53	2.81	1.38	6.15	0.104 (66%)
$(2.0-2.5)$	5.16	2.30	1.48	7.39	0.116 (74%)
$(2.5-3.0)$	8.88	2.25	1.57	8.77	0.121 (77%)
Eris	0.63	3.02	1.20	3.41	71%
E2k	0.69	2.43	1.22	3.38	67%

Table A.1: The mass budget of the warm–hot, warm–cold and hot gas phases, and the baryonic budget of a fiducial galaxy constructed as an object of mean properties of the subsample in a mass bin. Notation: $\bar{m}_h$ – mean total mass of the hot gas; $\bar{m}_{wh}$ – mean total mass of the warm–hot gas; $\bar{m}_{wc}$ – mean total mass of the warm–cold gas; $\bar{m}_*$ – mean total stellar mass; f_b – the mean baryonic fraction of the subsample. The mean masses of the halos were computed within their r_{200}.

within the COS-Halos range (the study of the circumgalactic medium of external galaxies, Werk et al., 2014) but closer to its lower limit.

A.3.3 Feedback variations

The reference runs (Ref100, Ref50) have been chosen in this study as the basis for the comparison with the two major constraints on the diffuse gaseous halos around Milky Way-sized galaxies (OVII absorbers, ram pressure stripping of Milky Way satellites). In this section, we quantify how sensitive the results presented in this work are to the details of the feedback subgrid physics. We use 25 Mpc and 50 Mpc (Ref25, Ref50) boxes as standards, with which we conduct the comparisons. Ref25 has the same population of galaxies as StrongSN and WeakSN variations, whereas the population of Ref50 is a match for the run without AGN feedback (noAGN) and the run with boosted temperature of the AGN output

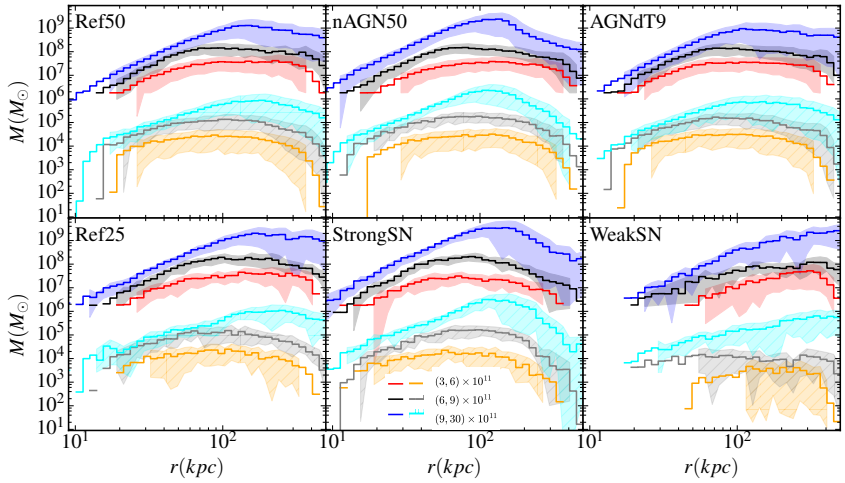

Figure A.4: The mass distribution of hot gas ($T > 10^6$ K) and OVII mass in 6 different realizations of EAGLE simulations. Each step function is color-coded with mass (low-mass, red and orange; intermediate-mass: black and grey; high-mass, blue and cyan; for hot gas and OVII, respectively). The distributions are the products of the mean values of all measurements in the individual halos falling into a given mass range. The shaded regions indicate the median absolute deviation.

(AGNdT9).

In Figure A.4, we show the mean radial mass distributions of hot gas (3 top lines) and OVII gas (3 bottom lines) for 3 samples of galaxies in different mass bins (i.e. $3-6, 6-9, 9-30 \times 10^{11} M_\odot$). Each line represents the average over all halos in different halo mass bins ($3-6, 6-9, 9-30 \times 10^{11} M_\odot$ shown as red, black and blue lines, respectively). OVII traces nearly perfectly the distribution of hot gas. For the high-mass galaxies, the distributions are peaked between 100-200 kpc. Thus, hot gas and OVII absorbers are mostly abundant at those radii. This applies to the reference runs with AGN feedback (Ref50, Ref25), StrongSN, AGNdT9, and noAGN as well. In the sample of lower-mass galaxies, the peak is less pronounced and the distributions appear smoother. WeakSN exhibits no peak at higher masses but a monotonically increasing distribution. StrongSN run generates the most hot gas of all (and OVII absorbers) and has the highest peak of all the realizations.

Figure A.5 shows the mass-weighted temperature radial distributions of hot gas (solid lines) and of the OVII-absorbing gas (dashed lines). In general, OVII tends to be born in the low-temperature hot gas (below 2×10^6 K). Hot gas with no AGN feedback, similarly to the

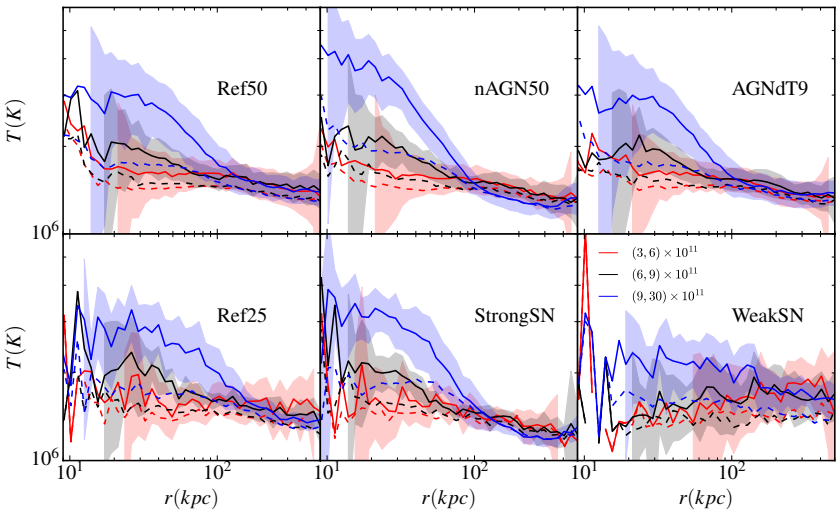

Figure A.5: The temperature distributions of hot gas ($T > 10^6$ K, solid lines) and OVII absorbers (dashed lines) mass in 6 different realizations of EAGLE simulations. The color-coding is consistent with the previous figures.

StrongSN case, attains the highest central temperature of all the realizations, which exceeds 4×10^6 K. All temperature profiles change a slope near 100 kpc and converge, thus the mass dependence is revealed only inner to that radius, and so is the subgrid scheme dependence. Outside 100 kpc, AGNdT9, Ref50, Ref25, noAGN or StrongSN runs show little difference. WeakSN is an exception, and exhibits the lowest temperatures inner to 100kpc and a larger scatter outside 100 kpc.

The radial density profiles (Figure A.6) and radial metallicity profiles (Figure A.7) are plotted according to the same scheme. We find that the densities of OVII and hot gas trace each other very well. As expected, high-mass galaxies have also higher densities of hot gas. The densities of hot gas particles are very similar between different runs. At radii greater than 100 kpc, the hot gas of high-mass galaxies of noAGN and StrongSN runs are much denser than the remainder. The hot gas of WeakSN is the thinnest of all and has the largest scatter. In terms of metallicities, OVII is born preferably in the high-metallicity gas; for the radii smaller than 100 kpc, the typical metallicity is in the range of $0.4-1Z_\odot$; for radii greater than 100 kpc, it is typically $0.4 - 0.6Z_\odot$. Outside the radius of 100 kpc, there is no clear trend in metallicity with mass as in case of the density profiles (the low and intermediate-mass galaxies have similar metallicities, while the high-mass galaxies are low on metals).

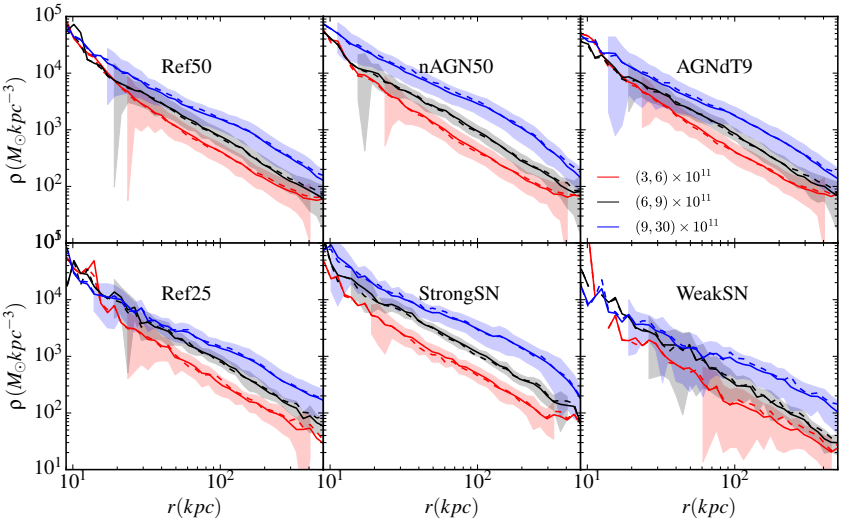

Figure A.6: The density distributions of hot gas ($T > 10^6$ K, solid lines) and OVII absorbers (dashed lines) mass in 6 different realizations of EAGLE simulations. The color-coding is consistent with the previous figures.

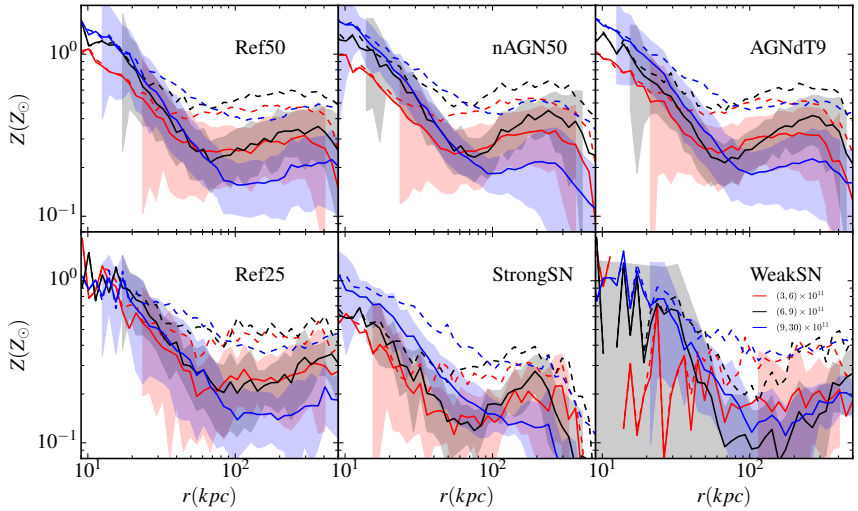

Figure A.7: Metallicity distribution of hot gas ($T > 10^6$ K) and OVII mass in 6 different realizations of EAGLE simulations. The color-coding is consistent with the previous figures.

Inside that radius, however, the more massive the galaxy, the more metals it harbours. In StrongSN, hot gas is less metal-rich than the reference runs, and OVII is born in more metal-poor gas. Galaxies in WeakSN, similarly to other comparisons, have the largest scatter also in the metallicity distributions, which makes the profiles noisy. The metallicity profiles of noAGN, Ref50, AGNdT9 share a degree of similarity. We note that no significant differences arise in the properties of the populations of Ref50 and Ref25 throughout the study.

A.4 Conclusion

In this paper, we study the column densities of OVII absorbers and the coronal densities of Milky Way-sized halos in the sample of EAGLE galaxies. We test the robustness of another study on the gaseous galactic halos, which reports a baryon-rich envelope of low-density warm-hot and hot gas surrounding these galaxies, and a good agreement with OVII absorption-inferred electron density profiles (S16). We also compare coronal number density profiles with the predictions for the Milky Way density derived from modelling of the ram pressure stripping of observed dwarf galaxies (Sextans, Carina, LMC).

Our major conclusions are summarized below.

1. All measurements of the column density of OVII in the reference feedback model Ref100 are within the observational range. We tested this on the sample of over 250 Milky Way-sized objects. Compared with the most probable value for the Milky Way, however, the measurements in EAGLE sample are lower by a factor of a few.

2. The distribution of OVII absorbers shows that most of them are located within radial 100 kpc.

3. The halos more massive than $10^{12} M_{\odot}$ fulfill the constraint following from the ram pressure stripping of Sextans and Carina. If the AGN feedback is absent, that range is $7 - 20 \times 10^{11} M_{\odot}$, which is more consistent with the zoom-in simulations of S16.

4. Contrary to that study, the EAGLE galaxies with and without AGN are surrounded by warm-hot envelopes of gas comprising at most 50%, not 80%, of the gas reservoir. This is due to the feedback implementation which produces hotter gas and expels a large fraction of baryons outside the virial radius. The reservoir of hot gas ($> 10^6$ K)

is twice as massive in these simulations as in S16. Nevertheless, warm-hot gas is the most abundant gas phase if halo is less massive than $2 \times 10^{12} M_{\odot}$. The contribution of the cold-warm gas to the baryon budget is consistent (but closer to the lower limit of) the results found by COS-Halos.

5. Baryon fractions in the presence of AGN feedback are levelled down to ∼40% of the cosmic fraction. Without AGN feedback, galaxies of $M_{halo} \simeq 3 \times 10^{12} M_{\odot}$ contain up to 77% of the cosmic baryon fraction.

We also studied variations of AGN feedback (noAGN, AGNdT9) and SN feedback (StrongSN, WeakSN). Here are our main conclusions.

1. The WeakSN simulation differs the most from all studied realizations in the context of the halo gas properties (i.e. the temperature, density and metallicity of hot gas). As reported in Crain et al. (2015), the weak supernova feedback in these galaxies led to the overgrowth of black holes, enhancing the AGN feedback on low mass scales. We verified that baryon fractions of its objects are extremely low compared with other simulations, also at the high-mass end of our sample.

2. Changes in the feedback type (AGN on/off) or strength (WeakSN, StrongSN) impacts primarily the radial temperature distributions of hot gas of high-mass galaxies. As expected, OVII can be found in the gas at temperatures of $\sim 2 \times 10^6$ K in all the feedback realizations.

3. We found that for most of the studied feedback realizations, gas properties (density, temperature, metallicity) are not dramatically affected by the feedback changes (with the exception of WeakSN), hence we expect our results for the OVII columns to be relatively robust.

Bibliography

Abadi, M. G., Navarro, J. F., Steinmetz, M., & Eke, V. R. 2003, ApJ, 591, 499

Abel, T., Anninos, P., Zhang, Y., & Norman, M. L. 1997, NewAstron., 2, 181

Agertz, O., & Kravtsov, A. V. 2015, ApJ, 804, 18

—. 2016, ApJ, 824, 79

Agertz, O., Teyssier, R., & Moore, B. 2011, MNRAS, 410, 1391

Anders, E., & Grevesse, N. 1989, gca, 53, 197

Anderson, M. E., & Bregman, J. N. 2010, ApJ, 714, 320

Anderson, M. E., & Bregman, J. N. 2011, ApJ, 737, 22

Anderson, M. E., Bregman, J. N., & Dai, X. 2013, ApJ, 762, 106

Babul, A., Balogh, M. L., Lewis, G. F., & Poole, G. B. 2002, MNRAS, 330, 329

Behroozi, P. S., Wechsler, R. H., Lu, Y., et al. 2014, ApJ, 787, 156

Bellovary, J. M., Governato, F., Quinn, T. R., et al. 2010, ApJl, 721, L148

Benson, A. J., Bower, R. G., Frenk, C. S., et al. 2003, ApJ, 599, 38

Bertschinger, E. 2001, ApJs, 137, 1

Binney, J. 1977, ApJ, 215, 483

Binney, J., Gerhard, O., & Silk, J. 2001, MNRAS, 321, 471

Bird, J. C., Kazantzidis, S., Weinberg, D. H., et al. 2013, ApJ, 773, 19

Birnboim, Y., & Dekel, A. 2003, MNRAS, 345, 349

Bogdán, Á., Forman, W. R., Kraft, R. P., & Jones, C. 2013, ApJ, 772, 98

Bogdan, A., Forman, W. R., Vogelsberger, M., et al. 2013, ApJ, 772, 97

Bogdan, A., Vogelsberger, M., Kraft, R. P., et al. 2015, ApJ, 804, 72

Bondi, H. 1952, MNRAS, 112, 195

Bondi, H., & Hoyle, F. 1944, MNRAS, 104, 273

Bonoli, S., Mayer, L., Kazantzidis, S., et al. 2016, MNRAS, 459, 2603

Booth, C. M., & Schaye, J. 2011, mnras, 413, 1158

Bouché, N., Murphy, M. T., Kacprzak, G. G., et al. 2013, Science, 341, 50

Bower, R. G., Benson, A. J., & Crain, R. A. 2012, MNRAS, 422, 2816

Bradshaw, E. J., Almaini, O., Hartley, W. G., et al. 2013, MNRAS, 433, 194

Bregman, J. N., & Lloyd-Davies, E. J. 2007, ApJ, 669, 990

Bromm, V., Ferrara, A., Coppi, P., & Larson, R. B. 2001, MNRAS, 328, 958

Brook, C. B., Governato, F., Roškar, R., et al. 2011, MNRAS, 415, 1051

Brooks, A. M., Governato, F., Quinn, T., Brook, C. B., & Wadsley, J. 2009, ApJ, 694, 396

Brooks, A. M., Kuhlen, M., Zolotov, A., & Hooper, D. 2013, ApJ, 765, 22

Burkert, A., Förster Schreiber, N. M., Genzel, R., et al. 2016, ApJ, 826, 214

Capaccioli, M. 1989, in World of Galaxies (Le Monde des Galaxies), ed. H. G. Corwin, Jr. & L. Bottinelli, 208–227

Capelo, P. R., & Dotti, M. 2016, ArXiv e-prints, arXiv:1610.08507

Chabrier, G. 2003, pasp, 115, 763

Clarke, C., & Carswell, B. 2007, Principles of astrophysical fluid dynamics (Cambridge University Press)

Collaboration, P., Ade, P. A. R., Aghanim, N., et al. 2014, aap, 571, A16

Contini, T., Epinat, B., Bouché, N., et al. 2016, aap, 591, A49

Crain, R. A., McCarthy, I. G., Schaye, J., Theuns, T., & Frenk, C. S. 2013, MNRAS, 432, 3005

Crain, R. A., Schaye, J., Bower, R. G., et al. 2015, mnras, 450, 1937

Dalla Vecchia, C., & Schaye, J. 2012, mnras, 426, 140

Danforth, C. W., & Shull, J. M. 2008, ApJ, 679, 194

Danovich, M., Dekel, A., Hahn, O., Ceverino, D., & Primack, J. 2015, MNRAS, 449, 2087

Davé, R. 2009, in ASPC, Vol. 419, Galaxy Evolution: Emerging Insights and Future Challenges, ed. S. Jogee, I. Marinova, L. Hao, & G. A. Blanc, 347

Davé, R., Cen, R., Ostriker, J. P., et al. 2001, ApJ, 552, 473

Dehnen, W., & Binney, J. 1998, MNRAS, 294, 429

Dekel, A., & Birnboim, Y. 2006, MNRAS, 368, 2

Dekel, A., Birnboim, Y., Engel, G., et al. 2009, nat, 457, 451

Dolag, K., Borgani, S., Murante, G., & Springel, V. 2009, mnras, 399, 497

Draine, B. T. 2010, Physics of the interstellar and intergalactic medium (Princeton University Press)

Elgaroy, O. 2017, Perturbation theory, `http://www.uio.no/studier/emner/matnat/astro/AST4320/h12/undervisningsmateriale/perturbation.pdf`, ,

Fall, S. M. 1983, in IAU Symposium, Vol. 100, Internal Kinematics and Dynamics of Galaxies, ed. E. Athanassoula, 391–398

Fall, S. M. 2002, in Astronomical Society of the Pacific Conference Series, Vol. 275, Disks of Galaxies: Kinematics, Dynamics and Peturbations, ed. E. Athanassoula, A. Bosma, & R. Mujica, 389–396

Fall, S. M., & Efstathiou, G. 1980, MNRAS, 193, 189

Fall, S. M., & Romanowsky, A. J. 2013, ApJl, 769, L26

Fang, T., Buote, D. A., Bullock, J. S., & Ma, R. 2015, ApJs, 217, 21

Fardal, M. A., Katz, N., Gardner, J. P., et al. 2001, ApJ, 562, 605

Ferland, G. J., Korista, K., Verner, D., et al. 1998, PASP, 110, 761

Fiacconi, D., Feldmann, R., & Mayer, L. 2014, MNRAS, 446, 1957

Fiacconi, D., Mayer, L., & Madau, P. e. a. 2016, in prep.

Finlator, K., & Davé, R. 2008, MNRAS, 385, 2181

Ford, A. B., Oppenheimer, B. D., Davé, R., et al. 2013, MNRAS, 432, 89

Fraternali, F., Marasco, A., Marinacci, F., & Binney, J. 2013, apjl, 764, L21

Fukugita, M., & Peebles, P. J. E. 2004, ApJ, 616, 643

Gabor, J. M., & Bournaud, F. 2013, MNRAS, 434, 606

Gadotti, D. A. 2009, MNRAS, 393, 1531

Gadotti, D. A., & dos Anjos, S. 2001, aj, 122, 1298

Gatto, A., Fraternali, F., Read, J. I., et al. 2013, MNRAS, 433, 2749

Genel, S., Fall, S. M., Hernquist, L., et al. 2015, ApJl, 804, L40

Gingold, R. A., & Monaghan, J. J. 1977, MNRAS, 181, 375

Gnedin, N. Y., Glover, S. G. O., Klessen, R. S., & Springel, V. 2015, Star Formation in Galaxy Evolution: Connecting Numerical Models to Reality

Gott, III, J. R., & Thuan, T. X. 1976, ApJ, 204, 649

Governato, F., Willman, B., Mayer, L., et al. 2007, MNRAS, 374, 1479

Governato, F., Mayer, L., Wadsley, J., et al. 2004, ApJ, 607, 688

Governato, F., Brook, C., Mayer, L., et al. 2010, nat, 463, 203

Graham, A. W., & Worley, C. C. 2008, MNRAS, 388, 1708

Guedes, J., Callegari, S., Madau, P., & Mayer, L. 2011, ApJ, 742, 76

Guedes, J., Mayer, L., Carollo, M., & Madau, P. 2013, ApJ, 772, 36

Gupta, A., Galeazzi, M., Koutroumpa, D., Smith, R., & Lallement, R. 2009, ApJ, 707, 644

Gupta, A., Mathur, S., Krongold, Y., Nicastro, F., & Galeazzi, M. 2012, ApJ, 756, L8

Haardt, F., & Madau, P. 1996, ApJ, 461, 20

Haardt, F., & Madau, P. 2001, in Clusters of Galaxies and the High Redshift Universe Observed in X-rays, ed. D. M. Neumann & J. T. V. Tran, 64

—. 2012, ApJ, 746, 125

Hahn, O., & Abel, T. 2011, MNRAS, 415, 2101

Hastings, W. K. 1970, Biometrika, 57, 97

Henley, D. B., & Shelton, R. L. 2012, apjs, 202, 14

—. 2013, ApJ, 773, 92

Herenz, P., Richter, P., Charlton, J. C., & Masiero, J. R. 2013, aap, 550, A87

Hopkins, P. F., Kereš, D., Oñorbe, J., et al. 2014, MNRAS, 445, 581

Hopkins, P. F., Quataert, E., & Murray, N. 2012, MNRAS, 421, 3488

Hoyle, F., & Lyttleton, R. A. 1939, Mathematical Proceedings of the Cambridge Philosophical Society, 35, 592

Huang, K.-H., Fall, S. M., & Ferguson, H. C. e. a. 2016, in prep.

Hutchinson, I. H. 2015, A Student's Guide to Numerical Methods

Jesseit, R., Cappellari, M., Naab, T., Emsellem, E., & Burkert, A. 2009, MNRAS, 397, 1202

Jonsson, P. 2006, MNRAS, 372, 2

Jonsson, P., Groves, B. A., & Cox, T. J. 2010, MNRAS, 403, 17

Kaastra, J., Finoguenov, A., Nicastro, F., et al. 2013, ArXiv e-prints, arXiv:1306.2324

Kassin, S. A., Devriendt, J., Fall, S. M., et al. 2012, MNRAS, 424, 502

Katz, N., Keres, D., Dave, R., & Weinberg, D. H. 2003, in Astrophysics and Space Science Library, Vol. 281, The IGM/Galaxy Connection. The Distribution of Baryons at z=0, ed. J. L. Rosenberg & M. E. Putman, 185

Katz, N., & White, S. D. M. 1993, ApJ, 412, 455

Kaufmann, T., Mayer, L., Wadsley, J., Stadel, J., & Moore, B. 2007, MNRAS, 375, 53

Keller, B. W., Wadsley, J., Benincasa, S. M., & Couchman, H. M. P. 2014, MNRAS, 442, 3013

Kereš, D., Katz, N., Fardal, M., Davé, R., & Weinberg, D. H. 2009, MNRAS, 395, 160

Kereš, D., Katz, N., Weinberg, D. H., & Davé, R. 2005, MNRAS, 363, 2

Kimm, T., Devriendt, J., Slyz, A., et al. 2011, ArXiv e-prints, arXiv:1106.0538

Klypin, A., Zhao, H., & Somerville, R. S. 2002, ApJ, 573, 597

Kormendy, J., & Barentine, J. C. 2010, ApJl, 715, L176

Kormendy, J., & Kennicutt, Jr., R. C. 2004, araa, 42, 603

Kravtsov, A. 2014, The role of feedback in setting galaxy sizes and angular momentum, `http://online.kitp.ucsb.edu/online/stars14/kravtsov/pdf/Kravtsov_Stars14_KITP.pdf`, ,

Kravtsov, A., Vikhlinin, A., & Meshscheryakov, A. 2014, ArXiv e-prints, arXiv:1401.7329

Kravtsov, A. V. 2013, ApJl, 764, L31

Kroupa, P. 2001, MNRAS, 322, 231

Kroupa, P., Tout, C. A., & Gilmore, G. 1993, MNRAS, 262, 545

Liang, L., Durier, F., Babul, A., et al. 2016, MNRAS, 456, 4266

Lucy, L. B. 1977, AJ, 82, 1013

Marinacci, F., Pakmor, R., & Springel, V. 2014a, MNRAS, 437, 1750

Marinacci, F., Pakmor, R., Springel, V., & Simpson, C. M. 2014b, MNRAS, 442, 3745

Martin, A. M., Papastergis, E., Giovanelli, R., et al. 2010, ApJ, 723, 1359

Martin, C. L. 2005, ApJ, 621, 227

Mashchenko, S., Wadsley, J., & Couchman, H. M. P. 2007, Science, 319, 174

Mayer, L. 2012, in Advances in Computational Astrophysics: Methods, Tools, and Outcome, ed. R. Capuzzo-Dolcetta, M. Limongi, & A. Tornambè, Vol. 453 (Astronomical Society of the Pacific Conference Series), 289

Mayer, L., Governato, F., & Kaufmann, T. 2008, Advanced Science Letters, 1, 7

Mayer, L., Kazantzidis, S., Mastropietro, C., & Wadsley, J. 2007, Nature, 445, 738

Mayer, L., Tamburello, V., Lupi, A., et al. 2016, apjl, 830, L13

McCarthy, I. G., Babul, A., Bower, R. G., & Balogh, M. L. 2008, MNRAS, 386, 1309

McGaugh, S. S., Schombert, J. M., de Blok, W. J. G., & Zagursky, M. J. 2010, ApJl, 708, L14

McKee, C. F., & Ostriker, J. P. 1977, ApJ, 218, 148

Metropolis, N., Rosenbluth, A. W., Rosenbluth, M. N., Teller, A. H., & Teller, E. 1953, jcp, 21, 1087

Miller, M., & Bregman, J. 2013, ApJ, 770, 13

Miller, M. J., & Bregman, J. N. 2014, ApJ, 800, 14

Mo, H., Van den Bosch, F., & White, S. 2010, Galaxy formation and evolution (Cambridge University Press)

Mo, H. J., Mao, S., & White, S. D. M. 1998, MNRAS, 295, 319

Monaghan, J. J. 1992, araa, 30, 543

Murray, N., Quataert, E., & Thompson, T. A. 2005, ApJ, 618, 569

Navarro, J. F., Frenk, C. S., & White, S. D. M. 1995, MNRAS, 275, 56

Navarro, J. F., & Steinmetz, M. 1997, ApJ, 478, 13

Nelson, D., Genel, S., Pillepich, A., et al. 2015, ArXiv e-prints, 1503.02665

Nicastro, F., Zezas, A., Drake, J., et al. 2002, ApJ, 573, 157

Nicastro, F., Mathur, S., Elvis, M., et al. 2005, nat, 433, 495

Nichols, M., & Bland-Hawthorn, J. 2011, apj, 732, 17

Obreschkow, D., & Glazebrook, K. 2014, ApJ, 784, 26

Okamoto, T., Jenkins, A., Eke, V. R., Quilis, V., & Frenk, C. S. 2003, MNRAS, 345, 429

Oosterloo, T., Fraternali, F., & Sancisi, R. 2007, aj, 134, 1019

Oppenheimer, B. D., & Davé, R. 2008, MNRAS, 387, 577

Pallottini, A., Ferrara, A., Gallerani, S., et al. 2016, ArXiv e-prints, arXiv:1609.01719

Pedrosa, S. E., & Tissera, P. B. 2015, aap, 584, A43

Peebles, P. J. E. 1969, ApJ, 155, 393

—. 1971, aap, 11, 377

Peeples, M. S., Werk, J. K., Tumlinson, J., et al. 2014, ApJ, 786, 54

Peng, C. Y., Ho, L. C., Impey, C. D., & Rix, H.-W. 2002, aj, 124, 266

—. 2010, aj, 139, 2097

Pichon, C., Pogosyan, D., Kimm, T., et al. 2011, mnras, 418, 2493

Pillepich, A., Madau, P., & Mayer, L. 2015, ApJ, 799, 184

Planck Collaboration, Ade, P. A. R., Aghanim, N., et al. 2014, aap, 571, A16

Press, W. H., & Schechter, P. 1974, apj, 187, 425

Puchwein, E., & Springel, V. 2013, MNRAS, 428, 2966

Putman, M. E., Peek, J. E. G., & Joung, M. R. 2012, ARA&A, 50, 491

Putman, M. E., Staveley-Smith, L., Freeman, K. C., Gibson, B. K., & Barnes, D. G. 2003, ApJ, 586, 170

Quinn, T., Katz, N., Stadel, J., & Lake, G. 1997, ArXiv Astrophysics e-prints, astro-ph/9710043

Rahmati, A., Schaye, J., Crain, R. A., et al. 2016, mnras, 459, 310

Rashkov, V., Pillepich, A., Deason, A. J., et al. 2013, ApJl, 773, L32

Rasmussen, A., Kahn, S. M., & Paerels, F. 2003, in Astrophysics and Space Science Library, Vol. 281, The IGM/Galaxy Connection. The Distribution of Baryons at z=0, ed. J. L. Rosenberg & M. E. Putman, 109

Rasmussen, J., Sommer-Larsen, J., Pedersen, K., et al. 2009, ApJ, 697, 79

Rees, M. J., & Ostriker, J. P. 1977, MNRAS, 179, 541

Romanowsky, A. J., & Fall, S. M. 2012, ApJs, 203, 17

Rosas-Guevara, Y. M., Bower, R. G., Schaye, J., et al. 2015, mnras, 454, 1038

Roškar, R., Teyssier, R., Agertz, O., Wetzstein, M., & Moore, B. 2014, MNRAS, 444, 2837

Salem, M., Besla, G., Bryan, G., et al. 2015, ApJ, 815, 77

Schaller, M., Dalla Vecchia, C., Schaye, J., et al. 2015, mnras, 454, 2277

Schaye, J. 2004, apj, 609, 667

Schaye, J., & Dalla Vecchia, C. 2008, mnras, 383, 1210

Schaye, J., Crain, R. A., Bower, R. G., et al. 2015, MNRAS, 446, 521

Sedov, L. I. 1959, Similarity and Dimensional Methods in Mechanics

Sembach, K. R. 2006, in The Local Group as an Astrophysical Laboratory, ed. M. Livio & T. M. Brown, Vol. 17, 86 – 99

Sérsic, J. L. 1963, Boletin de la Asociacion Argentina de Astronomia La Plata Argentina, 6, 41

—. 1968, Atlas de galaxias australes

Shen, S., Madau, P., Aguirre, A., et al. 2012, ApJ, 760, 50

Shen, S., Madau, P., Conroy, C., Governato, F., & Mayer, L. 2014, ApJ, 792, 99

Shen, S., Madau, P., Guedes, J., et al. 2013, ApJ, 765, 89

Shen, S., Wadsley, J., & Stinson, G. 2010, MNRAS, 407, 1581

Silk, J. 2003, MNRAS, 343, 249

Smith, R. K., Brickhouse, N. S., Liedahl, D. A., & Raymond, J. C. 2001, ApJl, 556, L91

Snowden, S. L., Egger, R., Freyberg, M. J., et al. 1997, ApJ, 485, 125

Sokołowska, A., Capelo, P. R., Fall, S. M., et al. 2017, ApJ, 835, 289

Sokołowska, A., Mayer, L., Babul, A., Madau, P., & Shen, S. 2016, ApJ, 819, 21

Somerville, R. S., & Davé, R. 2015, araa, 53, 51

Sommer-Larsen, J., & Dolgov, A. 2001, ApJ, 551, 608

Spergel, D. N., Bean, R., Doré, O., et al. 2007, ApJs, 170, 377

Spinoso, D., Bonoli, S., Dotti, M., et al. 2016, ArXiv e-prints, arXiv:1607.02141

Spitzer, Jr., L. 1956, apj, 124, 20

Springel, V. 2005, mnras, 364, 1105

Stadel, J., Wadsley, J., & Richardson, D. C. 2002, High Performance Computational Astrophysics with PKDGRAV/Gasoline, ed. N. J. Dimopoulos & K. F. Li (Boston, MA: Springer US), 501–523

Stewart, K. R. 2017, in Astrophysics and Space Science Library, Vol. 430, Astrophysics and Space Science Library, ed. A. Fox & R. Davé, 249

Stewart, K. R., Brooks, A. M., Bullock, J. S., et al. 2013, apj, 769, 74

Stewart, K. R., Kaufmann, T., Bullock, J. S., et al. 2011, apj, 738, 39

Stinson, G., Seth, A., Katz, N., et al. 2006, MNRAS, 373, 1074

Stinson, G. S., Bailin, J., Couchman, H., et al. 2010, MNRAS, 408, 812

Stinson, G. S., Bovy, J., Rix, H.-W., et al. 2013, MNRAS, 436, 625

Strickland, D. K., Heckman, T. M., Colbert, E. J. M., Hoopes, C. G., & Weaver, K. A. 2004, ApJs, 151, 193

Sugerman, B., Summers, F. J., & Kamionkowski, M. 2000, mnras, 311, 762

Taylor, G. 1950, Proceedings of the Royal Society of London Series A, 201, 159

Teklu, A. F., Remus, R.-S., Dolag, K., et al. 2015, ApJ, 812, 29

Tüllmann, R., Pietsch, W., Rossa, J., Breitschwerdt, D., & Dettmar, R.-J. 2006, aap, 448, 43

Tully, R. B., & Fisher, J. R. 1977, aap, 54, 661

Tumlinson, J., Thom, C., Werk, J. K., et al. 2011, Science, 334, 948

Turner, M. L., Schaye, J., Steidel, C. C., Rudie, G. C., & Strom, A. L. 2015, MNRAS, 450, 2067

Übler, H., Naab, T., Oser, L., et al. 2014, MNRAS, 443, 2092

van de Voort, F., Quataert, E., Hopkins, P. F., et al. 2016, MNRAS, 463, 4533

van den Bosch, F. 2010, Non-linear collapse and virialization, `http://www.astro.yale.edu/vdbosch/astro610_lecture8.pdf`, ,

Ventimiglia, T., & Wayne, K. 2017, The Barnes-Hut Algorithm, `http://arborjs.org/docs/barnes-hut`, , , [Online; accessed 16-August-2017]

Vogelsberger, M., Genel, S., Sijacki, D., et al. 2013, MNRAS, 436, 3031

Voit, G. M., Kay, S. T., & Bryan, G. L. 2005, MNRAS, 364, 909

Wadsley, J., Stadel, J., & Quinn, T. 2004, New Astron., 9, 137

Wadsley, J. W., Keller, B. W., & Quinn, T. R. 2017, mnras, 471, 2357

Wang, Q. D. 1998, in Lecture Notes in Physics, Berlin Springer Verlag, Vol. 506, IAU Colloq. 166: The Local Bubble and Beyond, ed. D. Breitschwerdt, M. J. Freyberg, & J. Truemper, 503–512

Wang, Q. D., Yao, Y., Tripp, T. M., et al. 2005, ApJ, 635, 386

Weil, M. L., Eke, V. R., & Efstathiou, G. 1998, MNRAS, 300, 773

Werk, J. K., Prochaska, J. X., Tumlinson, J., et al. 2014, ApJ, 792, 8

White, S. D. M., & Frenk, C. S. 1991, ApJ, 379, 52

White, S. D. M., & Rees, M. J. 1978, MNRAS, 183, 341

Wiersma, R. P. C., Schaye, J., Theuns, T., Dalla Vecchia, C., & Tornatore, L. 2009, mnras, 399, 574

Woods, R. M., Wadsley, J., Couchman, H. M. P., Stinson, G., & Shen, S. 2014, MNRAS, 442, 732

Wu, K. K. S., Fabian, A. C., & Nulsen, P. E. J. 2001, MNRAS, 324, 95

Zavala, J., Okamoto, T., & Frenk, C. S. 2008, MNRAS, 387, 364

Zavala, J., Frenk, C. S., Bower, R., et al. 2016, MNRAS, arXiv:1512.02636

Zel'dovich, Y. B. 1970, aap, 5, 84

Zeldovich, Y. B., & Raizer, Y. P. 1966, Elements of gasdynamics and the classical theory of shock waves

Zheng, Y., Putman, M. E., Peek, J. E. G., & Joung, M. R. 2015, ApJ, 807, 103

List of Figures

Aleksandra Sokołowska

Dörrmattweg 10c, 5070, Frick AG, Switzerland
alexs@physik.uzh.ch +41 787 092 840
www.alexsokolowska.com
GitHub: alexsokolowska

Education and research experience

Sep. 2013 – Dec. 2017	Fast-Track PhD, Institute for Computational Science, University of Zurich. Research project: *Dynamics and Thermodynamics of Baryons in Galaxy-Sized Cold Dark Matter Halos* **Details:** High Performance Computing: generating large data sets with the supercomputers at CSCS and UZH Science Cloud. Big Data: visualizations and statistical analysis of smoothed particle hydrodynamics simulations (codes: Gasoline, Gadget).
Sep. 2013 – Feb. 2015	Masters of Science, Theoretical Physics, Institute for Computational Science, University of Zurich. Research project: *Gaseous Galactic Halos in the simulations of Milky Way–like galaxies*
2013 (March – July)	Internship, Institute for Theoretical Physics, University of Zurich. Research project: *Galaxy Formation*
Oct. 2010 - Jul. 2013	Bachelor of Science, Astronomy and Physics and Computer Applications, Faculty of Physics, Astronomy and Informatics, Nicolaus Copernicus University of Torun, Poland. Specialization: Radio astronomy. Research project: *The recurrent activity of the object 0932+075*

Additional experience

Sep. 2017 - now	Co-founder and Board Member of the non-profit organization *women++* aimed at increasing gender diversity in ICT. Main responsibilities: teaching programming, workshop and event organization, web development, handling marketing, strategy, and collaborations with corporate partners.
2015	Webmaster of the Institute for Computational Science.
Sep. 2013 - Dec. 2017	Teaching assistant for: Calculus I, Theoretical Astrophysics, Theoretical Astrophysics and Cosmology, Introduction to Astrobiology, Course on Milky Way for high school teachers.

Research visits

Research programs: Kavli Institute for Theoretical Physics, University of Santa Barbara, California. KITP "Cold Universe" (1 month).

Collaborations: Space Telescope Science Institute, Johns Hopkins University, Baltimore, Maryland (2 months).

Invited talks: Stanford University, CA, USA; University of British Columbia, Canada.

Workshops and conferences

Since 2013, I attended 8 conferences and 4 workshops. Most important workshops are: **2014:** Introduction course to CSCS hybrid Cray XC30, Piz Daint. **2016:** Computing the Universe: At the Intersection of Computer Science and Cosmology, CMO BIRS, Oaxaca, Mexico. **2016:** Milky Way and its environment, Paris, France. **2017:** Scientific Programming with Python, University of Zurich.

Awards

Sep.2013–Feb.2015: Fast-Track PhD (scholarship for the MSc + direct entrance to the PhD Program). **2013:** Oort and NOVA Scholarship in Astronomy for MSc Students, University of Leiden (declined). **2012–2013:** The Individual Program of Studies for the academic year 2012/2013. **2011–2012:** The Individual Program of Studies for the academic year 2011/2012; The Rector's Scholarship for the best students. **2008:** Prize in the ESO competition 'Catch a star' for the project 'The Mystery of the Orion Nebula' (CAS2008849)

Computer-related and language skills

Operating systems: Linux (Ubuntu, Scientific Linux), Mac OSX, Windows.
Programming: Python, Git; HTML, CSS, JavaScript, Twitter Bootstrap; LaTeX; C/C++, SQL, Fortran (basic);
Languages: Polish (native), English (proficient), German (upper intermediate).
Future courses: EPFL Extension School on machine learning (start: December 2017).

Publications

1. "Multi-epoch VLBA observations of radio galaxy 0932+075: is this a compact symmetric object?", Marecki & Sokolowska (2014), A&A, 569, A22
2. "The baryonic and stellar content of galaxies from dwarf scales to the scale of X-ray bright galaxy groups: do hydro simulations match the observed Universe?", Mayer, Sokolowska et al. (2015), proceedings of *Cosmological simulations: from galaxies to large scales.*
3. "Diffuse Coronae in Cosmological Simulations of Milky Way-sized Galaxies", Sokołowska et al. (2016), ApJ, 819, 21
4. "Galactic angular momentum in cosmological zoom-in simulations. I. Disk and bulge components and the galaxy–halo connection", Sokolowska et al. (2017), ApJ, 835, 289
5. "The complementary roles of feedback and mergers in building the X-ray coronae of Milky Way-sized halos", Sokolowska et.al (2017), arXiv:1708.07820

Hobbies

Outdoors: hiking, windsurfing, skiing, kung-fu, gardening. Event organization and attendance in the tech space: data science meetups, hackathons (joined HackZurich 2017). Other: living sustainably.

Volunteering

Commited to diversifying STEM fields and tech industry. Organizer/speaker/tutor at events and coding workshops in Switzerland (meetup groups: Geek Girls Carrots Switzerland, Zurich Women in Tech Industry and Academia, Women in STEM).

References

Prof. Lucio Mayer, Institute for Computational Science, University of Zurich. Email: lmayer@physik.uzh.ch

Prof. Arif Babul, Department of Physics and Astronomy, University of Victoria. Email: babul@uvic.ca

Acknowledgements

Years that I spent at the University of Zürich, starting with my research project at the Institute for Theoretical Physics back in 2013, through the challenges posed by Fast Track PhD until 2017, were a wonderful experience. Owing to the collaborative spirit of ICS, the support of my PhD advisor, and a good will of my colleagues-experts, I gained deeper insights into the intersection of numerical models, computer science and theoretical physics, and flourished as a person. The latter is what I am most grateful for.

I would like to thank prof. Lucio Mayer for opening many doors in front of me, and actively encouraging me to be a part of a wider scientific community. Already from the start of my PhD, Lucio gave me the freedom to research and learn in parallel. The education I received went way beyond science and computing – for example, Lucio supported my participation in the career building program for women in science at ETH Zürich. I want to thank him for establishing a work style, which easied the process of me becoming an independent researcher, and for always giving me the feeling that my contribution to scientific discussions was valued. With Lucio as a mentor, I grew to appreciate the importance of both effectiveness and empathy as leadership traits.

My scientific training was also largely influenced by two important figures: prof. Arif Babul and prof. Mike Fall. I would like to thank them for taking me under their wings, providing with both career and technical guidance, and hosting me during my research stays in North America. I would also like to thank Piero Madau, Sijing Shen, Pedro Capelo, Ali Rahmati, Stelios Kazantzidis, Victor Debattista, Sebastian Trujillo-Gomez, and Silvia Bonoli for the fruitful collaboration on multiple scientific projects, some of which have yet to see the daylight. I would also like to acknowledge the kindness and the administrative support from Suzanne Wilde and Regina Schmid, from the very beginning of my time at Uni Zurich till the very end.

Over the course of past years, I could always rely on my colleagues Valentina Tamburello, Pedro Capelo, Irshad Mohammed, Davide Fiacconi, Christian Rheinhardt, and Maria Han Veiga as a source of comfort. Remaining sane, especially in those dead-end moments of my PhD, was possible only thanks to my partner and greatest support Sebastian Bürgel.

Last but not least, I would like to thank Valentina Tamburello and Joanna Drazkowska who fortified my aspirations of driving more women to STEM, and the institute director, prof. George Lake, for supporting the cause by hosting one of the tech talks at ICS back in 2016. One step at a time, this initiative turned into a non-profit organization *women++*, whose team and community became a vital ingredient of my after-work life, and gave me motivation to keep growing.

Merci viel mal!